Dynamic Subgrid Scale Combustion Modeling for Large Eddy Simulation of Premixed Flames

Vom Fachbereich Maschinenbau
an der Technischen Universität Darmstadt
zur
Erlangung des Grades eines Doktor-Ingenieurs (Dr.-Ing.)
genehmigte

Dissertation

vorgelegt von

Arash Hossein Zadeh, M.Sc.

aus Teheran, Iran

Berichterstatter:	Prof. Dr.-Ing. J. Janicka
Mitberichterstatter:	Prof. Dr.-Ing. W. Schröder
Tag der Einreichung:	21.10.2014
Tag der mündlichen Prüfung:	17.02.2015

Darmstadt 2015
D17

ACKNOWLEDGEMENTS

First and for most I would like to thank my advisor Prof. J. Janicka for his support, patience and help. I have always enjoyed his wide vision and deep knowledge of science and technology. Beside these, I have learned a lot from his practical attitude and always admired his keen wit in using magical words who alive the equations and aspire the audience, being a great speaker.

I would like also to thank Prof. W. Schröder from RWTH, who kindly accepted to be my second advisor. During numerous meetings in the “combustion noise” project, I enjoyed his support and problem solving attitude.

I would like also to thank Prof. A. Sadiki for introducing me to the EKT and his continuous support and encourage. I appreciate his patience and have a deep respect for his kind manner.

I would like to thank my M.Sc thesis supervisor and former colleague P. Pantangi for his enormous help and patience. I learned a lot from him and always admire his intellectual power beside his everlasting kindness and smile.

I would like also to thank other colleagues and roommates for our great time in EKT as R. Haghighi, A. Avdic, D. Jesch, F. Oezdogan, S. Doost and F. Sacomano and others. I owe a special thank to dear system administration team M. Schmitt and T. Klenke for their help and support, during many hardware failures.

I am very grateful and would like to show my deep respect to all my professors during my time in the TUD. Specially Prof. M. Oberlack, Prof. K. Hanjalic, Prof. S. Jakirlich, aspiring me in the CFD world.

At last but not least I would like to thank my parents for their non-remunerated support, my mother for her tender, care and friendship and my father who always inspires me in the scientific and technical world and being a fair individual. I would like to thank my compassionate and smart wife “Parvaneh” for her enormous support and encourage over all these years. At the end as it is said “life is what happens” I want to show my love to our newly born baby son “Atbin” who gives me the glimmers of hope.

Arash Hossein Zadeh Darmstadt, 20.10.2014

Contents

Greek Letters

β	Power-law
χ	Scalar dissipation rate
Δ	Filter width
ε	Turbulent kinetic energy dissipation
ϕ	Arbitrary quantity /equivalence ratio
Φ_{ij}	Spectral density
θ	Thermo-chemical quantity
η	Kolmogorov length scale
κ	Wave number
ν	Kinematic viscosity
ν_t	Turbulent viscosity
ν_{sgs}	SGS turbulent viscosity
μ	Dynamic viscosity
ω	Char. turbulent frequency
$\dot{\omega}$	Chemical source term
ρ	Density
ψ	Test function
τ	Reynolds stresses /SGS stress tensor /Kolmogorov time scale

Latin symbols

C	Model coefficient
C_{ij}^0	Cross stresses
D	Molecular diffusion coefficient
D_t	Turbulent diffusion
J_k^{sgs}	sgs flux vector
Le	Lewis number
L_{ij}^0	Leonard stresses
$L_{ij,k}$	Integral length scale
N_g	Number of grid points
N_{nu}	Number of operation
P_k	Turbulent production
Re	Reynolds number
R_{ij}	Two point correlation
R_{ij}^0	SGS Reynolds stresses
S_{ij}	Strain rate
Sc_t	Turbulent Schmidt number

Operators

$\bar{\cdot}$	Filter
$\tilde{\cdot}$	Favre filter
$\hat{\cdot}$	Test filter
$\langle\cdot\rangle$	Reynolds average

Abbreviations

ATF	Artificially Thickened Flame
CDS	Central Differencing Scheme
CFD	Computational Fluid Dynamics
CV	Control Volume
DNS	Direct Numerical Simulation
EDM	Eddy Diffusivity Model
EVM	Eddy Viscosity Model
FDM	Finite Difference Method
FEM	Finite Element Method
FGM	Flamelet Generated Manifolds
FPI	Flame Prolongation of ILDM
FVM	Finite Volume Method
FSD	Flame Surface Density
F-TACLES	Filtered TAbulated Chemistry for LES
FSD	Flame Surface Density
ILDM	Intrinsic Low Dimensional Manifolds
ISAT	In Situ Adaptive Tabulation
LDV	Laser Doppler Velocimetry
LES	Large Eddy Simulation
PDF	Probability Density Function
RANS	Reynolds Averaged Navier-Stokes
RSM	Reynolds Stress Model
TVD	Total Variation Diminishing

Chapter 1

Introduction

1.1 Motivation

Lean premixed combustion is recently a theme of interest in gas turbines in an effort to reduce nitrogen oxides (NOx) emission. This is a result of lower burning temperature in comparison to non-premixed combustion regimes. However, the occurring combustion driven induced oscillation, vibration, flashback and flame blow off belong to undesired side effects and are harmful for the system and consequently lead to the operation deficiency and ultimately degrade the system life cycle.

The combustion chamber should be ideally compact in dimension, ignitable and stable in combustion. The pressure loss, the emission of CO and unburnt fuel, (NOx) and soot should be also small. The flow in a combustion chamber is characterized by various interacting phenomena like mixing, turbulence, chemical processes, heat and mass transfer, radiation and multiphase flow. The other very important characteristic of flow in combustion chamber is that it is unsteady, which causes some events like blow off, quenching and auto ignition. The prediction of such a system with these complex interacting processes like swirling flow, recirculation and break down of large scales are very complicated and widely beyond the scope of available CFD tools used in industrial simulation like RANS models. On the other hand the demand of a reliable tool which can predict all these effects is very high, as the optimization by means of considering a steady state flow in most of time is ineffective.

In this manner Large Eddy Simulation (LES) has demonstrated abilities which can be used to predict such a complex system. The developments in computer world and enhanced computing power beside new numerical techniques make it possible to use the LES as a compromise between DNS and RANS. To reach the aim of having a reliable and overall model, the LES based model should be also continually improved. This overall model ultimately should have the ability of predicting all phenomena interacting in combustion chamber as mixing, turbulence chemistry interaction and multiphase flow. One important issue in this procedure is to have a model with physic preserving turbulence models. As in LES the large scale eddies are simulated and small scales are modeled, the model we use for this subgrid scale eddies should also have a reliable physics.

The aim of this work is the evaluation of the effect of subgrid scale modeling, validation and comparison of different combustion models in context of Large Eddy Simulation (LES) for premixed flames. The in-house code FASTEST is used for the numerical investigation of the premixed combustion in the turbulent flames with gas turbines characteristics, i.e., high turbulence intensity and high energy density.

1.2 State of the art

The development of numerical models for reacting flows has seen significant progress in recent years. However, due to the high complexity of the interaction between turbulence and chemistry in different combustion regimes (premixed, partially premixed and diffusion controlled), many scientific questions are still open [1]. Even within a single regime, various turbulence-chemistry interaction mechanisms lead to different flame behavior.

For this reason, lately combustion models are in the development, who aspire to reduce this limitation. The multi-regime flamelet combustion models (MFM) can predict the different types of interactions in combustion systems. These models are currently still at a low level of development and have difficulty with the correct modeling of the parameters such as the mixture fraction and the progress variable [2].

As another example, for a universal combustion model, the PDF model transport equation can be mentioned. In this model, the average chemical source term is exact and therefore can be used for each combustion regime, but the interaction between the turbulence and chemistry should be modeled. However, this model have conceptual difficulties with the premixed combustion and is always associated with high computational effort [3]. Therefore, it still make more sense to describe each particular regime by its own specific combustion model.

The combustion system involves highly unsteady interacting physical mechanisms such as flame, vorticity and acoustic fluctuations [4]. Thus, Large Eddy Simulation (LES) as an adequate tool is an appropriate candidate to give better insight into these unsteady phenomena. Although LES has shown its strength in predicting unsteady phenomena in non-reacting flows, it is still in the early stages of use for combustion [5, 6].

In LES the large turbulent scales of the flow are computed explicitly and the small scales or modeled. The combustion is basically a small scale and consequently a subgrid scale phenomena and hence modeling is necessary. For instance, in the case of premixed combustion, the flame thickness is much smaller than typical LES mesh size. As the progress variable is a stiff variable of space, the flame front can not be resolved directly and LES seems to be unsuitable for this type of reacting flow.
To overcome this, diverse approaches have been proposed. In level set approach the flame front is viewed as infinitely thin and solving a propagating kinematic equation leads to tracking the flame front position [7, 8, 9]. Another concept is the physical filtering of the reaction rate or the reaction progress variable (FSD, Flame Surface Density) [10]. An alternative is to artificially thicken the flame front and make it resolvable on LES grid (TFLES, Thickened Flame model of LES) [11, 12] or to introduce an a priori filtering of flamelets using a Gaussian filter (F-TACLES, Filtered TAbulated Chemistry for LES) [13, 14].

As noted before, the premixed combustion is basically a subfilter problem. Making the flame front resolvable on LES mesh is just one side of this challenge. The other remaining problem is to rebuild the unresolved flame/turbulence interaction, mostly lost during artificially thickening or filtering the flame front. To tackle this problem, different models have been proposed mainly depending on the stated combustion concept, the subfilter turbulent speed for level set method [7, 8], the flame surface density [10] and the flame surface wrinkling factor for artificially thickening of the flame front [11, 12, 15].

The proposed models are mostly not adapted to the transient flows and rely only on the flame/turbulence equilibrium assumption. For the consideration of flame surface and turbulence interaction in transient flows, different approaches are proposed and investigated. One concept is based on the solution of a balance equation for flame surface density [16] or flame wrinkling factor [17]. The alternative is using algebraic models and application of a "Germano-like" identity [18] to calculate dynamically the model parameters from the known resolved field [19, 20, 8, 21, 22, 23, 24, 25].

The current work introduces an extension of an artificially thickened flame approach coupled with tabulated chemistry (FGM, Flamelet Generated Manifolds) [15] with a dynamic wrinkling model [19]. The dynamic model is implemented in the block structured low-Mach code based on the procedure proposed by [21]. To analyze this model improvement, simulations are conducted for a lean premixed Bunsen type flame (Matrix Burner) with high Reynolds number, using two different combustion models, the ATF (Artificially Thickened Flame) and F-TACLES (Filtered TAbulated Chemistry for LES), both with dynamic and non-dynamic formulation of power-law wrinkling model. The dynamic formulation of the F-TACLES approach has been implemented in the same code and evaluated for different configurations [23, 24, 25].

1.3 Structure of the work

This work consists of seven chapters. The Chap.1 includes motivation of the the current work, state of the art of the numerical simulation of the reacting flows and structure of the work. In Chap.2 we will have a review on the turbulence phenomena and the simulation and modeling of the turbulent flow. The Chap.3 will briefly describe the numerical methods used in this work and the FASTEST code.

The combustion models and particularly the combustion modeling of the premixed combustion in the context of Large Eddy Simulation (LES) will be reviewed in the Chap.4. The developed approach and the derivation of the proposed model in the framework of this work is explained in the Chap.4. The numerical methods invoked in the model development are explained also in the same chapter.

At Chap.5 we will review the validation cases and comparison between various implemented models and ultimately the results of Large Eddy Simulation (LES) of a turbulent premixed flame with high turbulence intensity (Matrix burner) using dynamic combustion models.

At Chap.6 the application of the new developed model on series of premixed flames with low turbulence intensity (Berlin burner) will be reviewed.

At last the work is summarized and the outlook of the work is proposed at Chap.7.

Chapter 2

Numerical simulation and modeling of turbulent flows

2.1 Introduction

Fluids are substances which do not show any resistance to the shear forces, the smallest force can also cause deformation. For the most practical applications, fluids could be treated as continuum because the length and time scales are dominantly larger than molecular scales. The Knudsen number quantifies the separation of length scales and is defined as ratio of molecular free length pass to physical length scale :

$$Kn = \frac{\lambda}{l}, \tag{2.1}$$

and is always $Kn << 1$ which is appropriate for continuum hypothesis.

The flow of fluid is caused by external forces; these forces can be divided to body forces like gravity and surface forces as pressure gradient. To model a physical problem mathematically, one should decide which conservation equations are needed and which simplification should be implemented. Following the conservation equations should be derived either in differential or integral form depending on the demanding variable and regarding area.

- **Integral** form of the conservation equation: describes the temporal variation of an extensive variable. The time dependent ordinary differential equations could be derived from this equation type. Some famous conservation equations in integral form are continuity Eq.2.2 and momentum Eq.2.4, which will be discussed explicitly in coming section 2.2.

- **Differential** form of the conservation equation:

  describes the temporal and spatial variation of an intensive variable. For solution of partial differential equation, boundary condition is needed. In computational fluid dynamics, conservation equations are used in differential form. These equations should be discretized and ultimately numerically integrated.

2.2 Governing equations of fluid motion

2.2.1 The continuity equation

The continuity or mass-conservation equation in integral form is:

$$\frac{\partial}{\partial t}\int_V \rho dV + \int_S \rho.\mathbf{n}dS = 0 \tag{2.2}$$

The mass change rate in the material control volume is zero, that means within control volume will be temporally constant. With implementation of Stokes theorem to convection term and for an infinitesimal control volume, continuity equation can be written in differential form:

$$\underbrace{\frac{\partial \rho}{\partial t}}_{Temporal\ change} + \underbrace{\nabla.(\rho\mathbf{U})}_{Advection\ term} = 0, \tag{2.3}$$

which is written for a discrete and coordinate independent system. Therefore, for different divergence operator, different coordinate system can be used.

2.2.2 The momentum equation

The momentum equation is based on Newton's second law. The momentum equation for incompressible flow and a fixed control volume in integral form is:

$$\frac{\partial}{\partial t}\int_V \rho\mathbf{U}dV + \int_S \rho\mathbf{U}\mathbf{U}.\mathbf{n}dS = \sum \mathbf{f}, \tag{2.4}$$

in which the forces on RHS are body and surface forces.

- **Body forces**:

  for example centrifugal, Coriolis and gravitation forces;

- **Surface forces**:

  for example normal and shear stresses or surface tensions.

From the molecular view, the surface forces from pressure and viscose stresses are momentum fluxes into the control volume surface, they can be described by the stress tensor $\tau_{ij}(x,t)$, which for a constant property Newtonian fluids is:

$$\tau_{ij} = -\mathbf{P}\delta_{ij} + \mu(\frac{\partial \mathbf{U}_i}{\partial x_j} + \frac{\partial \mathbf{U}_j}{\partial x_i}) \tag{2.5}$$

The integral form of the momentum equation can be written as:

$$\frac{\partial}{\partial t}\int_V \rho\mathbf{U}dV + \int_S \rho\mathbf{U}\mathbf{U}.\mathbf{n}dS = \int_S \mathbf{T}.\mathbf{n}dS + \int_V \rho\mathbf{b}dV, \tag{2.6}$$

with implementation of Stokes theorem on the convective and diffuse term of the momentum equation, the differential form of the momentum equation can be written as:

$$\rho\frac{\mathbf{DU}_j}{\mathbf{D}t} = \nabla.\mathbf{T} + \rho\mathbf{b} \tag{2.7}$$

Considering the gravity as interested body force $g = -\nabla\Psi$, in which Ψ is the gravitational potential and substituting in above equation the **Navier-Stokes** equation can be obtained:

$$\frac{\mathbf{DU}}{\mathbf{D}t} = \frac{-1}{\rho}\nabla p + \nu\nabla^2\mathbf{U}, \tag{2.8}$$

where $p = \mathbf{P} + \rho\Psi$ is the modified pressure and $\nu = \mu/\rho$ is the kinematic viscosity. Assuming a constant density flow, the Navier-Stokes equation can also be derived in dimensionless form if one writes the all variables in non-dimensional form:

$$\frac{\partial U_j^*}{\partial t^*} + U_i^*\frac{\partial U_j^*}{\partial x_i^*} = \frac{1}{Re}\frac{\partial^2}{\partial x_i^*}\frac{\partial U_j^*}{\partial x_i^*} - \frac{\partial p^*}{\partial x_i^*}, \tag{2.9}$$

where the Reynolds number is:

$$Re = \frac{\rho\mathbf{U}L}{\mu}, \tag{2.10}$$

in which $\mathbf{U}$ and L are characteristic velocity and length scales of mean flow, ρ is fluid density and μ is the dynamic fluid viscosity.

2.2.3 The conserved passive scalar transport equation

The conservation equation for a conserved passive scalar $\theta(x, t)$ is:

$$\frac{\mathbf{D}\theta}{\mathbf{D}t} = D\nabla^2\theta, \tag{2.11}$$

in which D is diffusion coefficient, for example for θ as species concentration D would be the molecular diffusivity and ν/D is Schmidt number. The conserved scalar means that there is no source term in equation and passive stands for having no effect on material properties as density or diffusivity. This equation can be generalized for any scalar transport by adding the source term and dependency to material properties to be used for example for predicting chemistry or energy scalars [26], [27].

The complete transport equation for species mass concentration or a reaction progress variable will be discussed in Chap.4. The closure problem for the turbulent reacting flow will be reviewed and typical closure concepts will be presented.

2.3 Turbulent flow

2.3.1 Introduction to turbulent flow physics

Dimension analysis in fluids mechanics has proved that in incompressible, frictional flows within the geometrical similar systems the Reynolds-number Eq.2.10, determines the flow characteristics. In technical devices we are often faced with flows with high Reynolds-number , and it is also known that flow regime and characteristics will change very rapidly when they excess the critical Reynolds-number which is also problem dependent. The steady regime will change to unsteady although the boundary condition remain the same as before. The flow is three dimensional, unsteady and shows a stochastic character which means that flow variables have random characteristic in both time and space. This kind of regime is known as turbulent flow. Such a regime shows also some other significant characteristics:

- **High diffusivity** which means that in a turbulent flow mixing is more rapidly than a laminar flow and transport of scalars are also increased
- **Dissipative** means there is a need for more energy supply as kinetic energy will be vanished due to transform to heat
- **Diverse length scales** in a turbulent flow exist many length scales from large energy containing eddies to small dissipative structures

2.3.2 Turbulence scales and mechanism

One of the most important definitions in turbulence is "**eddy**" which can be explained as disturbances and inhomogeneities with various time and length scales. The main mechanism in turbulence is the stretching of these eddies due to internal and external forces. Eddies with different order and size are always available in the turbulent flow, the largest length scale are always in order of flow geometry and often called as flow length scale, the region of a large eddy can also simultaneously include smaller eddies. The end of energy spectrum enclose the smallest eddies which are to be dissipated by viscous stresses into thermal energy. This dissipative small eddies gain their energy from slightly larger ones (intermediate scales) and the larger ones receive from even lagers till the largest eddies which gain the energy from the mean flow; this is the so called cascade process (See Fig.2.1), transferring the energy from mean flow to energy containing eddies up to dissipation into thermal energy.

The turbulence mechanism can be divided into the following steps:

- Production and Transport in physical space by convection and diffusion of mean and respectively fluctuating momentum
- Redistribution
- Transport in spectral space, means energy cascading due to vortex stretching
- dissipation to the thermal energy by viscous effects

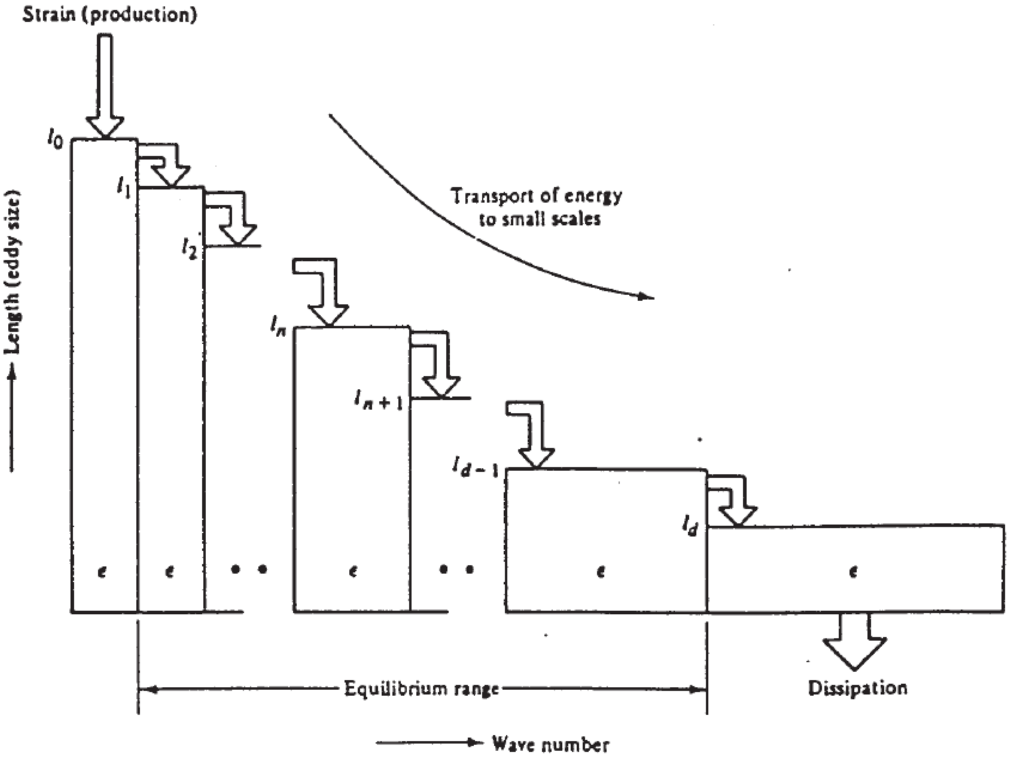

Figure 2.1: Energy cascade process and the spectrum of eddies [28].

2.3.2.1 Turbulence scales

In turbulence we are faced to different length and time scales, each length and time scale is corresponding to a particular effect, large eddies are responsible for transport of momentum, heat and species; they are limited to characteristic flow dimension, intermediate scales are associated to the cascade effect and viscous dissipation happening in small eddies. Energy containing eddies is also associated to the scales which are responsible for extracting the energy from mean flow. The scales of energy containing eddies, (nearly largest eddies) can be defined in dependency of the turbulent kinetic energy and the its dissipation rate

$$l_0 = \frac{k^{3/2}}{\varepsilon} \tag{2.12}$$

$$\tau_0 = \frac{k}{\varepsilon} \tag{2.13}$$

As kolmogorov's first similarity hypothesis, in high Reynolds number turbulent flows, the statistics of the small scale eddies uniquely determined by kinematic viscosity ν and turbulent kinetic energy dissipation rate ε.

$$\eta = (\frac{\nu^3}{\varepsilon})^{1/4} \tag{2.14}$$

$$\tau_\eta = (\frac{\nu}{\varepsilon})^{1/2} \tag{2.15}$$

$$u_\eta = (\varepsilon\nu)^{1/4}, \tag{2.16}$$

in which the u_η is the Kolmogorov's velocity scale. The Kolmogorov's Reynolds number is unity $Re_\eta = \eta u_\eta/\nu = 1$, showing the consistency with the cascade procedure to dissipate energy at the small scales by very small Reynolds number.
Now the ratio between large and small scales can be estimated with assumption $\varepsilon \approx {u_0}^3/l_0$

$$\frac{\eta}{l_0} = (\frac{\nu^3}{\varepsilon})^{1/4} {l_0}^{-1} = (\frac{u_0^3 l_0^3}{\nu^3})^{-1/4} = Re^{-3/4} \tag{2.17}$$

$$\frac{u_\eta}{u_0} = (\varepsilon\nu)^{1/4} {u_0}^{-1} = (\frac{u_0 l_0}{\nu})^{-1/4} = Re^{-1/4} \tag{2.18}$$

$$\frac{\tau_\eta}{\tau_0} = (\frac{\nu}{\varepsilon})^{1/2} \frac{u_0}{l_0} = (\frac{u_0 l_0}{\nu})^{-1/2} = Re^{-1/2}. \tag{2.19}$$

It is clear that the ratio of the very small dissipative eddies to the energy containing eddies decreases as the Reynolds number increases; this means also that there exist an intermediate range of scales which also increase as Reynolds number increases. Since eddies in this intermediate scale are very larger than the dissipative range, it can be assumed that their Reynolds number is also large and little affected by the viscosity and scales can be determined by dissipation ε independent of kinematic viscosity ν. This intermediate scales are in the so called inertial sub-range .

2.3.2.2 The energy spectrum

Distribution of turbulent kinetic energy between the eddies of different scale is theme of interest. A product of two fluctuating quantity at two spatial or temporal point, like two point correlation can help to gather some insight about turbulence structure of different eddy scales.

$$R_{ij}(x,t,r,\tau) = \overline{u'_i(x,t)u'_j(x',t')}, \tag{2.20}$$

in which $x = x' + r$, r denoting the distance between two points and $t' = t + \tau$.
The integral length scale, which correspond to largest eddies can also be achieved from the two point correlation function

$$L_{ij,k} = \frac{1}{2R_{ij}(x,t,0,0)} \int_{-\infty}^{\infty} R_{ij}(x,t,r_k,0)dr_k. \tag{2.21}$$

As discussed, the integral length scale is just representing the largest scale in turbulent spectrum and does not give more information on other scales; hence it is more useful to transform it via Fourier transform to achieve the spectral density

$$\Phi_{ij}(K) = (\frac{1}{2\pi})^3 R_{ij}(x,r)e^{(-iKr)}dr, \tag{2.22}$$

in which $K(\kappa_1,\kappa_2,\kappa_3)$ is the wave number vector and $\kappa = 2\pi/L$. Sum of diagonal components of Φ at $r = 0$ is the kinetic energy at a given wave number. Introducing $R_{ij}(x,r)$

as inverse Fourier transform of $\Phi_{ij}(K,r)$

$$R_{ij} = \int_{-\infty}^{\infty} \Phi_{ij}(K,r)e^{(iKr)}dK, \tag{2.23}$$

and for $r = 0$

$$R_{ij} = \overline{u_i'u_j'} = \int_{-\infty}^{\infty} \Phi_{ij}(K)dK, \tag{2.24}$$

by integration the energy spectrum over a spherical shell σ of radius $\kappa = |K|$ and for $i = j$, turbulent kinetic energy spectrum is

$$\begin{aligned} E(\kappa) &= \frac{1}{2}\int_{\sigma} \Phi_{ii}(\kappa)d\sigma \qquad (2.25)\\ \int_0^{\infty} E(\kappa)d\kappa &= \frac{1}{2}\overline{u_i'u_i'} = k. \qquad (2.26)\end{aligned}$$

The turbulent kinetic energy spectrum can be divided into three regions:

- I. Generation of large eddies
- II. Inertial sub-range
- III. Dissipation range

We have discussed before about the region I and III, let have some deeper insight in region II.
In sufficiently high Reynolds number as the Kolmogorov's dissipative scales become very small, compared to large eddies in energy containing region, there should exist a region with intermediate scales. This region represents the transport region which is called spectral transfer in wave number space. In the concept of energy cascade we assume that the energy is transferring from large scale energy containing eddies to the small scale dissipative eddies, this happens in spectral transfer region in which energy transfer rate gained from the large eddies is proportional to dissipation, $P_k = \varepsilon$. As Kolmogorov's second similarity hypothesis; in this transfer region, the statistics of flow motion have a universal form which can be determined only by ε. Dimensional analysis gives:

$$\begin{aligned} E[L^3/T^2] &= \kappa^a[1/L]\,\varepsilon^b[L^2/T^3] \qquad (2.27)\\ 3 &= -a + 2b \quad for\ [L]\\ -2 &= -3b \quad for\ [T], \qquad (2.28)\end{aligned}$$

so we came to $a = -5/3, b = 2/3$ and we get finally the Kolmogorov's spectrum -5/3 law

$$E(\kappa) = C\varepsilon^{2/3}\kappa^{-5/3}, \tag{2.29}$$

where C is a universal constant. This law states that in a turbulent flow with high Reynolds number the energy has $-5/3$ decay in the inertial region [28], [26].

2.4 Introduction to turbulence modeling

Turbulent flow shows in compare to laminar flow an increase in flow resistance, which is related to averaged fluctuations flux momentum or so called Reynolds stresses $-\rho\overline{u'_i u'_j}$. In turbulent flows, these Reynolds stresses are generally very larger than viscose friction stresses. To have a solution for Navier-Stokes equations the Reynolds stresses should also be known and cannot be neglected, but there is no analytical solution for this variable which lets us to solve the Navier-Stokes equation for fully developed turbulent flow without need to have supplemental theories. In next sections we will see how we can solve this problem.

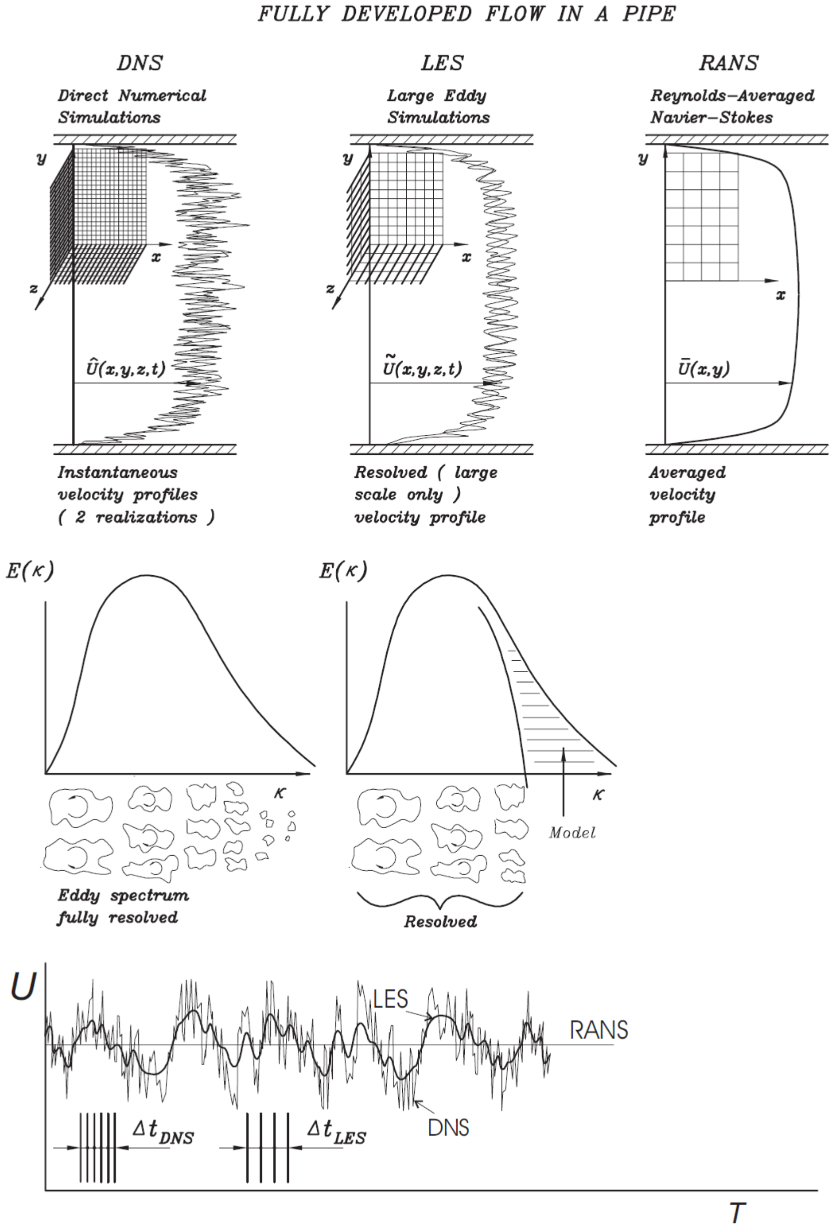

Figure 2.2: Different approaches to solve turbulent flow in a fully developed flow in a pipe. Comparison of predicted velocity profile by DNS, LES and RANS [28].

2.5 Direct numerical simulation

Direct numerical simulation (DNS) is associated to resolve all scales of motion in Navier-Stokes equations; from the large energy containing eddies to the Kolmogorov's dissipative ones (See Fig.2.2). Basically the DNS is the easiest and most accurate approach, if it can be applied. However because of very high computational cost, it is infeasible in high Reynolds or complex geometries.

As discussed in the section (2.3.2.1), in turbulent flows by increasing the Reynolds number, the range of scales also increases and the dissipative scales became very small. AS DNS is expected to resolve all range of eddies, the average size of grid cell Δ should be smaller than the smallest eddies which here are corresponding to kolmogorov's dissipative scales. In a 3-D turbulent flow, the minimum required grid points can be estimated as

$$N_g \approx (\frac{L}{\eta})^3 \approx Re^{9/4}, \tag{2.30}$$

assuming that number of numerical operations required for each grid cell is $Re^{1/2}$, then the total operation number in a 3-D turbulent flow correspond to

$$N_{nu} \approx Re^{11/4}, \tag{2.31}$$

shows that DNS is just rational up to moderate Reynolds numbers roughly up to 10^4 and not complex geometries which is normally being used in technical world.

The spatial resolution criteria discussed above is commonly used. However, there exist other researches [29] which states that smallest resolved length scale is just required to be $O(\eta)$, which means that if the resolution be fine enough to catch the most of dissipation, then the first and second statistics are also obtainable.

Another important influencing factor on the resolution is the numerical method used in DNS, which can be divided into two most used methods, spectral or differencing schemes. The coupled primary errors associated to spatial discretization are the differentiation error and the error coming from the transport equations non-linearity.

2.5.0.3 Different discretization methods

The spectral methods are using global ansatz rather than local ansatz in differentiating schemes like FEM (Finite Elements Method) and FVM (Finite Volume Method) approaches. By discretization a problem we have

$$\begin{aligned} Probelm: L\phi &= f\ in\ \Omega,\ B\phi = g\ at\,\partial\Omega \\ Ansatz: \phi \approx \phi_N &= \sum_{k=1}^{N} a_k \psi_u \qquad (2.32) \\ Residual: R &= L\Phi_N - f \qquad (2.33) \\ with\ a\ test\ function\,\psi_j: \int_\Omega R\psi_j &= 0 \quad \forall j = 1, ..., N, \qquad (2.34) \end{aligned}$$

the solution is

$$\underbrace{\sum_{k=1}^{N} a_k \int_\Omega L\phi_k \psi_j dx}_{S_{kj}} = \underbrace{\int_\Omega \psi_j dx}_{b_j}, \tag{2.35}$$

in which the ψ_j can be achieved in different methods. For example:

$$Galerkin\ method : \psi_j = \phi_j, B\phi = g\ \forall j, \tag{2.36}$$

which is used in FEM or FVM methods with local approach. The collocation method for spectral method with global approach

$$Collocation\ method : \psi_j = \delta(x_j - x), \tag{2.37}$$

and an extra equation for Boundary condition which will be used in spectral methods. The ansatz for ψ_j can be chosen :

- Fourier for periodic problems, as a finite Fourier series:

  $$\phi(x,t) = \sum_{\kappa} e^{i\kappa x}\widehat{\phi}(\kappa, t), \tag{2.38}$$

  in which the solution is transferring from physical space to spectral space.
- Orthogonal polynomials (like Chebyshev) for other problems

The most interesting advantage of collocation methods is the exponential convergence of the solution in which the error degree is under 1 percent. However, there is also some disadvantage like that there is no flat solution for complex configurations.

2.6 Reynolds averaged Navier-Stokes simulation

2.6.1 Reynolds decomposition

The Navier-Stokes equations (Eq.2.8) are derived without consideration of whether the flow is laminar or turbulent. As the Navier-Stokes equations are second order non-linear partial differential, except some simplified cases, there is no exact solution. In case of laminar flow the problem can be often explained as steady and the problem can also be reduced to two dimensional if in third direction the flow is homogeneous or there exist some symmetric axis. In this case the flow can be solved numerically.

The turbulent flow by its nature is unsteady and three dimensional and hence the above explained simplification is not applicable, although the averaged flow is constant and steady and the interest of most studies are also in the mean field of the flow.

Osborne Reynolds [30] used this reality and proposed the decomposition of the instantaneous property ϕ to a mean value $\langle\phi\rangle\,(u, p, T, \rho, ...)$ and the accomplishing fluctuations ϕ'. If the flow is changing slowly with time, the time mean can be

$$\begin{aligned} \phi(x_i, t) &= \langle\phi\rangle\,(x_i) + \phi'(x_i, t) && (2.39)\\ \langle\phi\rangle\,(x_i) &= \lim_{t\to\infty}\int_0^t \phi(x_i, t)dt && (2.40) \end{aligned}$$

If it is not the case, the averaging method is ensemble mean with N samples

$$\langle\phi\rangle\,(x_i, t) = \lim_{N\to\infty}\frac{1}{N}\sum_{i=1}^{N}\phi(x_i, t). \tag{2.41}$$

Applying the Reynolds averaging to the conservation equations delivers:

- Reynolds averaged Navier-Stokes equation

$$\rho\frac{\partial \langle U_i\rangle}{\partial t}+\rho\langle U_j\rangle\frac{\partial \langle U_i\rangle}{\partial x_J}=-\frac{\partial \langle P\rangle}{\partial x_i}+\frac{\partial}{\partial x_j}\left[\mu\left(\frac{\partial \langle U_i\rangle}{\partial x_j}+\frac{\partial \langle U_j\rangle}{\partial x_i}-\frac{2}{3}\frac{\partial \langle U_k\rangle}{\partial x_k}\delta_{ij}-\rho\overline{u_i'u_j'}\right)\right]. \tag{2.42}$$

- Reynolds averaged conserving scalar equation

$$\rho\frac{\partial \langle \theta\rangle}{\partial t}+\rho\langle \theta\rangle\frac{\partial \langle U_j\rangle}{\partial x_J}=\frac{\partial}{\partial x_j}\left(D\frac{\partial \langle \theta\rangle}{\partial x_j}-\rho\overline{\theta' u_j'}\right). \tag{2.43}$$

  The above equations contain unclosed terms, stemming from the non-linearity of convective term which should be modeled.

- Turbulent stress tensor or Reynolds stress tensor $\rho\overline{u_i'u_j'}$
- Turbulent scalar flux vector $\rho\overline{\theta' u_j'}$

2.6.2 The turbulence closure models

As denoted in last section, for having a complete solution of the Navier-Stokes equations, the unclosed terms should be modeled with auxiliary relations. Depending on using algebraic or deferential equations, the closure level will be defined. The Most desirable model should be case insensitive, physically based on the turbulence structure and numerically simple, realizable and stable.

There are currently two different levels of modeling available: first order methods known as EVM (Eddy Viscosity Model) and second order methods known as RSM (Reynolds Stress Model). In first order methods, the main assumption is alignment of turbulent small scales and the mean flow. In the second order methods, transport equations should be solved for Reynolds stresses. As in this thesis, the main issue is the large eddy simulation, we will just have a short review on variants of each models level used in RANS context.

2.6.2.1 First order models (EVM)

The first order models are known as EVM (Eddy Viscosity Model). The main assumption is that in a turbulent flow the Reynolds stresses and the mean strain rate are in alignment in the same way as viscous stresses. In a Newtonian fluid the molecular viscosity (ν) will be substituted with a turbulent viscosity (ν_t). This approach is known as Boussinesq approximation. The same assumption will be also used for scalar fluxes, known as EDM (Eddy Diffusivity Model).

- The deviatoric part of Reynolds stresses is

$$-\rho\overline{u_i'u_j'}+\frac{2}{3}\rho k\delta_{ij}=\rho\nu_T\left(\frac{\partial \langle U_i\rangle}{\partial x_j}+\frac{\partial \langle U_j\rangle}{\partial x_i}\right), \tag{2.44}$$

  in which ν_T is the turbulent viscosity.

- The turbulent scalar flux vector is

$$\rho\overline{\theta' u'_j} = -D_T \nabla \langle\theta\rangle\,, \tag{2.45}$$

with D_T as turbulent diffusivity.

By using Boussinesq approximation, analogy between turbulent and molecular fluxes, it is possible to introduce effective values

$$\begin{aligned} \nu_{eff} &= \nu + \nu_T && (2.46) \\ D_{eff} &= D + D_T, && (2.47) \end{aligned}$$

by substituting the effective values with molecular values, The EVM model transport equations is now similar to laminar flows and the closure problem is then reduced to finding the appropriate eddy viscosity/diffusivity coefficients. The important difference between eddy viscosity/diffusivity coefficients and molecular viscosity/diffusivity is that those are flow properties rather than being local fluid properties.

2.6.2.2 Turbulent eddy viscosity/diffusivity approximation

To approximate the turbulent viscosity/diffusivity one can rely also to the analogy between local properties and the turbulent ones. The molecular viscosity of a fluid can be related to the average of molecules speed and the mean free path between them, this can be used for approximation of turbulent properties. The turbulent viscosity can be defined as a proportionality of a turbulence length scale and a characteristic time or velocity scale.

$$\begin{array}{cccc} \nu_T & \propto & L & U \\ [\frac{L^2}{T}] & & [L] & [\frac{L}{T}]. \end{array} \tag{2.48}$$

This principle is used in diverse models in order to calculate the turbulent viscosity/diffusivity. As in this thesis the main topic is Large Eddy Simulation; we will just outline the models for RANS.

Model	**Lenght scale** L	**Velocity scale** U	
Algebraic	$\ell/\delta \approx 0.0075$	$\left\vert \ell \frac{du}{dy} \right\vert$	Prandtl [31]
	$ky\left[1 - exp\left(-\frac{y^+}{A^+}\right)\right]$, $A^+ = 26$	$\left\vert \ell \frac{du}{dy} \right\vert$	Van Driest [32]
One equation	As mixing lenght models	T.E^a for k	Cebeci & Smith [33]
Two equations	T.E for a scale-providing variable	T.E for k	Hanjalic & Launder [34]

[a] T.E: Transport equation

Table 2.1: Diverse models for turbulent viscosity/diffusivity.

The different approaches to obtain the characteristic length and time scales are gathered in the Tab.2.1, depending on the order of complexity of the model. It shows that one can only use algebraic model for both characteristic time and length scales or use one or two auxiliary equations to obtain the required scales.

The two equations model is the most popular turbulence model which is used in industry, here the length scale is calculated via solving another transport equation for a variable, it can be the length scale L as introduced by Rotta [35], which in fact was not very applicable or another variable like turbulent energy dissipation rate ε introduced by Davidov. The length and time scales can be constructed by solving two equations for k and ε as proposed by Jones and Launder [36] as standard $k-\varepsilon$ model. There exist also different two equations models in which the main difference to standard $k-\varepsilon$ model is choosing the scale providing variable under different motives. A summary of three popular models can be seen in Tab.2.2.

Model	**scale-providing variable**	**(Dis)advantages**	
$k-\varepsilon$	Turbulent dissipation rate ε	- Near wall	Jones & Launder [36]
$k-\omega$	Char. turbulent frequency $\omega = \varepsilon/k$	- B.C at free boundaries	wilcox [37]
SST model	ω or ε	+Switching	Menter [38]

Table 2.2: Different two equations models, based on the scale-providing variable approach.

2.6.2.3 Linear eddy viscosity models characteristics

Turbulent eddy viscosity/diffusivity models, specially $k-\varepsilon$ models are implemented in standard engineering CFD tools and widely being used. The reason may be the simplicity and applicability of implementing into existing numerical codes. But beside these advantages we are also faced to very obvious shortcomings stemming from the assumptions and simplifications which are done. The most popular deficiencies of models are like:

- Linear algebraic stress-strain alignment assumption that leads to poor predictions in flows in which the stress transport plays a major role, e.g.: flow encountering separation and none equilibrium rapidly developing flows.

- Very poor or totally wrong prediction in flows with rotation or strong streamline curvature, flows facing to adverse pressure gradients, etc.

The shortcomings listed above, are some characteristics of complex flows, which make the obvious differences to thin shear layer approximations used to calibrate the eddy diffusivity models. Some cases as rotation, multi-phase and compressibility can be handled with problem specific additional equations and terms, but there exist other cases, in which the model is expected to be able to predict the physical phenomena by itself; like recirculation, separation and secondary flows.

It is well known that there is no eddy viscosity type model which can generally satisfy the all turbulence specific problems. In RANS context other possibility for handling the turbulence closure is the exact treatment of turbulence production term via solution of a separate transport equation for all turbulent stress components (Second order model).

2.6.2.4 Second order models (RSM)

In second moment models, the modeling will be shifted to higher order correlations, as we will solve the transport equations for the Reynolds stresses and turbulent fluxes. As normally the higher order moments have smaller effect on the mean flow properties, one can state that the turbulence production terms are being treated exactly. Hence the advantage is that the solving the transport equation for all components of turbulent stresses let us to have better prediction in flows encountering system rotation and other body forces, or other types of anisotropy which are main source of turbulence energy. But it should also be clear that, the computation cost is higher than EVM methods as we need to solve more equations and model the more terms.

- Reynolds stress transport equations

$$\begin{aligned}\frac{D\overline{u'_i u'_j}}{Dt} = \underbrace{\frac{\partial \overline{u'_i u'_j}}{\partial t}}_{L_{ij}} + U_k\underbrace{\frac{\partial \overline{u'_i u'_j}}{\partial x_k}}_{C_{ij}} &= -\underbrace{\left(\overline{u'_i u'_k}\frac{\partial U_j}{\partial x_k} + \overline{u'_j u'_k}\frac{\partial U_i}{\partial x_k}\right)}_{P_{ij}} + \underbrace{\left(\overline{f_i u'_j} + \overline{f_j u'_i}\right)}_{G_{ij}} \\ &\underbrace{-2\Omega_k\left(\overline{u'_j u'_m}\varepsilon_{ikm} + \overline{u'_i u'_m}\varepsilon_{jkm}\right)}_{R_{ij}} + \underbrace{\overline{\frac{P}{\rho}\left(\frac{\partial u'_i}{\partial x_j} + \frac{\partial u'_j}{\partial x_i}\right)}}_{\Phi_{ij}} \underbrace{-2\nu\overline{\frac{\partial u'_i}{\partial x_j}\frac{\partial u'_j}{\partial x_i}}}_{\varepsilon_{ij}} \\ &+ \underbrace{\frac{\partial}{\partial x_k}\left[\underbrace{\nu\frac{\partial \overline{u'_i u'_j}}{\partial x_k}}_{D^{\nu}_{ij}} - \underbrace{\overline{u'_i u'_j u'_k}}_{D^{t}_{ij}} - \underbrace{\overline{\frac{P}{\rho}(u'_i\delta_{jk} + u'_j\delta_{ik})}}_{D^{p}_{ij}}\right]}_{D_{ij}}\end{aligned} \tag{2.49}$$

In the table 3.3 we can see which terms should be modeled and which terms can be handled as exact. The important turbulent production terms can be solved exactly without need of extra models; this gives the RSM model the possibility to handle complex flows. The outline in table 3.3 is just for basic RSM model, the advanced methods are not addressed in this thesis.

2.6.2.5 The Algebraic Reynolds stress/Scalar Flux models

- The Algebraic Reynolds stress model

The RSM equations can be simplified by neglecting some terms, as suggested by Rodi [41]. The weak equilibrium assumption is that the time and space evolution of the stress anisotropy tensor is equal to zero, for homogenous flows.

$$\begin{aligned} a_{ij} &= \frac{\overline{u'_i u'_j}}{k} - \frac{2}{3}\delta_{ij} \\ \frac{Da_{ij}}{Dt} &- D_{ij}a_{ij} = 0 \end{aligned} \tag{2.50}$$

	Term	Physical meaning	Solution
Production	P_{ij}	Mean flow deformation	Exact
	G_{ij}	Body force	Exact
	R_{ij}	Rotation force	Exact
Pressure redistribution	Φ_{ij}	Pressure strain	M[a]:split to slow & rapid terms
	Φ^s_{ij}	Slow term	M:$-C_1\varepsilon\left(\frac{\overline{u'_iu'_j}}{k}-\frac{2}{3}\delta_{ij}\right)$Rotta (1951)
	Φ^r_{ij}	Rapid term	M:$-C_2\left(P_{ij}-\frac{2}{3}\delta_{ij}P\right)$ Naot et al [39]
Viscous destruction	ε_{ij}	Stress dissipation rate	M: $(\varepsilon_{ij}=\frac{2}{3}\varepsilon\delta_{ij})$
Diffusive transport	D^{ν}_{ij}	Viscose	Exact
	D^t_{ij}	Turbulent velocity	M: GGD, or SGD shir[40]
	D^p_{ij}	Pressure fluctuations	M

[a] M: Model

Table 2.3: RSM Terms

Using this simplification, and implementing the models used in Basic RSM, we can write an algebraic expression for stress tensors in implicit form

$$\overline{u'_iu'_j}=\frac{k}{\varepsilon}\left[\alpha_1\left(P_{ij}-\frac{2}{3}P\delta_{ij}\right)+\alpha_2\left(G_{ij}-\frac{2}{3}G\delta_{ij}\right)\right]+\frac{2}{3}\delta_{ij}k, \tag{2.51}$$

in which the α_1 and α_2 contain coefficients of pressure strain term of basic RSM equation. Implicit form of stress tensors may lead to numerical instabilities, therefore explicit form of ARSM are proposed, which mostly are similar to none-linear eddy viscosity models.

2.7 Large eddy simulation

Large-eddy simulation is an approach to resolve the larger three-dimensional turbulent eddies directly and model the smaller scales (See Fig.2.2). LES is dominantly more accurate than Reynolds-stress models for flows in which are faced to vortex shedding and unsteady separation because of resolving the large unsteady eddies explicitly. As seen in last section DNS is expected to be not applicable to flows with high Reynolds number because the computational expense increases as the cube of Reynolds number, LES computational cost lies between Reynolds stress and DNS.

LES is based on the concept of filtering, in which the large filtered motion will be directly resolved. For example the instantaneous velocity $\mathbf{U}(x,t)$ will be decomposed into two components, the resolved component $\overline{\mathbf{U}}(x,t)$ and a subgrid scale component $u'(x,t)$. The next step is to derive the filtered Navier-Stokes equations which are just like normal Navier-Stokes equation for resolved component plus the extra subgrid scale stress tensor term, arising from residual motions. The SGS stress tensor also needs a closure as like as Reynolds stress tensor in RANS approach, this closure can be as simple as an eddy-viscosity model, which lies on the isotropy assumption of small motions or more complicated models.

2.7.1 Filtering

In LES the equations will be filtered by volume averaging. Implying on a random field $\phi(x,t)$ we get a spatial and temporal filtered random field. The filtered field is defined as:

$$\overline{\phi}(x,t) = \int_{-\infty}^{\infty}\int_{-\infty}^{\infty} \phi(r,t')\mathbf{G}(x-r,t-t')dt'dr, \tag{2.52}$$

in which $\mathbf{G}$ is the filter convolution kernel function which has the cut off length Δ_c and cut off time scale τ_c. Smaller motions will not be resolved and should be modeled. In a simple one dimension coordinate, filter function for a box filter with width of Δ could be written as:

$$G_B(r) = \begin{cases} 1/\Delta & if \quad r < \Delta/2 \\ 0 & if \quad r > \Delta \end{cases}$$

$$\int_{-\infty}^{\infty} G_B(r)dr = 1.$$

The filtered field could be written as:

$$\overline{\phi} = \frac{1}{\Delta x}\int_{x-\frac{1}{2}\Delta x}^{x+\frac{1}{2}\Delta x} \phi(r,t)dr, \tag{2.53}$$

box filter delivers the $\overline{\phi}(x)$ simply as average of $\phi(x')$ in the interval of $x - \frac{1}{2}\Delta < x' < x + \frac{1}{2}\Delta$. It should be clear that when using box filter, $\overline{\phi'} \neq 0$ and also $\overline{\overline{\phi}} \neq \overline{\phi}$ contrary to RANS approach.

In a spectral space filtering procedure is simple, the contribution larger than cut-off wave number $\kappa_c = \pi/\Delta$ will be set to zero . The $\widehat{G}_c$ is defined as:

$$\widehat{G}_c = \begin{cases} 1/\Delta & if \quad \kappa \le \kappa_c \\ 0 & if \quad \kappa > \kappa_c \end{cases} . \tag{2.54}$$

If one use the Fourier transformation and convolution theorem using cut-off filter to filter twice, it can be showed that:

$$\overline{\widehat{\phi}}(\kappa) = \widehat{\overline{\phi}}(\kappa) = \widehat{G}_c(\kappa)\widehat{\phi}(\kappa), \tag{2.55}$$

$$\overline{\overline{\widehat{\phi}}} = \widehat{G}_c\widehat{G}\widehat{\phi} = \overline{\widehat{\phi}}, \tag{2.56}$$

thus, here contrary to box filter and similar to RANS approach, we get the same results when we filter twice.

The spectral filter is sharp in wave number space and none local in physical space; for the box filter is exactly vice versa as can be seen in Fig.2.3 and Fig.2.4 [26]. In finite volume methods implicit box filtering is used which means that the filter size is as same as the discretized control volume.

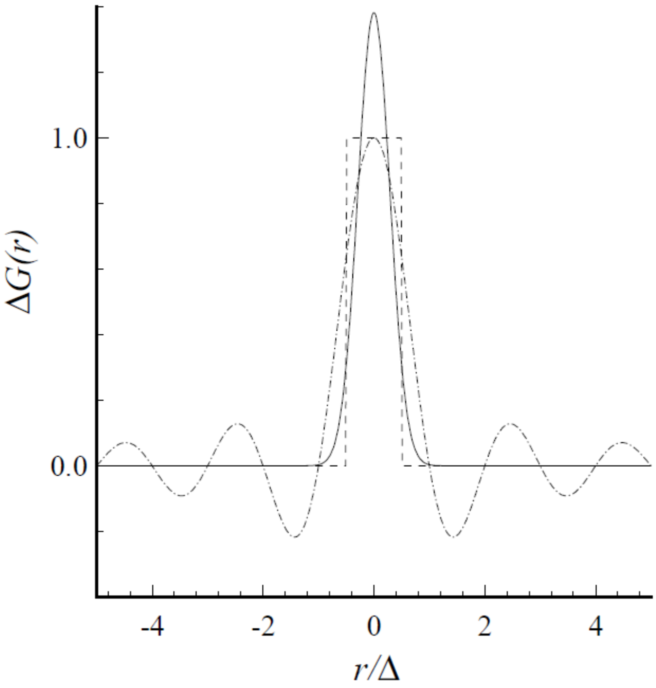

Figure 2.3: Filter transfer function G(r) in physical space: box filter, dashed line; Gaussian filter, solid line; sharp spectral filter, dot-dashed line [26].

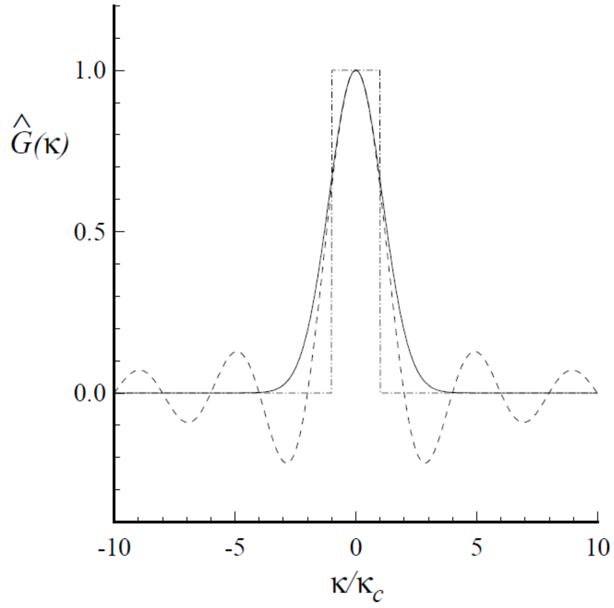

Figure 2.4: Filters $\widehat{G}(\kappa)$ in wave number space: box filter, dashed line; Gaussian filter, solid line; sharp spectral filter, dot-dashed line [26].

2.7.1.1 Filtered transport equations

The filtered Navier-Stokes equations (Eq.2.8) can be written as:

$$\frac{\partial\overline{\mathbf{U}}_j}{\partial t} + \frac{\partial\overline{\mathbf{U}}_i\overline{\mathbf{U}}_j}{\partial x_i} = -\frac{1}{\rho}\frac{\partial\overline{\mathbf{P}}}{\partial x_j} + \nu\frac{\partial^2\overline{\mathbf{U}}_j}{\partial x_i\partial x_i} - \frac{\partial\tau_{ij}^{sgs}}{\partial x_i} \tag{2.57}$$

$$\tau_{ij}^{sgs} = \overline{\mathbf{U}_i\mathbf{U}_j} - \overline{\mathbf{U}}_i\overline{\mathbf{U}}_j, \tag{2.58}$$

which can be also decomposed as proposed by Germano [42]:

$$\tau_{ij}^{sgs} = L_{ij}^o + C_{ij}^o + R_{ij}^o, \tag{2.59}$$

in which the Leonard stresses are:

$$L_{ij}^o \equiv \overline{\overline{\mathbf{U}}_i\overline{\mathbf{U}}_j} - \overline{\overline{\mathbf{U}}}_i\overline{\overline{\mathbf{U}}}_j, \tag{2.60}$$

the cross stresses are:

$$C_{ij}^o \equiv \overline{\overline{\mathbf{U}}_i\overline{\mathbf{u}'}_j} + \overline{\overline{\mathbf{u}'}_i\overline{\mathbf{U}}_j} - \overline{\overline{\mathbf{U}}}_i\overline{\mathbf{u}'}_j - \overline{\mathbf{u}'}_i\overline{\overline{\mathbf{U}}}_j, \tag{2.61}$$

and SGS Reynolds stresses are:

$$R_{ij}^o \equiv \overline{u_i'u_j'} - \overline{u'}_i\overline{u'}_j, \tag{2.62}$$

this decomposition is Galilean invariant. The original decomposition is offered by Leonard [43], in which the components are not generally Galilean invariant. We will explain the later decomposition in the section which the scale similarity subgrid scale model is discussed (Sec.2.7.2.3).

Fig.2.5 shows the LES filtered and non filtered fields. The LES filtered fields, contrary to the RANS fields show statistical behavior as the non filtered fields. The $\overline{U}(x,t)$ follows the trend of $U(x,t)$ although the small length scales are missing. The small scales are illustrated in the residual field $\overline{u'}(x,t)$ and the filtered residual field is non-zero.

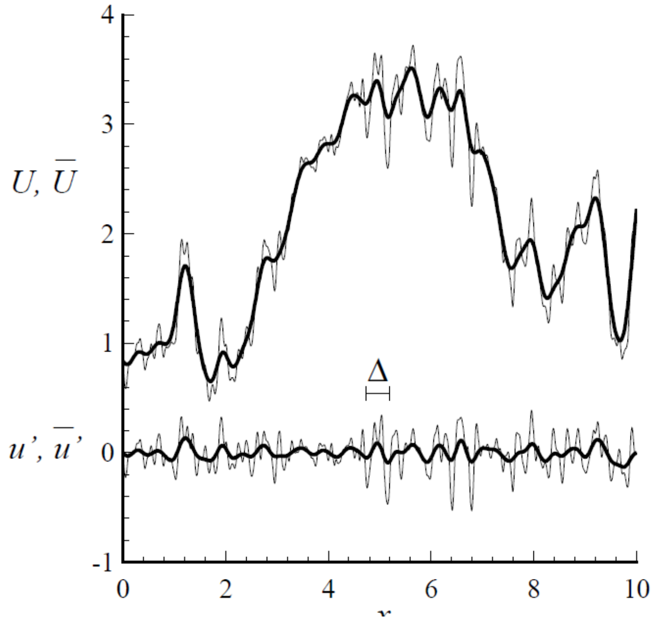

Figure 2.5: Filtered field $\overline{U}(x,t)$ (bold line), using the Gaussian filter with $\Delta \approx 0.35$. Lower curves: residual field $u'(x)$ and the filtered residual field $\overline{u'}(x,t)$ (bold line)[26].

Similar to the momentum equation (Eq.2.57), the filtered transport equation for a passive scalar reads as below:

$$\frac{\partial\overline{\theta}}{\partial t}+\frac{\partial}{\partial x_k}\overline{\theta}\,\overline{\mathbf{U}}_k=\frac{\partial}{\partial x_k}\left(D\frac{\partial\overline{\theta}}{\partial x_k}-J_k^{sgs}\right), \tag{2.63}$$

in which the D is molecular diffusivity and J_k^{sgs} is the residual scalar fluxes

$$J_k^{sgs}=\overline{\theta U}_k-\overline{\theta}\,\overline{\mathbf{U}}_k, \tag{2.64}$$

which also can be decomposed as like as SGS momentum stress tensor and needs a closure.

The filtered equations (Eq.2.57, Eq.2.63) are unclosed; the SGS terms (Eq.2.62, Eq.2.64) should be modeled. In the following section we will review some closure approaches for Large Eddy Simulation.

2.7.2 Subgrid scale modeling

As discussed in last section, the unresolved term should be modeled. Subgrid scale fluxes should be properly estimated to describe the energy transfer from the resolved to subgrid scales which means damping the resolved turbulent fluctuations. In this way, different approaches are being tried and are available. To model the SGS tensor, similar to RANS approach one need to know the time and length scale which the latest is grid scale in LES. The time scale can be approximated from two different approaches:

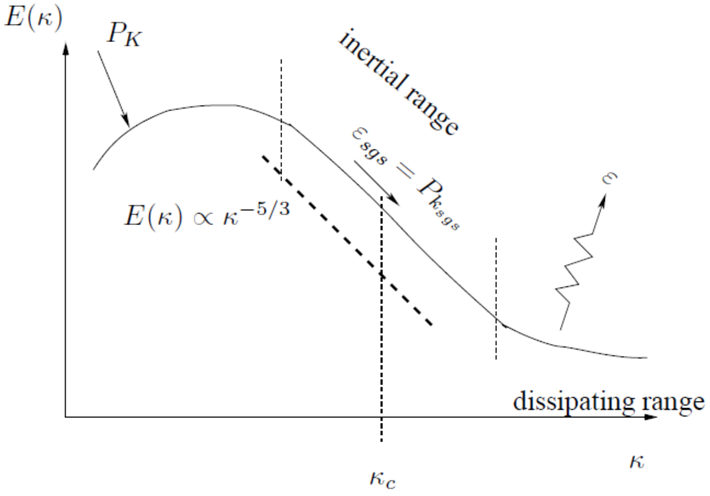

Figure 2.6: Local equilibrium in inertial sub-range $P_{k_{sgs}} = \varepsilon_{sgs}$ [45].

- resolved strain-rate like eddy viscosity/diffusivity models
- subgrid kinetic energy

These models can be as simple as eddy viscosity/diffusivity which is based on the isotropy of the small scales or more complex approaches like second order, anisotropy or nonlinear models. Here comes the question if it is more convenient to use a simple algebraic closure with very fine grid or higher-order models with a moderate grid.

2.7.2.1 Smagorinsky model

The simplest closure for the unresolved SGS fluxes is the Smagorinsky model [44]. The Smagorinsky model is based on the local equilibrium assumption, which means that there is a balance between production term in SGS kinetic energy equation and the viscous dissipation $P_{k_{sgs}} = \varepsilon_{sgs}$ in the inertial sub-range following Kolmogorov's second similarity hypothesis (See Fig.2.6).

The unresolved SGS stress tensor is modeled in which the alignment with the resolved strain rate tensor $\overline{S}_{ij}$ via SGS turbulent viscosity is invoked. The Smagorinsky model is similar to the Prandtl mixing length model [31] used in RANS context :

$$\tau_{ij}^{sgs} = -2\nu_{sgs}\overline{S}_{ij} + \frac{1}{3}\delta_{ij}\tau_{kk}, \tag{2.65}$$

in which SGS viscosity is:

$$\nu_{sgs} = (\mathbf{C}_s\Delta)^2 \left|\bar{s}\right|. \tag{2.66}$$

The filter-width Δ is the local grid size, assumed to be the turbulent length scale:

$$\Delta = (\Delta V_{ijk})^{1/3}$$

and $\mathbf{C}_s$ is the "Smagorinsky constant", which is in realty not constant and flow dependant, it varies in the range of $\mathbf{C}_s$=0.065 to 0.25. The filtered strain rate tensor is:

$$\overline{S}_{ij} = (\frac{\partial \overline{\mathbf{U}}_i}{\partial x_j} + \frac{\partial \overline{\mathbf{U}}_j}{\partial x_i}), \tag{2.67}$$

and the scalar $|\bar{s}|$, the reciprocal of turbulent time scale is also:

$$|\bar{s}| = \sqrt{2\overline{S}_{ij}\overline{S}_{ij}}.$$

As the gradient of velocity near the wall becomes very large, the SGS viscosity also increases, which in reality should approach to zero as the SGS turbulent fluctuations are zero at the wall. Therefore, to avoid this this problem a damping function should be used to set the model constant zero at the walls:

$$\mathbf{C}_s = \mathbf{C}_0(1 - e^{\frac{-y^+}{25}})^2 \tag{2.68}$$

The Smagorinsky model for scalar fluxes (Erlebacher et al.[46]) is:

$$\begin{aligned} J_k^{sgs} &= -D_t \frac{\partial \overline{\theta}}{\partial x_k} \\ D_t &= C_\theta \Delta^2 \, |\bar{s}| \\ C_\theta &= \frac{C_s}{Pr_t} \end{aligned} \tag{2.69}$$

The C_θ is assigned as contribution of C_s and turbulent Prandtl/Schmidt number. The C_θ is prescribed in this model and has a value in the range $0.5 - 0.7$ for air.

2.7.2.2 Dynamic eddy viscosity model

In the model proposed by Germano et al.[18], the constant $\mathbf{C}_s$ will be computed from the resolved velocity field. The disadvantage of choosing an arbitrary constant will be overcome, the near wall damping is covered and transitional field could be handled.

The concept is to use the Smagorinsky model at two different grid levels (See Fig.2.7) and to calculate the constant from the error minimization using least square method.

As we assume that filter width is same as grid size, we apply two filters to momentum equation (Eq.2.8), one with grid filter (Eq.2.57) and second one using a coarser filter which we name it as the test filter where $\widetilde{\Delta} = 2\Delta$, we have:

$$\frac{\partial \widetilde{\overline{\mathbf{U}}}_j}{\partial t} + \frac{\partial \widetilde{\overline{\mathbf{U}}}_i \widetilde{\overline{\mathbf{U}}}_j}{\partial x_i} = -\frac{1}{\rho}\frac{\partial \widetilde{\overline{\mathbf{P}}}}{\partial x_j} + \nu \frac{\partial^2 \widetilde{\overline{\mathbf{U}}}_j}{\partial x_i \partial x_i} - \frac{\partial T_{ij}^{sgs}}{\partial x_i}, \tag{2.70}$$

where the SGS stress at test filter level is:

$$T_{ij}^{sgs} = \widetilde{\overline{\mathbf{U}_i \mathbf{U}_j}} - \widetilde{\overline{\mathbf{U}}}_i \widetilde{\overline{\mathbf{U}}}_j, \tag{2.71}$$

which also can be reformed as:

$$T_{ij}^{sgs} = \widetilde{\tau}_{ij}^{sgs} + \widetilde{\overline{\mathbf{U}}_i \overline{\mathbf{U}}_j} - \widetilde{\overline{\mathbf{U}}}_i \widetilde{\overline{\mathbf{U}}}_j. \tag{2.72}$$

Both $\tilde{\tau}_{ij}^{sgs}$ and T_{ij}^{sgs} contain unresolved terms but the difference "The dynamic Leonard stresses" are explicitly computable from resolved stresses:

$$L_{ij} = T_{ij}^{sgs} - \tilde{\tau}_{ij}^{sgs}, \tag{2.73}$$

The dynamic Leonard stresses are corresponding to the stresses with length scale l in the range of $\Delta < l < \widetilde{\Delta}$. The Smagorinsky model for the test filter is:

$$T_{ij}^{sgs} - \frac{1}{3}\delta_{ij}T_{kk}^{sgs} = -2\mathbf{C}\widetilde{\Delta}^2 \left|\tilde{\bar{s}}\right| \tilde{\bar{S}}_{ij}, \tag{2.74}$$

applying the test filter and substituting the Eq.2.74 in Eq.2.73 delivers:

$$L_{ij} - \frac{1}{3}\delta_{ij}L_{kk} = -2C(\widetilde{\Delta}^2 \left|\tilde{\bar{S}}\right| \tilde{\bar{S}}_{ij} - \Delta^2 \widetilde{|\bar{S}|\,\bar{S}_{ij}}). \tag{2.75}$$

Germano et al.[18] used a least-square method to find the C, the error is defined as:

$$Q = (L_{ij} - \frac{1}{3}\delta_{ij}L_{kk} + 2CM_{ij})^2, \tag{2.76}$$

in which

$$M_{ij} = (\widetilde{\Delta}^2 \left|\tilde{\bar{S}}\right| \tilde{\bar{S}}_{ij} - \Delta^2 \widetilde{|\bar{S}|\,\bar{S}_{ij}}). \tag{2.77}$$

The error, Q has an extrema in $\partial Q/\partial C = 0$ and $\partial^2 Q/\partial C^2 = 8M_{ij}M_{ij} > 0$,
the C_{dyn} can be defined as:

$$C_{dyn} = -\frac{L_{ij}M_{ij}}{2M_{ij}M_{ij}}. \tag{2.78}$$

This dynamic coefficient has a wide fluctuation range and it should be averaged and limited.

The dynamic model is also applicable to scalar flux to extrapolate the values at subgrid scales from resolved field, all under scale similarity assumption. The same procedure will be applied to scalar flux and as result the dynamic turbulent Prandtl/Schmidt number read as proposed by Cabot and Moin [47]:

$$Sc_t = \frac{L_{ij}M_{ij}}{2M_{ij}M_{ij}}\frac{H_iH_i}{F_iH_i} \tag{2.79}$$

$$\begin{aligned}
C_{\theta_{dyn}} &= -\frac{F_iH_i}{H_iH_i} \\
\mathit{where} & \\
F_i &= \widetilde{\bar{\theta}\,\bar{\mathbf{U}}_k} - \tilde{\bar{\theta}}\widetilde{\bar{\mathbf{U}}}_k \\
H_i &= \widetilde{\Delta}^2\left|\tilde{\bar{S}}\right|\frac{\partial\tilde{\bar{\theta}}}{\partial x_k} - \Delta^2 \widetilde{|\bar{S}|\,\frac{\partial\bar{\theta}}{\partial x_k}}.
\end{aligned} \tag{2.80}$$

Applications show that using dynamic model, LES can be performed without the need of near wall damping functions and fixed model constants.

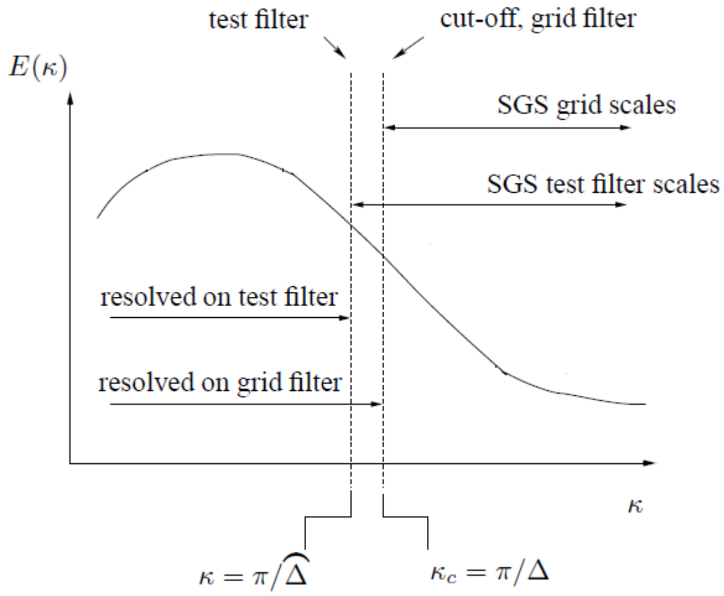

Figure 2.7: Grid filter and test filter in the energy spectrum [45].

2.7.2.3 Scale similarity models

The basic idea of this model is to use the scale similarity of scales just above and below the cut off wave number. The first step is to decompose the SGS stress $\tau_{ij}^{sgs} = \overline{\mathbf{U}_i\mathbf{U}_j} - \overline{\mathbf{U}}_i\overline{\mathbf{U}}_j$ as:

$$\begin{aligned} \tau_{ij}^{sgs} &= L_{ij} + C_{ij} + R_{ij} \\ L_{ij} &= \overline{\overline{\mathbf{U}}_i\overline{\mathbf{U}}_j} - \overline{\mathbf{U}}_i\overline{\mathbf{U}}_j \\ C_{ij} &= \overline{\overline{\mathbf{U}}_i u'_j} + \overline{\overline{\mathbf{U}}_j u'_i} \qquad (2.81) \\ R_{ij} &= \overline{u'_i u'_j}, \end{aligned}$$

this decomposition is offered by Leonard [43] which as stated before is not generally Galilean invariant. The advantage of this model is that Leonard stresses are directly computable, but the cross term and Reynolds term should be modeled, the cross stress is also responsible for interaction of resolved and modeled scales.

$$\begin{aligned} C_{ij}^{M} &= c(\overline{U}_i\overline{U}_j - \overline{\overline{U}}_i\overline{\overline{U}}_j) \\ R_{ij}^{M} &= -2C_s^2\Delta^2|\bar{s}|\,\overline{S}_{ij} \qquad (2.82) \end{aligned}$$

The model is called mixed similarity model (Jaberi [48]) and the SGS stress will be computed as:

$$\tau_{ij}^{msim} = -2C_s^2\Delta^2|\bar{s}|\,\overline{S}_{ij} + C_{sim}(\overline{\overline{\mathbf{U}}_i\overline{\mathbf{U}}_j} - \overline{\overline{\mathbf{U}}}_i\overline{\overline{\mathbf{U}}}_j), \qquad (2.83)$$

note that here the second term $C_{sim}(\overline{\overline{\mathbf{U}}_i\overline{\mathbf{U}}_j} - \overline{\overline{\mathbf{U}}}_i\overline{\overline{\mathbf{U}}}_j)$ is:

$$L_{ij}^{o} = L_{ij} + C_{ij}^{M}, \qquad (2.84)$$

which is Galilean invariant. The original scale similarity model offered by Bardina et al.[49] is consisting of just the second part of τ_{ij}^{msim}, which is not sufficiently dissipative and therefore the eddy viscosity term has to be added. Fig.2.8 shows the effect of filtering on energy spectrum, same goes also to models which are not sufficiently dissipative; the energy pills up in inertial sub-range and the model cannot predict the SGS scales properly.

The SGS scalar flux also can be computed via scale similarity model :

$$J_k^{sgs} = D_{sim}(\overline{\overline{\theta}\,\overline{\mathbf{U}}_k} - \overline{\overline{\theta}}\,\overline{\overline{\mathbf{U}}}_k), \tag{2.85}$$

but as same as dissipation problem in SGS momentum closure, the mixed models, Jaberi et al.[48] used an eddy viscosity model to make the scale similarity model dissipative

$$J_k^{sgs} = D_{ted}\frac{\partial\overline{\theta}}{\partial x_k} + D_{sim}(\overline{\overline{\theta}\,\overline{\mathbf{U}}_k} - \overline{\overline{\theta}}\,\overline{\overline{\mathbf{U}}}_k) \tag{2.86}$$

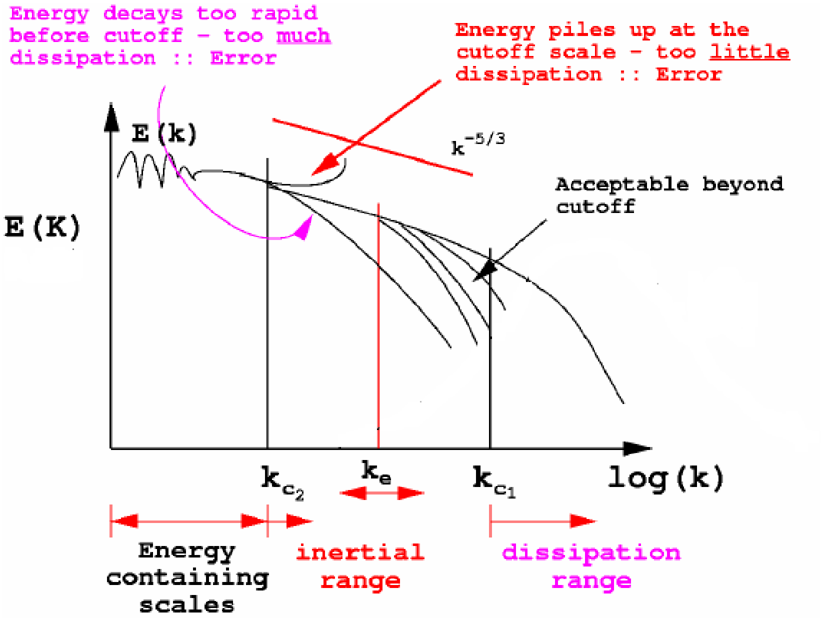

Figure 2.8: Impact of filtering on the energy spectrum [28].

As in isotropic eddy viscosity/diffusivity assumptions, the SGS fluxes are assumed to be aligned with the resolved strain rate, it cannot predict all components of the subgrid stresses properly. In the next section we will review some more general models to overcome this disadvantage.

2.7.2.4 Dynamic SGS turbulent kinetic energy model

At cut-off, SGS turbulent kinetic energy is dissipated from the resolved turbulence and transfers to smaller scales in a cascade effect and acts as a production term in the SGS turbulent kinetic energy equation. To estimate the subgird time scale one can also use an one equation to model the SGS turbulent kinetic energy, Schumann [50], Menon et al.[51], and Yoshizawa and Horiuti [52] which reads as:

$$\frac{\partial k_{sgs}}{\partial t} + \frac{\partial \overline{\mathbf{U}}_j \partial k_{sgs}}{\partial x_j} = P_{k_{sgs}} - \varepsilon_{k_{sgs}} + \frac{\partial}{\partial x_j}(\nu_{eff}\frac{\partial k_{sgs}}{\partial x_j}), \tag{2.87}$$

in which $P_{k_{sgs}}$ production term, $\varepsilon_{k_{sgs}}$ dissipation and third term on the right hand side is diffusion of k_{sgs}:

$$\begin{aligned} P_{k_{sgs}} &= -\tau_{ij}\frac{\partial \overline{\mathbf{U}}_j}{\partial x_j} \\ \varepsilon_{k_{sgs}} &= C_\varepsilon \frac{k_{sgs}^{3/2}}{\overline{\Delta}}. \end{aligned} \tag{2.88}$$

The SGS stress tensor is also:

$$\begin{aligned} \tau_{ij}^{sgs} - \frac{1}{3}\tau_{kk}^{sgs}\delta_{ij} &= -2\nu_\tau \overline{S}_{ij} \\ \nu_\tau &= C_k \overline{\Delta} k_{sgs}^{1/2}, \end{aligned} \tag{2.89}$$

where k_{sgs} is defined as:

$$k_{sgs} = \overline{\mathbf{U}_k \mathbf{U}_k} - \overline{\mathbf{U}}_k \overline{\mathbf{U}}_k = \frac{1}{3}\tau_{kk}^{sgs}. \tag{2.90}$$

The coefficients C_ε and C_k should be find dynamically.

Chapter 3

Numerical methods

3.1 Introduction to numerical methods

The choice of an appropriate mathematical model is the essential initial point of any numerical model. As to know, it is has been shown that a general purpose solution is not practical. Depending on the targeted application, one should choose the appropriate numerical method. Beyond the wide scope of applications, the target application normally will be divided to the reacting and non-reacting processes in compressible and incompressible forms. The technical flows are also labeled to be laminar or turbulent. Comparing to the exact solution of the targeted application, each of these mathematical models includes simplifications.

As described in Chap.2, the turbulent flows can be described with equations either in integral or differential form. These equations apart from special cases have no analytical solution and should be solved numerically. The partial differential equations can be approximated numerically using discretization methods and solving systems of algebraic equations. It is obvious that the accuracy of the numerical solution is then based on the quality of the used discretization method.

The most practiced discretization approaches in the Computational Fluid Dynamics (CFD) are: Finite Difference Method (FDM), Finite Element Method (FEM), Finite Volume Method (FVM) and the spectral methods. In a finite difference method, approximations for the derivatives at the grid points have to be selected. In a finite volume method, one has to select the methods of approximating surface and volume integrals. In a finite element method, one has to choose the shape functions (elements) and weighting functions. There are many possibilities to choose from. The choice influences the accuracy of the approximation. Ultimately if one use a very fine mesh grid, all of these approaches should yield the same result.

The coordinate system is other important issue in the numerical methods. The conservation equations can be written in many forms like cartesian, cylindrical, spherical, curvilinear orthogonal or non-orthogonal systems. The choice of basis is also important (fixed, variable, etc.).

The choice of an appropriate mesh grid type is also crucial for the numerical methods. The grid can be globally structured or unstructured. The main property of the structured grid is that it is logically equivalent to the cartesian grid. Hence each point has six neighbors in three dimensions. The matrix of algebraic equation using structured grid is also structured. The disadvantage may be seen is in level of application which will be restricted to the simple geometries. In opposite in the unstructured grid, the control volumes has no restrict number of neighbors. They can also have an arbitrary shape. The main advantage of using unstructured grid is the flexibility of the grid generation. The local refinement is also no problem using unstructured grid type. The main difficulty is the irregularity of the data structure. The algebraic equation system solver is in comparison to the structured grid is normally slower because the algebraic equation system has no longer diagonal structure.

The software package FASTEST is used within this work. It is fully conservative incompressible Finite-Volume code with a SIMPLE (Semi-Implicit Method for Pressure Linked Equations) type pressure correction scheme that simulates flows in complex three-dimensional configurations. The spatial discretization is of second order, and the time discretization is an explicit Runge-Kutta third order. To assure the boundedness of scalar quantities a TVD (Total Variation Diminishing) limiter is used. The code uses block structured, hexahedral boundary-fitted grids. As the current work is based on using the FASTEST code, we will briefly review the exploited numerical methods.

3.2 Finite Volume Method (FVM)

The Finite Volume Method (FVM) uses the integral form of the conservation equations. The targeted domain is subdivided into a finite number of control volumes, applying the conservation equations on each control volume. Each control volume has a centered computational node for calculation of variable values. The variable values at the control volume surface will be achieved via interpolation of nodal values. The surface and volume integrals should also approximated using appropriate schemes. Using this numerical approach, each control volume will be designated with an algebraic equation, appearing neighbor nodal values.

The finite volume method uses the integral form of the conservation equation as the starting point, considering the generic conservation equation for a quantity ϕ.

$$\int_s \rho\phi v.nds = \int_s Dgrad\phi.nds + \int_\phi q_\phi ds \tag{3.1}$$

The solution domain is subdivided into a finite number of small control volumes (CVs) by a grid. The practical approach is to define CVs using an appropriate grid and assign the computational node to the CV center. One could also define the nodal points first and construct surrounding CVs, in which the CV faces positioned between nodes.

The second order accuracy is the advantage of first method in which nodal values presenting the mean over the CV volume. The second method has a better accuracy in calculation of derivatives at CV faces, as the face is midway of two nodes

The conservation equation in the integral form (Eq.3.1) applies to the all CVs of the whole domain also on the solution. The global conservation equation will be retained if one make a sum over all CVs, omitting the surface integrals over CV faces. As explained before, after approximation of volume and surface integrals, the algebraic equation for each CV can be constructed.

3.2.1 Approximation of surface integrals

In a 3D case, the CV surfaces have six faces. This faces can be shown corresponding to their direction to the central node with (e, w, n, s, t, b). In this case, we can approximate the net flux through each CV as the sum of integrals over all six faces. This reads as:

$$\int_s f ds = \sum_s \int_{s_k} f ds, \tag{3.2}$$

in which f can be either a diffusive ($Dgrad\phi.n$) or convective ($\rho\phi v.n$) term. The approximation of diffusive and convective terms are also shown in the following. For calculation of the surface integral in in Eq.3.2, one needs to approximate the values of ϕ everywhere on the surface S_e using known nodal values. These approximations consist of: The approximation of integrals using one or more values on the cell face and approximation of cell face values using central node values.

The integral can be approximated using midpoint rule as a product of the integrand at the cell face center and the cell face area, in which the integrand at cell face center is one more time an approximation of the mean value over the surface.

$$F_e = \int_s f ds = \overline{f_e} S_e \approx f_e S_e \tag{3.3}$$

The second order accuracy can be achieved using this approximation. As explained before, as the value is not known at the face center, it should be approximated using interpolation. This calculation also should have second order accuracy to preserve the order of midpoint rule.

The midpoint rule is the simplest second-order approximation. Higher-order approximations can be achieved which require the integrand at also other locations beside the cell face center, like center of edges and corners.

3.2.2 Approximation of volume integrals

Some terms in the transport equations require integration over the volume of a CV. One can use the mean value of integrand and the volume of CV to construct an approximation. The product of these two values delivers a second order approximation.

$$Q_p = \int_\Omega q d\Omega = \overline{q} \Delta\Omega \approx q_p \Delta\Omega, \tag{3.4}$$

in which the value of q at the CV central node is assigned to be q_P. The q can calculated using all other variables at central node without any interpolation as all variables are available. If q has an constant or linear variation over the cell, the above approximation will be exact otherwise it has second order error. If higher order approximations are needed, one need to now about more values on more locations rather than cell center. Hence the values should approximated using nodal values.

3.2.3 Treatment of convective and diffusive fluxes

The approximations of the integrals require the values of variables at locations other than computational nodes (CV centers). The integrand, denoted in the previous sections by f, involves the product of several variables and/or variable gradients at those locations: $f^c = \rho\phi \boldsymbol{v}.\boldsymbol{n}$ for the convective flux and $f^d = Dgrad\phi.\boldsymbol{n}$ for the diffusive flux. We assume that the velocity field and the fluid properties ρ and D are known at all locations.

To calculate the convective and diffusive fluxes, the value of ϕ and the gradient normal to the cell face at one or more locations on the CV surface are needed. The volume integrals of the source terms may also require these values. They have to be expressed in terms of the nodal values by interpolation. Numerous possibilities are available; we shall mention the ones which are most commonly used in the FASTEST code. In particular we shall show how the value of ϕ and its normal derivative at the cell face 'e' can be approximated.

- **Convective fluxes**

The linear interpolation between the two nearest nodes is an approximation for the value at CV-face center. At location 'e' on a cartesian grid we have :

$$\phi_e^{CDS} = \phi_E \lambda_e + \phi_P (1 - \lambda_e) \tag{3.5}$$

where the linear interpolation factor λ_e is defined:

$$\lambda_e = \frac{x_e - x_P}{x_E - x_P} \tag{3.6}$$

The value at the surface 'e' is then a sum of weighted values of nodes P and E. For every cartesian grid, the Central Differencing Scheme (CDS) is second order. The truncation error is proportional to the square of the grid. This scheme as other higher order schemes may produce oscillatory solutions. The other problem using this scheme is lack of numerical diffusion which leads to stability problem specially in presence of sharp gradient or jump of a variable.

To overcome this problem the FASTEST code uses the Multi Linear interpolation (MULI) procedure [53]. The MULI-procedure is based on the multi-dimensional Taylor series expansion which uses the additional information of other nodes.

$$\phi_e^{MULI} = \phi_E \lambda_e + \phi_P (1 - \lambda_e) + (\phi_N - \phi_S)\lambda_{NS} + (\phi_T - \phi_B)\lambda_{TB} \tag{3.7}$$

In the MulI-procedure (Eq.3.7) extra terms are existing in comparison to the Central Differencing Scheme (CDS) (Eq.3.5), which consider the alternation of ϕ considering the neighbor cells.

- **Total Variation Diminishing (TVD) scheme**

High order spatial discretization schemes, like MULI-procedure [53] are more accurate for having an smooth interpolated solution. Although they show spurious oscillations in the case of discontinuities like density jump in the reacting flows. A flux limiter can be exploited to make the solutions Total Variation Diminishing (TVD) and limit the spatial derivatives to physically realistic values. The flux limiter can switch between the low precision, high resolution and the high precision, low resolution schemes, depending to the gradients of the targeted cell.

Various flux limiters are proposed in the literature which have different switching characteristics. The selection of a particular flux limiter is based on the problem and solution scheme. Using the Total Variation Diminishing (TVD) scheme, the solution reads as:

$$\phi_f^{TVD} = \phi_c + \frac{|x_{f,i} - x_{C,i}|}{|x_{C,i} - x_{U,i}|}\Psi(r)(\phi_C^l - \phi_U^l), \tag{3.8}$$

in the FASTEST code the CHARM [54] limiter function is used:

$$\Psi(r) = \begin{cases} \frac{r(3r+1)}{(r+1)^2} & \text{if } r > 0 \\ 0 & \text{if } r \leq 0 \end{cases}$$

The r reads as:

$$r = \frac{|x_{C,i} - x_{U,i}|}{|x_{D,i} - x_{C,i}|}\frac{\phi_D^l - \phi_C^l}{\phi_C^l - \phi_U^l}, \tag{3.9}$$

in which the C stands for center, U for upwind and the D for the downwind cells. This TVD limiter will set the order of the used scheme, if r tends to unity we will have CDS and if it tends toward zero we will have pure first order upwind.

- **Diffusive fluxes**

To describe the diffusive fluxes, the spatial gradient of the cell surface should be also known. The FASTEST code uses the DABT method [53] which is also based on the Taylor series expansion. The gradient should be evaluated in corresponding to a local coordinate system ξ_i:

$$\frac{\partial \phi}{\partial x_i} = \frac{\partial \phi}{\partial \xi_j}\frac{\partial \xi_j}{\partial x_i} = \frac{\Psi^{ji}}{J}\phi^j \tag{3.10}$$

in which the Jacobian is the determinant of the transformation matrix $J = det(A_{ij})$.

$$\begin{aligned} \Psi_e^{1j} &= \epsilon_{ikl}\left[(x_{N,k} - x_{S,k} + x_{NE,k} - x_{SE,k})\,(x_{T,l} - x_{B,l} + x_{TE,l} - x_{BE,l})\right] \\ \Psi_e^{2j} &= \epsilon_{ikl}\left[(x_{T,k} - x_{B,k} + x_{TE,k} - x_{BE,k})\,(x_{E,l} - x_{P,l})\right] \\ \Psi_e^{3j} &= \epsilon_{ikl}\left[(x_{E,k} - x_{P,k})\,(x_{N,l} - x_{S,l} + x_{NE,l} - x_{SE,l})\right] \\ \phi_e^1 &= \phi_E - \phi_P \\ J_e &= (x_{E,i} - x_{P,i}) \\ \phi_e^2 &= \phi_N - \phi_S + \phi_{NE} - \phi_{SE} \\ \phi_e^3 &= \phi_T - \phi_B + \phi_{TE} - \phi_{BE} \end{aligned} \tag{3.11}$$

3.3 Time discretization

The time discretization used in this work is the Runge-Kutta procedure. This procedure include more explicit Euler sub-steps with different time steps. In the sub-steps just the state of the problem between two time steps t^n and t^{n+1} will be calculated, the corresponding time step is then defined as: $\Delta_t = t^{n+1} - t^n$. Writing the simplified form of transport equation for the ϕ as:

$$\frac{\partial \phi}{\partial t} = Q(\phi) \tag{3.12}$$

The three stage Runge-Kutta procedure used in FASTEST code reads as:

$$\begin{aligned} \phi^{(1_{RK})} &= \phi^{(n)} + c_1 \Delta_t Q(\phi^n) \\ \phi^{(2_{RK})} &= \phi^{(n)} + c_2 \Delta_t Q(\phi^{(1_{RK})}) \\ \phi^{n+1} &= \phi^{(n)} + c_3 \Delta_t Q(\phi^{(2_{RK})}) \\ c_1 &= \frac{1}{3},\ c_2 = \frac{1}{3},\ c_3 = 1 \end{aligned} \tag{3.13}$$

This procedure consist of two predictor sub-steps. In the first sub-step the state corresponding to the time t^n will be calculated with a time advancement of $c_1\Delta_t$, following a second correction sub-step with time advancement of $c_2\Delta_t$.

For the stability of the explicit time advancement procedure, two indicator are derived using from comparison of time step to the convection and diffusion characteristic time scales. The CFL number is defined as $C = u\Delta_t/\Delta_x$. The CFL number hold in the following calculation always under one, assuring that convective information within time step of Δ_t stays conservative in the control volume of Δ_x.

3.4 Pressure correction

The FASTEST code is based on the law-Mach number assumption for incompressible flows which allow to decouple the pressure and density. Solving the transport equation for momentum and scalars do not lead to conservation of mass. In context of fully compressible flows, one can also explicitly solve the continuity equation. The idea behind law-Mach number assumption let to skip the later step in which is encountered with frequent difficulties and boundary condition implementation problems.

The low-Mach number assumption, exploits the pressure correction procedure. The pressure is used as a correction quantity for the momentum equation. The procedure of pressure correction method is first to solve the momentum equation which lead to temporarily (not corrected) values of velocity. These values will be used to construct the pressure correction equation (Poisson equation). Solving Poisson equation and continuity equation in an iterative procedure leads to conservation of mass.

The iterative procedure used in FASTEST code is based on strongly implicit procedure [55] which uses an Incomplete Lower Upper (ILU) matrix decomposition [56]. The iterative process solves the Poisson equation for pressure correction quantity and updates the reformulated continuity equation. The iterative procedure converges when the computed mass lack is smaller than an appropriate given criteria.

3.5 Boundary conditions

To complete the solution of the transport equations using explained discretization methods, one need also to define appropriate boundary conditions. The different boundary conditions used in this work can be categorized to inlet, outlet and wall boundary conditions.

- **Inlet boundary condition**

The state of all transported quantities are prescribed using the Dirichlet boundary conditions. The scalars are spatially and temporally constant. The velocity inlet boundary condition used in this work is a combination of prescribed velocity profiles and invoking of turbulence using the digital filtering method of Klein et al.[57].

- **Outlet boundary condition**

The outlet boundary condition are treated based on the type of transported quantity. For scalars, the Neumann boundary condition assuming zero gradient condition in boundary normal direction is used.

$$\frac{\partial \phi}{\partial x_i} n_i = 0 \tag{3.14}$$

For the velocity components the Richter et al. [58] proposed method is used. In which the simplified convection equation reads as:

$$\frac{\partial u_i}{\partial t} + u_c \frac{\partial u_i}{\partial x_i} n_i = 0, \tag{3.15}$$

The u_c is a convective velocity which should be prescribed, either in form of an appropriate bulk or a velocity profile. The conservation of the global mass flux is ensured using a scaling factor comparing, the inlet boundary prescribed mass flux subtracted from the mass change due to chemical reaction within domain and the outlet computed mass flux.

- **Wall boundary condition**

The no-slip boundary conditions are invoked on all walls. For species, the zero gradient conditions are applied. The current investigation is based on the adiabatic model.

Chapter 4

Combustion, theory and modeling

4.1 Combustion chemistry

The investigated problem is normally a good indicator for choosing the conducted chemistry level complexity. For instant, simple chemistry and flame front tracking methods can be carried out for prediction of flame characteristics of premixed flames with low turbulence intensity. Nevertheless, most important aspects in the numerical investigation of combustion are the pollutant prediction, flashback and flame blow off and are highly dependent on appropriate and complete chemistry description.

The conduction of a turbulent combustion simulation using full description of chemical reactions are encountered with theoretical and computational difficulties. The first issue is the presence of large spectrum of the chemical time scales, which can not be retained using a single turbulent flow time scale either the integral or Kolmogorov time (Ex.2.19) scales.

Since the combustion chemical reactions are a combination of hundreds of species and up to thousands of reactions, the second issue will be the computational costs. Full description of combustion needs solving a transport equation for each species which also contains complex functions for transport coefficients and source terms in dependency of species mass fraction and temperature. Although the computational resources have increased a lot in last decade, the simulation of a realistic configuration with full detailed chemistry is and will be also in the near future computationally expensive.

To include the reduced chemical schemes for turbulent combustion different strategies are proposed all based on the neglection of very small chemical time scales.

One widely practiced approach is the chemistry reduction using global schemes from complex and full description of the chemical reaction mechanism. The main assumptions for constructing such a global reaction mechanism are quasi steady state of the radicals and some intermediate species and partial equilibrium of some elementary reactions. In this reduction approach the full description of chemistry will be reduced to the solving of the reaction rate with few main species which seems to be computationally affordable. Divers approaches are proposed, as the four step mechanism for methane [59] or a more general one for hydrocarbons [60, 61] or other global schemes for more specific combustion form like the one proposed in [62].

Nevertheless, creation of such global schemes are also encountered with difficulties. Although the number of transport equations are reduced but the complexity and mathematically stiffness of the reaction rates raise. On the other hand derivation of such complex schemes needs very high chemistry knowledge which in case of very complex fuels or specific combustion process are not well matured in the community.

4.1.1 Tabulated chemistry

The other interesting approach which is recently developed and widely used for different configurations is the tabulated chemistry based on the detailed kinetic mechanism. The tabulate chemistry approaches are divided as to now to two categories. The pre computed look-up table and in situ adaptive tabulation (ISAT).

- **Intrinsic Low Dimensional Manifold (ILDM)**

The first approach is Intrinsic Low Dimensional Manifold (ILDM) [63, 64, 65]. In the reduction mechanisms one needs to have a priori knowledge about that which reactions are in partial equilibrium and which species are in steady state. The proposed method automatically separates the slow and fast processes based on the analysis of the chemical source terms. The proposed method needs as input the degree of freedom, corresponding to the number of steps in the reduced scheme beside the detailed kinetic mechanism.

As a function of reduced set of variables (for instant a progress variable) the reaction rate will be stored in look-up table. The look-up table is then coupled to the CFD code and will be searched using multilinear interpolations.

The ILDM approach is shown to have very good results by the correct separation of slow and fast mechanism. Although using complex fuels, one needs to have larger manifolds which normally is less effective. The other problem is that the diffusion process is not included in the mathematical description and the transport process is only based on the reaction rate. The reaction rate is also mainly subject to change by the high temperatures. This leads to problem in low temperature regions which chemistry and diffusive processes are both active.

- **Flame Prolongation of ILDM (FPI) & Flamelet Generated Manifolds (FGM)**

To tackle this problem similar approaches are proposed all based on the describing a multidimensional flame by one-dimensional flamelets. These similar proposed methods are then called ”Flame Prolongation of ILDM” (FPI) [66, 67] and ”Flamelet Generated Manifolds” (FGM) [68, 69] respectively. The principal assumption is that the chemical composition of a one-dimensional flame is similar to the composition of the multi-dimensional flame.

The one-dimensional flamelets are constructed using complex chemical schemes. The look-up table is then constructed using the solution of one-dimensional flamelets and is parametrized with various control variables (mixture fraction, progress variable). The dependent variables, reaction rates and species mass fractions are then tabulated based on the control variables. The proposed methods can be extended with other control variables as enthalpy [70, 71, 72, 73] or variation in the element composition. Nevertheless, adding extra control variables may lead to the look-up tables with very large size. Although there exist some practical solutions to overcome this drawback as using self-similarity of premixed flames to split the table in smaller sub tables [74, 75, 76].

- **In Situ Adaptive Tabulation (ISAT)**

The other approach which is proposed to use the benefits of tabulated chemistry and simultaneously avoid large size tables is the proposed ”In Situ Adaptive Tabulation” (ISAT) [77, 78, 79]. The ISAT approach pledge a decrease by three order of magnitude comparing to the detailed chemistry in combustion. The proposed method is based on the restriction of the table generation to the accessed region of the composition space. The ISAT approach showed to have a speed-up factor of 1000 comparing to the direct integration of the reaction equations. Various numerical speed-up schemes are proposed for the ISAT approach including artificial neural networks and polynomial fits [80, 81].

4.2 Modeling of turbulent premixed flames

4.2.1 Introduction

In Sec.4.1 we have reviewed the possible options to include the chemistry in the CFD (Computational Fluid Dynamics). The remaining issues are the resolution of the flame front (particular for Large Eddy Simulation) and closure problem for the turbulent flows. As already stated in the literature survey (See Sec.1.2), due to the high complexity of the interaction between turbulence and chemistry in different combustion regimes, it still make more sense to describe each particular regime by its own specific combustion model.

As a classical view the combustion regimes are divided to the premixed and the diffusion controlled flames.

4.2.1.1 Diffusion flames

In this regime the fuel and the oxidizer are separately injected into the combustion chamber and the mixing of them are first achieved in the chamber. The diffusion flame has no flammability limit and can burn for any flow rate of fuel and oxidizer. In this regime mixing plays a crucial rule. For a stable combustion process, the mixing should deliver the reactants to the reaction zone very fast. The diffusion controlled flame does not show typical premixed flame characteristics as the reference speed and thickness. The flame can not propagate to the fuel or oxidizer direction as it does not contain the needed reactants. As this work is based on the premixed combustion, the theory and modeling of the diffusion are beyond the scope of the current work and the reader is referred to the specific literature [82, 83, 84, 85, 86, 87, 88].

4.2.1.2 Premixed flames

In this regime the fuel and the oxidizer are mixed before entering into the combustion chamber. The prior mixing causes the premixed flames to have flammability limits. It means that too lean or too rich mixtures can not burn and fail to propagate. Contrary to the diffusion flame, the premixed flame propagates to the fresh gas. The premixed flame can be seen as a discontinuity between fresh and burnt gases, which has a certain thickness δ_l^0 and propagates with a certain speed S_l in direction of fresh gas.

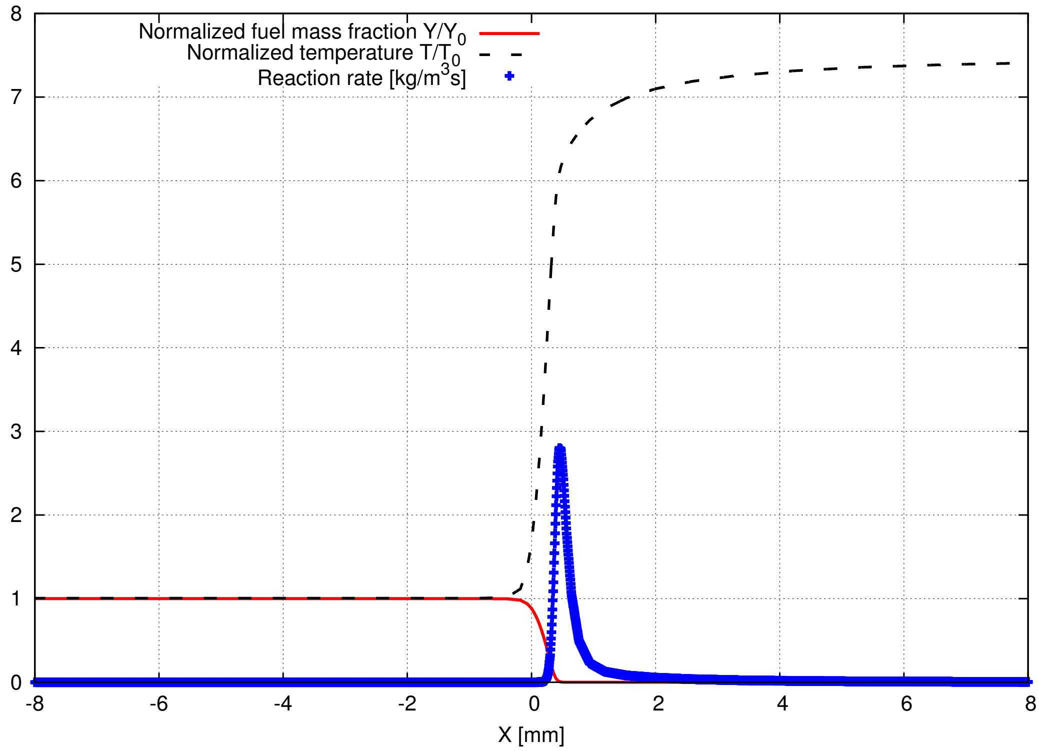

Figure 4.1: Profiles of normalized fuel mass fraction, normalized temperature and the reaction rate for a premixed methane/air flame at stoichiometric condition.

Fig.4.1 shows the profiles of normalized fuel mass fraction, normalized temperature and the reaction rate for a premixed methane-air flame. The one dimensional flame structure is computed using CHEM1D [89] code applying the GRI 3.0 mechanism [90] which contains 325 reactions and 53 species. Three zones can be distinguished, the fresh gas, the reaction zone and the burnt gas state. The temperature increases rapidly in the reaction zone. The burnt gas temperature is more than seven time larger than the fresh gas temperature. The reaction rate is also zero in the fresh gas and burnt gas zones. The reaction rate is a stiff variable of the space. The computed flame has an laminar speed of $S_l = 0.28248$ $[m/s]$ and has a thickness $\delta_l^0 = 0.62504e-03$ $[m]$ calculated based on the maximum temperature gradients.

The conservation equation for a conserved passive scalar (Eq.2.11) has been presented in Chap.2.1. Now we will expand the equation to species mass fraction which also contains the source term. The equation will be simplified and the closure problem will be discussed.

- **Species mass fraction conservation equation**

The species transport equation for $k = 1$ to $N - 1$ is:

$$\frac{\partial \rho Y_k}{\partial t} + \nabla \cdot \left(\rho \left(\mathbf{u} + V_k\right) Y_k\right) = \dot{\omega}_k, \tag{4.1}$$

where the Y_k, ρ and $\mathbf{u}$ are the species mass fraction, density and the velocity vector, respectively. For a laminar flame, the Eq.4.1 is closed for the given models for the reaction rate $\dot{\omega}_k$ and the the diffusion velocities V_k. For the reaction rate $\dot{\omega}_k$, the Arrhenius law should be used. The diffusion velocities V_k in a multispecies gas can be closed using Hirschfelder and Curtiss approximation [91]. In this case the Eq.4.1 reads as:

$$\frac{\partial \rho Y_k}{\partial t} + \nabla \cdot (\rho \mathbf{u} Y_k) = \nabla \cdot \left(\rho D_k \frac{W_k}{W} \nabla X_k\right) + \dot{\omega}_k, \tag{4.2}$$

where $X_k = W_k/W Y_k$ is the species mole fraction and the $W = \sum_{k=1}^{N} X_k W_k$ is the mean molecular weight of the mixture. The D_k is the diffusion coefficient of species k into the mixture and reads as:

$$D_k = \frac{1 - Y_k}{\sum_{j \neq k} X_j / D_{jk}} \tag{4.3}$$

As the Lewis number $Le_k = D_{th}/D_k$, in many flames can be considered as constant through the flame (only small changes in reaction zones), the diffusion coefficients D_k and the heat diffusivity D_{th} can be easily linked together.

The transport mechanism can be also simplified using Fick's law, assuming equality of binary diffusion coefficients [92]:

$$V_k = -D \nabla ln(Y_k) \tag{4.4}$$

The Eq.4.1 will be simplified using Fick's law (Eq.4.4) and unity Lewis number for all species to:

$$\frac{\partial \rho Y_k}{\partial t} + \nabla \cdot (\rho \mathbf{u} Y_k) = \nabla \cdot (\rho D \nabla Y_k) + \dot{\omega}_k \tag{4.5}$$

The current assumptions are used in most flame theories and modelings. Fig.4.2 shows the effect of the different transport mechanisms on the laminar flame speed of methane/air premixed flame at different equivalence ratios. The comparison shows that for lean premixed flames ($\phi < 0.8$) the both transport mechanism show comparative results. For larger equivalence ratios ($\phi < 0.8$), larger deviation is to observer. Both calculations are based on the same chemistry level (GRI 3.0 mechanism) using CHEM1D code.

The analytical and asymptotic solution of the species mass fraction equation for the laminar premixed flame under very restrictive assumptions are available in literature. As this thesis is devoted to turbulent premixed flames, the reader is referred to the special literature [92].

The LES filtered transport equation for a turbulent premixed flame using the simplified assumption for diffusion velocities reads as:

$$\frac{\partial \bar{\rho} \widetilde{Y}_k}{\partial t} + \nabla \cdot \left(\bar{\rho} \widetilde{\mathbf{u}} \widetilde{Y}_k\right) = \nabla \cdot \left[\bar{\rho} \widetilde{D} \nabla \widetilde{Y}_k - \bar{\rho} \left(\widetilde{\mathbf{u} Y_k} - \widetilde{\mathbf{u}} \widetilde{Y}_k\right)\right] + \widetilde{\dot{\omega}}_k, \tag{4.6}$$

where Y_k is the species mass fraction. The $\bar{\cdot}$ and $\tilde{\cdot}$ are filtered and Favre filtered quantities ($\bar{\rho}\widetilde{\phi} = \overline{\rho\phi}$), respectively. Eq.4.6 has two unclosed terms which should be modeled.

- **Unresolved scalar transport**

In the Large Eddy Simulation context, the unresolved species flux, are normally modeled using the gradient assumption as described in Sec.2.7.2.1.

$$\widetilde{\mathbf{u} Y_k} - \widetilde{\mathbf{u}} \widetilde{Y}_k = -\frac{\nu_{sgs}}{Sc_t} \nabla \widetilde{Y}_k, \tag{4.7}$$

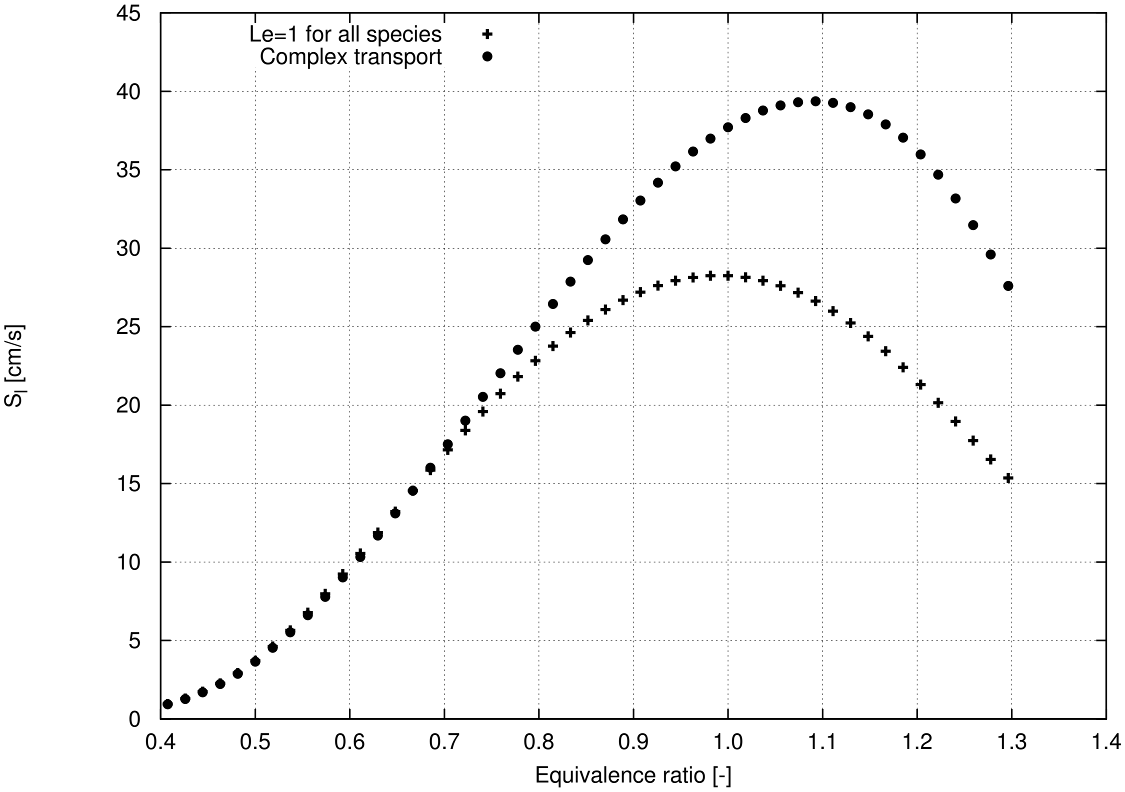

Figure 4.2: The effect of using different transport mechanism on the laminar flame speed for a premixed methane/air flame at different equivalence ratios.

where ν_t is the subgrid scale turbulent viscosity (Eq.2.66) and the Sc_t is the turbulent Schmidt/Prandtl number.

- **Filtered chemical source term**

The Arrhenius law for the fuel mass fraction reaction rate in a simple irreversible reaction reads as:

$$\dot{\omega}_F = -B_1 \rho^2 Y_F Y_O T^{\beta_1} \exp\left(-\frac{T_A}{T}\right), \tag{4.8}$$

where B_1 is the pre-exponential constant, β_1 is the temperature exponent and the T_A is the activation temperature. The usual decomposition method based on the mean and fluctuating quantities is not generally applicable due to the non-linear structure of the Arrhenius law. The alternative is using the Taylor series to expand the mean (filtered) reaction rate. This series development introduces more unclosed high-order terms. This new unclosed terms again need closures using transport equation or algebraic expressions. Therefore the model complexity increase. Taking the only first or second order terms of the series expansion introduces large truncation errors due to highly non-linear nature of the Arrhenius law.

Neglecting the subgrid scale fluctuations, the filtered reaction rate equation reads as:

$$\bar{\dot{\omega}}_F = -B_1 \bar{\rho}^2 \widetilde{Y}_F \widetilde{Y}_O \widetilde{T}^{\beta_1} \exp\left(-\frac{T_A}{\widetilde{T}}\right) \tag{4.9}$$

Such an expression is not useful in most combustion application as the main assumption is that the turbulent subgrid scale time is shorter than the smallest chemical subgrid scale time scale (Da= $\tau_t/\tau_c << 1$).

If we neglect the subgrid scale temperature fluctuations, the filtered reaction rate with second order Taylor series terms can be written as:

$$\bar{\dot{\omega}}_F = -B_1\bar{\rho}^2\widetilde{Y}_F\widetilde{Y}_O\widetilde{T}^{\beta_1}\exp\left(-\frac{T_A}{\widetilde{T}}\right)\left[1+\frac{\widetilde{Y_F Y_O}-\widetilde{Y}_F\widetilde{Y}_O}{\widetilde{Y}_F\widetilde{Y}_O}\right] \tag{4.10}$$

It is also obvious that this expression is also not useful for turbulent flames as the temperature fluctuations are neglected.

Other models based on the scale similarity assumptions also have been proposed [93, 94] in the literature. The model derivation is similar to the procedure used for Reynolds stresses. They are simple and attractive, but the main problem lies in the modeling constants which have been found to be strongly dependent on the mesh size and Dämkohler number. This disadvantage makes the models inappropriate for most combustion application in which the length scale effects should be considered.

As discussed above, the modeling based on the Taylor series development of the Arrhenius law are not applicable to the most turbulent flows. The scale similarity models are also not useful as the similarity constant has strong length scale dependency. In the upcoming section we will review the models which are mostly based on the physical analysis of the turbulent premixed flows and are widely used in the LES context.

4.2.2 G-equation approach

In the G-equation approach the flame front is viewed as infinitely thin and described as a propagating surface tracked using kinematic equation of the field variable G [7]. The value of G is normally set to be zero at the flame front, is smaller than zero in the unburned mixture and has positive values in the burned gases. The resolved flame brush is convected by the displacement speed $\overline{S}_T$.

$$\frac{\partial\bar{\rho}\widetilde{G}}{\partial t}+\frac{\partial\bar{\rho}\widetilde{u}_i\widetilde{G}}{\partial x_i}=\rho_u\cdot\overline{S}_T\cdot|\nabla\widetilde{G}| \tag{4.11}$$

The turbulent flame speed $\overline{S}_T$ is modeled generally as:

$$\frac{\overline{S}_T}{S_l}=1+\alpha\left(\frac{u'}{S_l}\right)^n, \tag{4.12}$$

where u' is the subgrid scale turbulent fluctuation normally extracted from the resolved shear stresses. The α and n are constants which can also be calculated dynamically [95].

4.2.3 Thickened Flame model for LES (TFLES)

A well-known approach to propagate a premixed flame on the LES mesh is to modify thermal diffusivity and pre-exponential constants and is originally proposed by Butler and O'Rouke [96]. This approach leads to a thickened flame front which is then resolvable on LES mesh grid for sufficiently large thickening factor. The expressions. 4.13, 4.14 show that by increasing the thermal diffusivity D_{th} with a factor F while decreasing the exponential factor B_1 in the Arrhenius law (Eq.4.8) with the same factor F, the flame speed S_l remains constant while the flame thickness is increased by F [92].

$$S_l \propto \sqrt{D_{th} B} \tag{4.13}$$

$$\delta_l^0 \propto \sqrt{\frac{D_{th}}{B}} \tag{4.14}$$

Hence thickening the flame thickness reduces the Damköhler number, the turbulence and chemistry interaction will be modified consequently [4]. To compensate this disadvantage the laminar flame speed will be modified by an efficiency function E_Δ which depends on velocity and length scale ratios extracted from resolved velocity field. These subgrid scale models can be based on similarity assumption [11] or the unresolved flame surface density in terms of a general power-law expression involving an inner cutoff scale [12]. considering an equilibrium assumption of flame-surface production and destruction and turbulence leads to a constant value, typically 0.5 for the power-law exponent β.
The set of equations for large eddy simulation of turbulent premixed flames using non-dynamic artificially thickened flame model coupled with tabulated chemistry and assumption of equal thermal diffusivity for all species reads as [15] :
Equation of state for mixture fraction Z is:

$$\frac{\partial \bar{\rho}\widetilde{Z}}{\partial t} + \nabla \cdot \left(\bar{\rho}\widetilde{\mathbf{u}}\widetilde{Z}\right) = \nabla \cdot \left(\bar{\rho}\left(\widetilde{D} + \widetilde{D}^t\right)\nabla \widetilde{Z}\right), \tag{4.15}$$

where the ρ, D, $\mathbf{u}$ are density, diffusion coefficient and the velocity vector, respectively. The $\bar{\cdot}$ and $\tilde{\cdot}$ are filtered and Favre filtered quantities ($\bar{\rho}\widetilde{\phi} = \overline{\rho\phi}$), respectively.
The LES filtered progress variable equation is:

$$\begin{aligned} \frac{\partial \bar{\rho}\widetilde{Y}_c}{\partial t} + \nabla \cdot \left(\bar{\rho}\widetilde{\mathbf{u}}\widetilde{Y}_c\right) &= S\nabla \cdot \left(F E_\Delta \bar{\rho}\widetilde{D}\nabla \widetilde{Y}_c\right) \\ &+ (1-S)\,\nabla \cdot \left(\bar{\rho}\left(\widetilde{D} + \widetilde{D}^t\right)\nabla \widetilde{Y}_c\right) + \frac{E_\Delta}{F}\widetilde{\dot{\omega}}_c, \end{aligned} \tag{4.16}$$

where Y_c is the progress variable mass fraction and the F is the thickening factor. The $\widetilde{\dot{\omega}}_c$ is the progress variable source term which is extracted here directly from a two dimensional chemical look-up table based on the trajectories of progress variable and mixture fraction $\phi = (Y_c, Z)$, using FGM technique [68].

- The linear efficiency model is [11]:

$$E_\Delta = \frac{\Xi(\delta_l^0)}{\Xi(\delta_l^1)} = \frac{1 + \alpha\Gamma\left(\Delta_e/\delta_l^0, u'_{\Delta_e}/S_l\right) u'_{\Delta_e}/S_l}{1 + \alpha\Gamma\left(\Delta_e/\delta_l^1, u'_{\Delta_e}/S_l\right) u'_{\Delta_e}/S_l} \tag{4.17}$$

$$\Gamma\left(\Delta_e/\delta_l^0, u'_{\Delta_e}/S_l\right) = 0.75 \exp\left[-1.2/\left(u'_{\Delta_e}/S_l\right)^{0.3}\right]\left(\Delta_e/\delta_l^{0,1}\right)^{2/3} \tag{4.18}$$

in which the δ_l^1 is the filtered flame thickness and the parameter α is estimated as below depending on the turbulent Reynolds number:

$$\alpha = \beta \frac{2\ln(2)}{3C_{ms}\left(Re_t^{1/2} - 1\right)}, \; Re_t = \frac{u' l_t}{\nu} \tag{4.19}$$

The β is a model constant which is near to unity and the C_{ms} is 0.28.

- The power-law wrinkling model [12] reads as:

$$E_\Delta = \left(1 + \min\left[\max\left(\frac{\Delta}{\delta_l^0} - 1, 0\right), \Gamma \frac{u'_\Delta}{S_l}\right]\right)^\beta, \tag{4.20}$$

where $\Gamma\left(\Delta/\delta_l^0, u'_\Delta/S_l, Re_\Delta\right)$ is an efficiency function describing the net strain effect of subfilter turbulent scales.

$$\Gamma = \left[((f_u^{-a} + f_\Delta^{-a})^{-1/a})^{-b} + f_{Re}^{-b}\right]^{-1/b} \tag{4.21}$$

$$f_u = 4\left(\frac{27C_k}{110}\right)^{1/2}\left(\frac{18C_k}{55}\right)\left(\frac{u'_\Delta}{S_l}\right)^2 \tag{4.22}$$

$$f_\Delta = \left[\frac{27C_k\pi^{4/3}}{110}\left(\left(\frac{\Delta}{\delta_l^0}\right)^{4/3} - 1\right)\right]^{1/2} \tag{4.23}$$

$$f_{Re} = \left[\frac{9}{55} exp\left(\frac{-3}{2} C_k \pi^{4/3} Re_\Delta^{-1}\right)\right]^{1/2} Re_\Delta^{1/2}, \tag{4.24}$$

$$a = 0.6 + 0.2 exp\left[-0.1\left(u'/S_l\right)\right] - 0.2 exp\left[-0.01\left(\Delta/\delta_l^0\right)\right], \tag{4.25}$$

where

$$Re_\Delta = 4\left(\Delta/\delta_l^0\right)\left(u'_\Delta/S_l\right), \Delta = F\delta_l^0 \tag{4.26}$$

are respectively subgrid turbulent Reynolds number and the filter size. The Kolmogorov constant is $C_k = 1.5$ and $\beta = 0.5$ as a model constant for non-dynamic model.

The u'_Δ is the subgrid scale velocity fluctuation at test filter scale $\Delta = F\delta_l^0$, estimated from resolved velocity field [11]. The term $\Delta/n_x\Delta_x$ is a correction to the original expression to omit the thermal expansion contribution which is not related to the turbulence [22].

$$u'_\Delta = c_2 \Delta_x^3 \mid \nabla^2 \times (\nabla \times \tilde{\mathbf{u}}) \mid \left(\frac{\Delta}{n_x \Delta_x}\right)^{1/3} \tag{4.27}$$

using a flame sensor S, ensures that thickening does not affect the regions of pure mixing. The sensor used in this work is based on the progress variable source term and reads as:

$$S = \frac{\max\left(\tanh\left(100\frac{\dot\omega_c(\widetilde{\phi})}{\dot\omega_{c,max}(\widetilde{Z})} - 0.25\right); 0\right)}{0.75}, \tag{4.28}$$

here $\phi = (Y_c, Z)$ and the $\dot\omega_{c,max}$ is the maximum progress variable source term of the current mixture fraction. The sensor should be zero in the regions of pure mixing. For a methane-air mixture the flame sensor is set to zero in the lower flammability limit $Z[-] < 0.02$ [23].

4.2.4 Flame Surface Density (FSD) approach

The Flame Surface Density (FSD) approach is based on the filtering of the progress variable transport equations using a filter larger than the mesh size. The LES filtered transport equation of progress variable is written as:

$$\frac{\partial \bar{\rho}\widetilde{Y}_c}{\partial t} + \nabla \cdot \left(\bar{\rho}\tilde{\mathbf{u}}\widetilde{Y}_c\right) + \nabla \cdot \left[\bar{\rho}\left(\widetilde{\mathbf{u}Y_c} - \tilde{\mathbf{u}}\widetilde{Y}_c\right)\right] = \overline{\nabla \cdot (\rho D \nabla Y_c)} + \bar{\dot{\omega}}_c = \overline{\rho S_d |\nabla Y_c|} \tag{4.29}$$

The filtered equation has unclosed terms. The first one is subgrid scale scalar flux, the second is filtered molecular term and the third one is the filtered chemical source term. The basic idea is that the product of flame surface and the flame propagation speed will deliver the consumption rate of the unburned mixture. Therefore the filtered molecular diffusion term and chemical source term can be considered as propagation (flame front displacement) and modeled as a single term, namely the subgrid scale flame surface density (flame surface per unit volume).

The term $\overline{\rho S_d |\nabla Y_c|}$ in RHS of Eq.4.29 corresponds to the flame front displacement and can be modeled as [10]:

$$\overline{\rho S_d |\nabla Y_c|} \approx \rho_u S_l \Sigma = \rho_u S_l \Xi |\nabla \overline{Y}_c| \tag{4.30}$$

In the expression 4.30, the ρ_u and S_l are the density of unburned mixture and laminar flame speed respectively. The Σ is the subgrid scale flame surface density per unit volume and Ξ shows the subgrid scale flame wrinkling factor which are to be modeled. These terms can be modeled in different approaches. One can solve an extra transport equation [97, 10, 98, 16] or a modeled transport equation for the perturbed laminar flame speed [17]. The similarity models [99] or algebraic expressions with assumption of equality for production and dissipation in the transport equations, are also exploited for description of the flame surface density expression (4.30). The FSD model is also extended for some specific combustion processes like spark-ignition [100].

The other term that should be modeled is the subgrid scale fluxes. The most used model is the gradient transport models. The occurring problem is the counter gradient diffusion caused by heat release in premixed combustion specially for low intensity turbulence. The addressed problem leads in failure using gradient transport models [101]. To tackle this problem, different subgrid scale modeling are proposed for Large Eddy Simulation [98, 102].

4.2.5 Filtered Tabulated Chemistry for LES (F-TACLES)

As explained in FSD models, the expression 4.30 should be modeled. One interesting proposed approach is to filter the one-dimensional laminar flamelets to extract the term $\rho_u S_l |\nabla \overline{Y}_c|$ and tabulate it [103]. The same idea has been used for development of a new combustion model. The pre-computed laminar one-dimensional flamelet using complex chemistry will be filtered and consequently tabulated using FPI or FGM techniques. The sub gird scale equivalence ratio will be also neglected due to the similarity assumption of planar filtered flame for fixed equivalence ratios and the three-dimensional flames. The F-TACLES model [13, 104, 105] first was developed for the premixed flames but it is also extended to partial premixed regimes [14] and non-premixed regime [106] as well. The F-TACLES approach assures the correct propagating flame speed prediction and simultaneously improve the predictions using the resolved and modeled contributions. The model is tested and validated through simulation of various configurations [13, 23, 107, 108].

In addition to the continuity and Navier-Stokes equations, the large eddy simulation of turbulent premixed flames using F-TACLES model includes: The mixture fraction balance equation Z:

$$\frac{\partial \bar{\rho}\widetilde{Z}}{\partial t} + \nabla \cdot \left(\bar{\rho}\widetilde{\mathbf{u}}\widetilde{Z}\right) = \nabla \cdot \left(\bar{\rho}\left(\widetilde{D} + \widetilde{D}^t\right)\nabla \widetilde{Z}\right), \tag{4.31}$$

where the ρ, D, u are the density, the diffusion coefficient and the velocity vector, respectively. The quantities noted as $\bar{\cdot}$ and $\widetilde{\cdot}$ are filtered and Favre filtered quantities ($\bar{\rho}\widetilde{\phi} = \overline{\rho\phi}$), respectively. The progress variable transport equation reads as:

$$\begin{aligned} \frac{\partial \bar{\rho}\widetilde{Y}_c}{\partial t} + \nabla \cdot \left(\bar{\rho}\widetilde{\mathbf{u}}\widetilde{Y}_c\right) &= S\nabla \cdot \left(E_\Delta \alpha \bar{\rho}\widetilde{D}\nabla \widetilde{Y}_c\right) \\ + \left(1 - S\right)\nabla \cdot \left(\bar{\rho}\left(\widetilde{D} + \widetilde{D}^t\right)\nabla \widetilde{Y}_c\right) &+ E_\Delta \bar{\rho}\Sigma_c, \end{aligned} \tag{4.32}$$

where Y_c is the progress variable mass fraction.

$$\begin{aligned} \bar{\rho}\Sigma_c &= \Omega_c + \widetilde{\rho\dot{\omega}_c} \\ \Omega_c &= -\rho S_l \left[\frac{\partial \overline{Y_c^*}}{\partial x^*} - \frac{\partial \widetilde{Y_c^*}}{\partial x^*}\right], \end{aligned} \tag{4.33}$$

where $\bar{\rho}\Sigma_c = \Omega_c + \widetilde{\rho\dot{\omega}_c}$ is the sum of progress variable chemical source term and a closure term (unresolved transport due to thermal expansion). The * indicates 1-dimensional reference non-filtered flamelets computed from complex chemistry.

$$\alpha_c = \frac{\overline{\rho^* D \frac{\partial Y_c^*}{\partial x^*}}}{\overline{\rho \widetilde{D} \frac{\partial \widetilde{Y_c^*}}{\partial x^*}}} \tag{4.34}$$

The α is a correction factor for filtered molecular diffusivity. These extra terms are a priori stored beside density and dynamic viscosity in two-dimensional chemical look-up table based on the trajectories of progress variable and mixture fraction and the filter size $\phi = (\widetilde{Y}_c, \widetilde{Z}, \Delta)$, using FGM technique framework.

The turbulence and combustion interaction is also modeled in F-TACLES model like the TFLES model using the wrinkling factor E_Δ. Both linear model [11] and power law wrinkling model [12, 19] are coupled and tested for F-TACLES approach [13, 23, 109]

4.2.6 Dynamic formulation of the Artificially Thickened Flame model coupled with tabulated chemistry (DATF)

As mentioned before, the equilibrium assumption between flame and turbulence leads to constant values for the exponent in power-law wrinkling model [12]. As this equilibrium is not generally reached in early flame development, assuming a constant model parameter leads to a wrong turbulent burning velocity S_T. In this work the power-law wrinkling exponent is calculated on the fly using a Germano-like procedure from filtered resolved flow fields as suggested by [19, 21]. The parameter β in the power-law wrinkling model is determined from comparing the reaction rate calculated by LES filter Δ and the reaction rate calculated from test filtered $\widehat{\Delta}$ parameters both averaged over a given domain $< \cdot >$. The LES filtered progress variable source term $\bar{\dot{\omega}}_c$ in Eq.4.16 is:

$$\bar{\dot{\omega}}_c = \frac{E_\Delta}{\Delta}\delta_l^0 \dot{\omega}_c(\widetilde{\phi}) = \frac{E_\Delta}{\Delta} W_{\Delta,c}(\widetilde{\phi}) \tag{4.35}$$

Using a test filter $\widehat{\Delta} = \gamma\Delta, \gamma > 1$, the test filtered reaction rate reads as:

$$\widehat{\bar{\dot{\omega}}_c} = \widehat{\frac{E_\Delta}{\Delta} W_{\Delta,c}(\widetilde{\phi})} \tag{4.36}$$

Applying Germano-like procedure and equating the test filtered reaction rate and the source term from test filtered variables over a given domain gives:

$$\left\langle \widehat{\frac{E_\Delta}{\Delta} W_{\Delta,c}(\widetilde{\phi})} \right\rangle = \left\langle \frac{E_{\widehat{\Delta}}}{\widehat{\Delta}} W_{\widehat{\Delta},c}(\widehat{\widetilde{\phi}}) \right\rangle = \left\langle \frac{E_{\gamma\Delta}}{\gamma\Delta} W_{\gamma\Delta,c}(\widehat{\widetilde{\phi}}) \right\rangle \tag{4.37}$$

The parameter β can be obtained as suggested in [19]:

$$\beta = \frac{\log\left(\gamma < \widehat{W_{\Delta,c}(\widetilde{\phi})} > / < W_{\gamma\Delta,c}(\widehat{\widetilde{\phi}}) >\right)}{\log\left(\frac{1+\min\left(\gamma\Delta/\delta_l^0 - 1,\ \Gamma_{\gamma\Delta} < u'_{\gamma\Delta} > /S_l\right)}{1+\min\left(\Delta/\delta_l^0 - 1,\ \Gamma_{\Delta} < u'_{\Delta} > /S_l\right)}\right)} \tag{4.38}$$

The practical implementation of Eq.4.38 will encounter some difficulties as explained in [21]. The main one is definition of modeled turbulence fluctuation Eq.(4.27) at both filter and test filter levels. Wang et al [21] suggested a simplification of the Eq.4.38 in the limiting case of large turbulence intensities $u' >> S_l$ in which the wrinkling factor reduces to :

$$\begin{aligned} \lim_{u'_\Delta \to \infty} E_\Delta &= \left(\frac{\Delta}{\delta_l^0}\right)^\beta \\ \lim_{u'_{\gamma\Delta} \to \infty} E_{\gamma\Delta} &= \left(\frac{\gamma\Delta}{\delta_l^0}\right)^\beta \end{aligned} \tag{4.39}$$

Using this expression the Eq.4.38 will be simplified to:

$$\beta = 1 + \frac{\log(< \widehat{W_{\Delta,c}(\widetilde{\phi})} > / < W_{\gamma\Delta,c}(\widehat{\widetilde{\phi}}) >)}{\log(\gamma)} \tag{4.40}$$

The Eq.4.40 is practically easier to implement. The averaging method <> also can be conducted in different ways. Assume a uniform β which is only subject of the temporal changes, one can easily average the power-law value over whole domain. More complex methods can also be conducted in which the β is assumed to be also spatial dependent. In this way the β will be calculated based on the spatial direction over neighbor control volumes [23, 24].

4.2.6.1 Test filtering

The test filtering can be conducted using the direct computation of the filter kernel, although is CPU costly. The alternative approach proposed by [110], is based on the truncation of the moments of the filter. In this approach the Gaussian filter will be approximated by using a Taylor expansion before performing the convolution operator. The convolution operator with the Gaussian filter G in one-dimensional reads as:

$$\begin{aligned}
\overline{\Phi}(x) &= \int_{-\infty}^{+\infty} G(y-x)\phi(y)dy \\
&= \int_{-\infty}^{+\infty} G(y-x)\sum_{n=0}^{n=\infty}\frac{\phi^{(n)}(x)}{n!}(y-x)^n dy \\
&= \sum_{n=0}^{n=\infty}\frac{\phi^{(n)}(x)}{n!}\int_{-\infty}^{+\infty} G(y-x)(y-x)^n dy \\
&= \sum_{n=0}^{n=\infty}\frac{\phi^{(n)}(x)}{n!}\underbrace{\int_{-\infty}^{+\infty} G(z)(z)^n dz}_{Pn} \qquad (4.41)
\end{aligned}$$

Substituting $z = y - x$ and using expression of

$$G(z) = \left(\frac{6}{\pi\Delta^2}\right)^{1/2} \exp\left[-\frac{6}{(\gamma\Delta)^2}(z^2)\right], \qquad (4.42)$$

gives:

$$\begin{aligned}
P0 &= 1 \\
P1 &= 0 \qquad (4.43) \\
P2 &= \frac{\Delta^2}{12}
\end{aligned}$$

Writing the three-dimensional as:

$$\begin{aligned}
\overline{\Phi}(x,y,z) &= \int_{-\infty}^{+\infty} G(x-x',y-y',z-z')\phi(x',y',z')dx'dy'dz' \qquad (4.44) \\
&= \int\int\int_{-\infty}^{+\infty} G(X,Y,Z)\sum_{n1,n2,n3=0}^{\infty}\frac{X^{n1}Y^{n2}Z^{n3}}{n1!n2!n3!}\frac{\partial^{n1+n2+n3}\phi(x,y,z)}{\partial x^{n1}\partial y^{n2}\partial z^{n3}}dXdYdZ \\
&= \sum_{n1,n2,n3=0}^{\infty}\frac{1}{n1!n2!n3!}\frac{\partial^{n1+n2+n3}\phi(x,y,z)}{\partial x^{n1}\partial y^{n2}\partial z^{n3}}\cdot Pn1n2n3
\end{aligned}$$

with

$$\begin{aligned} Pn1n2n3 &= \int\int\int_{-\infty}^{+\infty} G(X,Y,Z)X^{n1}Y^{n2}Z^{n3}dXdYdZ && (4.45) \\ &= \int\int\int_{-\infty}^{+\infty} G(X)X^{n1}G(Y)Y^{n2}G(Z)Z^{n3}dXdYdZ \\ &= Pn1Pn2Pn3 && (4.46) \end{aligned}$$

Retaining only the second order:

$$\overline{\Phi}(x,y,z) = \Phi(x,y,z) + \frac{\Delta^2}{24}\frac{\partial^2\Phi}{\partial x_i^2} \quad (4.47)$$

4.2.6.2 Numerical methods

An implicit second-order scheme is used and validated for given 1D analytical functions and simple 2D test cases. The computation of this diffusion-like expression (Eq. 4.47) shows 20 times speed up in compare to using direct filter kernel on multidimensional cases [110, 24, 23].

The finite volume formulation writes:

$$\frac{1}{V_j}\int_{\Omega_j}\overline{\Phi}(x,y,z)dV = \frac{1}{V_j}\int_{\Omega_j}\Phi(x,y,z)dV + \underbrace{\frac{1}{V_j}\int_{\Omega_j}\frac{\Delta^2}{24}\frac{\partial^2\Phi}{\partial x_i^2}(x_i)dV}_{A} \quad (4.48)$$

where:

$$\begin{aligned} A &= \frac{1}{V_j}\int_{\Omega_j}\frac{\Delta^2}{24}\frac{\partial^2\Phi}{\partial x_i^2}(x_i)dV \\ &= \frac{1}{V_j}\int_{\Omega_j}\frac{\Delta^2}{24}\frac{\partial}{\partial x_i}\frac{\partial\Phi}{\partial x_i}(x_i)dV \\ &= \frac{1}{V_j}\int_{S_{\Omega_j}}\frac{\Delta^2}{24}\frac{\partial\Phi(x_i)}{\partial x_i}n_i dS \\ &\approx \frac{1}{V_j}\frac{\Delta^2}{24}\sum_{S_k\in S_{\Omega_j},k=1,6}\left(\frac{\partial\Phi(x_i)}{\partial x}n_{x,k} + \frac{\partial\Phi(x_i)}{\partial y}n_{y,k} + \frac{\partial\Phi(x_i)}{\partial z}n_{z,k}\right)S_k && (4.49) \end{aligned}$$

where S_k is the surface associated with face $k \in [E,W,N,S,T,B]$ (*i.e.* the est, west, ... sides). Using MLU-procedure [53] implemented in FASTEST code for calculation of diffusion operator:

$$A \approx \frac{1}{V_j}\frac{\Delta^2}{24}\sum_{S_k\in S_{\Omega_j},k=1,6}\left\{\left(\frac{\Psi^{l,x}_{S_k}}{J_{S_k}}n_{x,k} + \frac{\Psi^{l,x}_{S_k}}{J_{S_k}}n_{y,k} + \frac{\Psi^{l,x}_{S_k}}{J_{S_k}}n_{z,k}\right)\Phi^l_{S_k}\right\}S_k \quad (4.50)$$

where $l \in [1,3]$. J_{S_k} is the control volume associated with the face S_k and, for face est, it is defined by:

$$J_{S_E} = (x_{E,i} - x_{P,i})\Psi^{1,x}_{S_E} \quad (4.51)$$

with

$$\begin{aligned}
\Psi^{1,x}_{S_E} &= \epsilon_{ikl}[(x_{N,k} - x_{S,k} + x_{NE,k} - x_{SE,k})(x_{T,l} - x_{B,l} + x_{TE,l} - x_{BE,l})] && (4.52)\\
\Psi^{2,x}_{S_E} &= \epsilon_{ikl}[(x_{T,k} - x_{B,k} + x_{TE,k} - x_{BE,k})(x_{E,l} - x_{P,l})] && (4.53)\\
\Psi^{3,x}_{S_E} &= \epsilon_{ikl}[(x_{E,k} - x_{P,k})(x_{N,l} - x_{S,l} + x_{NE,l} - x_{SE,l})] && (4.54)\\
\Phi^{1}_{S_E} &= \Phi_E - \Phi_P && (4.55)\\
\Phi^{2}_{S_E} &= \Phi_N - \Phi_S + \Phi_{NE} - \Phi_{SE} && (4.56)\\
\Phi^{3}_{S_E} &= \Phi_T - \Phi_B + \Phi_{TE} - \Phi_{BE} && (4.57)
\end{aligned}$$

where $\Phi^1_{S_k}$ is the orthogonal contribution, and $\Phi^2_{S_k}$ and $\Phi^3_{S_k}$ counts for non-orthogonal terms. On a cartesian grid, the two last expressions may be omitted and only $\Phi^1_{S_k}$ remains.

Schmitt has shown [111] different numerical procedures to solve these equations. These methods are solving direct, explicitly and implicitly using the incomplete LU decomposition following FASTEST code. Each of this numerical methods have their ad and disadvantages. For example, solving explicitly is easy to implement and leads to the second order approximation but needs a large number of sub-steps to satisfy the pseudo-Fourier stability conditions.

Conducting the numerical simulation implicitly using the incomplete LU decomposition delivers first order upwind which is always stable and monotonic but the with limiting first order approximation. The Euler scheme increases the order by using Gauss formalism which needs few mandatory additional sub steps to suppress unphysical oscillations. Using implicit approach, the orthogonal part will be solved implicitly while he non-orthogonal contribution is explicitly solved. The current approach leads to numerical oscillations with strongly stretched grids.

The one-dimensional and two dimensional test cases are carried in the [111] for the analytical solutions, The three-dimensional cases are also conducted using F-TACLES combustion model [110, 24, 23]. The same numerical method is used in the current work to implement the dynamic power-law wrinkling factor in the ATF combustion model context as described in 4.2.6. The three-dimensional test cases will be conduct in the current work.

4.2.6.3 Practical procedure

The practical procedure to compute the power-law exponent in artificially thickened flame model coupled with tabulated chemistry is first to define the test filter as $\widehat{\Delta} = \gamma F \delta_l^0$. The next step is to test filter the density $\widehat{\bar{\rho}}$, Favre test filter the mixture fraction $\widehat{Y}_c = \overbrace{\bar{\rho}\widetilde{Y}_c} / \widehat{\bar{\rho}}$ and progress variable $\widehat{Z} = \overbrace{\bar{\rho}\widetilde{Z}} / \widehat{\bar{\rho}}$. The resolved progress variable source term also should be test filtered $\overbrace{W_{\Delta,c}(\widetilde{\phi})}$. The progress variable from test filtered mixture fraction and progress variable will be extracted directly from the chemical look-up table $W_{\gamma\Delta,c}(\widehat{\widetilde{\phi}})$. The test filtered progress variable source term and the progress variable source term extracted from look-up table will be averaged on a given domain $< \overbrace{W_{\Delta,c}(\widetilde{\phi})} >$ and $< W_{\gamma\Delta,c}(\ widehat\widetilde{\phi}) >$, respectively. The averaging can be either global over whole domain or local. The last step is to calculate the exponent from the Eq.4.40 and update it in appropriate sequences.

Chapter 5

Application: Matrix burner

5.1 Experimental and numerical setup

5.1.0.4 Experimental setup

The matrix burner (turbulent bunsen type) was developed and experimentally investigated at Karlsruhe Institute of Technology (KIT) [112, 113]. The objective was to constitute turbulent flames with gas turbines characteristics, i.e., high turbulence intensity and high energy density. The model burner is equipped with a square matrix turbulence generator consisting of 32 boreholes and swirl sheets that render opposite swirl direction in each borehole pair respectively. Fig.5.1 shows the experimental set-up of the model burner which consist of the turbulence generator, the burner nozzle and the stabilization device.

The burner jet flow is homogenous and has a well-defined mean velocity without integral swirl and has high volumetric heat release rates. The flame is stabilized upstream of the burner orifice at the jet rim. In the current work, a methane/air mixture with an air to fuel equivalence ratio of $\lambda = 1.75$ (lean premixed) and a thermal load of $P_{th} = 275.6kW$ is considered which is preheated to the temperature of $T_u = 673K$. The Re based on the nozzle diameter ($D = 0.15m$) and bulk velocity ($U_{bulk} = 23.5m$) is $Re \approx 55.000$ (See Tab.5.1).

D_{nozzle}	$d_{borehole}$	Re_D	Ma_u	T_u	T_∞	λ	P
150 mm	20 mm	55000	0.046	673 K	298 K	1.75	275 kW

Table 5.1: Re_D Reynolds number, Ma_u Mach number, T_u and T_∞ temperature of unburnt mixture and ambient air, λ Air to fuel ratio and P indicates the thermal power.

5.1.0.5 Numerical setup

The computational domain consists of a part of the nozzle ($length = 0.1$ $[m]$) and a cylindrical region ($length \times diameter = L \times D = 2m \times 1.6m$) downstream of the burner. In this study two grid level are used for simulation of the matrix burner (See Fig. 5.2). The coarse grid has a size of approximately 4.5 million cells which is systematically refined with a grid size of $\Delta_{min} = 2.0$ $[mm]$ in the region of interest. The finer grid has a size of approximately 11 million cells with a grid size of $\Delta_{min} = 1.0$ $[mm]$ in the region of interest. The grid form is held cubic in the nozzle up and downstream.

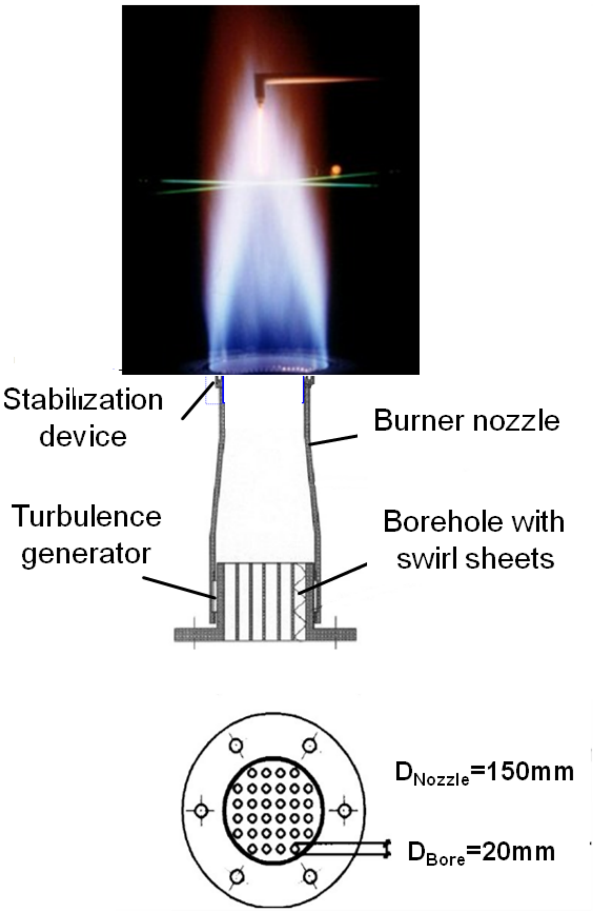

Figure 5.1: Matrix burner experimental setup.

The numerical settings for the inlet boundary conditions are listed in Tab.5.2. The turbulence intensity T_i and the integral length scale L_t are used by the inflow generator [57] together with the velocity profile $U_{inlet}(r)$ corresponding to the boundary condition of the experimental configuration. The flame is numerically stabilized using burnt methane gas as pilot. The coflow considered as air which is also tabulated in look up tables.

y_{CH_4}	y_{O_2}	y_{N_2}	T_u	U_0	D	$U_{inlet}(r)$	T_i	L_t
0.0322	0.2254	0.7424	$673K$	$23.5m/s$	$0.15m$	$U_0 \cdot (1-(2r/D_0)^{16})$	13%	$8mm$

Table 5.2: Inlet boundary conditions for the numerical investigation of matrix burner.

Fig.[5.3] shows the premixed combustion regime in the context of Large Eddy Simulation proposed by Pitsch et al [6]. This premixed regime diagram is constructed based on the same physical information as the Peters's diagram including new regimes coming from the numeric and LES filter width changes. The premixed diagram is illustrated based on the Karlovitz number for the horizontal axis and the filter width variation as vertical axis. The Karlovitz number is defined as ratio of the time scales of the laminar flame and the Kolmogorov eddies and therefore is independent of filter width. For the LES of the premixed combustion the Damköhler number and the turbulent Reynolds number can be defined also based on the subgrid velocity fluctuation u'_Δ and the filter width Δ. The

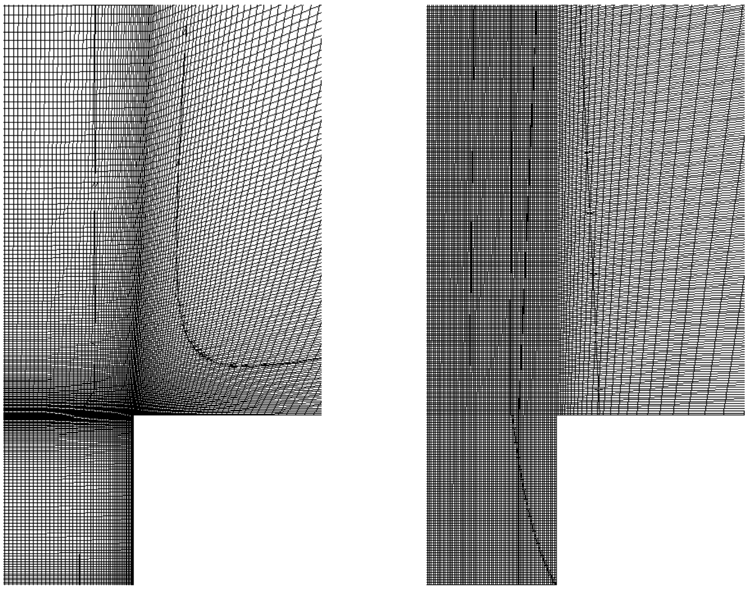

Figure 5.2: Matrix burner investigated mesh grid, Left: coarse, right: fine.

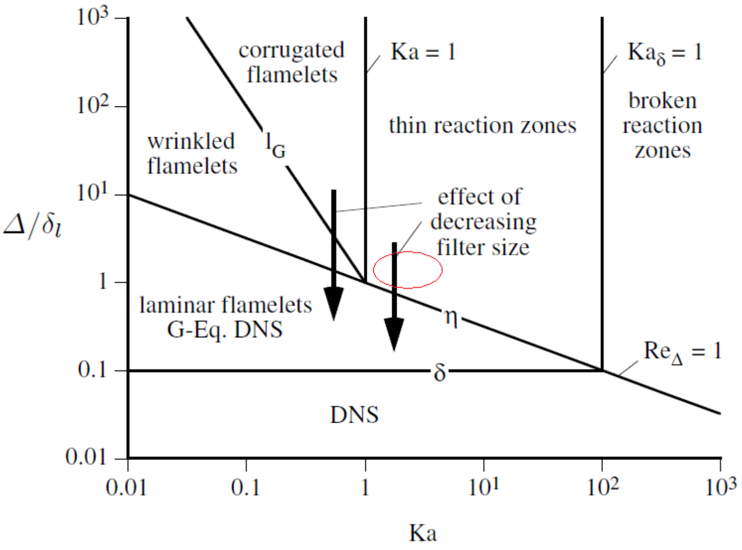

Figure 5.3: Regime diagram for the LES of turbulent premixed combustion [6]. The red area indicates the classification for the investigated flame.

Karlovitz number and the turbulent Damköhler are here defined as:

$$Ka^2 = \left(\frac{u'_\Delta}{S_l}\right)^3 \frac{\delta_l^0}{\Delta} \tag{5.1}$$

$$Da_\Delta = Ka^{-2} \left(\frac{u'_\Delta}{S_l}\right)^2 \tag{5.2}$$

The calculated value of Karlovitz number (Eq.(5.1)) for the current configuration is Ka=3-8, based on the subgrid velocity fluctuation $u'_\Delta \approx 2-4$ $[m/s]$ (See Fig.5.47), laminar flame thickness $\delta_l^0 = 0.4$ $[mm]$ (See Fig.5.4), laminar flame speed $S_l = 0.7$ $[m/s]$ and LES grid width $\Delta_{min} = 1$ $[mm]$ for the fine mesh. The Karlovitz number is independent of LES grid width as the amplitude of subgrid velocity fluctuation u'_Δ varies also depending on the LES grid size. According to these values the investigated configuration is located in the thin reaction zones regime. The diagram shows that in this regime zone, the coarsening of the mesh does not leads to combustion regime change.

The diverse numerically conducted simulations for the matrix burner configuration are gathered in Tab.(5.3). The matrix burner is numerically investigated using two grid levels. The combustion models ATF (Artificially Thickened Flame) [11, 15] and F-TACLES (Filtered TAbulated Chemistry for LES) [14, 23], are used in this investigation. The dynamic version of the power-law wrinkling model [19] is coupled with the ATF combustion model. In the cases using power-law wrinkling model, the beta power is calculated using local and global averaging approaches.

The simulations are conducted using both combustion models coupled with the dynamic [19] following the dynamic procedure proposed in [21] and the non-dynamic [12] forms of the power-law wrinkling model and the linear wrinkling model [11]. The simulation results are then compared with the experiment to investigate the predictability of the combustion and wrinkling modeling on this flame type.

The CHEM1D code [89] is used to calculate the internal flame structure applying the GRI 3.0 mechanism [90] which contains 53 species and 325 reactions. The laminar flame speed of the investigated configuration is depicted in Fig.5.4 against the fuel mixture fraction. The laminar flame speed of methane/air mixture under normal conditions is also illustrated in Fig.5.4. The comparison shows higher laminar flame speed for the investigated configuration for the same mixture fraction corresponding to non-preheated mixture.

The chemistry look up table is constructed using FGM technique. It consist of one progress variable (CO_2 mass fraction) and one mixture fraction variable. All other dependent variables are tabulated based on these two variables.

Combustion model	**Wrinkling model**	**Numerical model**	**β power**	**Grid**	**Case**
ATF[a]	Power law	NA[b]	Fixed (0.5)	Coarse	1
	Power law	NA	Fixed (0.5)	Fine	2
	Power law	Gaussian	Dyn (global)	Coarse	3
	Power law	Gaussian	Dyn (global)	Fine	4[c]
	Power law	Gaussian	Dyn (local)	Fine	5
	Linear	NA	NA	Fine	6
F-TACLES[d]	Power law	NA	Fixed (0.5, 03)	Coarse	7
	Power law	Gaussian	Dyn (global)	Coarse	8
	Power law	Gaussian	Dyn (global)	Fine	9

[a] Artificially Thickened Flame
[b] Not Applicable
[c] This case has 3 subcases (See Tab.5.4)
[d] Filtered Tabulated Chemistry For LES

Table 5.3: The investigated test cases for the matrix burner configuration.

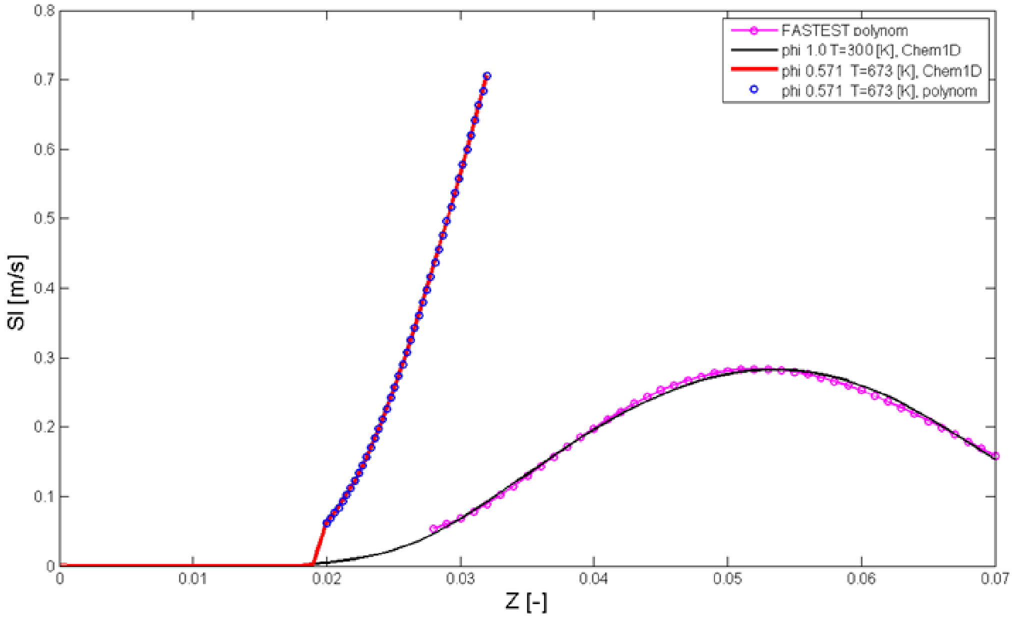

Figure 5.4: Laminar flame speed (S_l [m/s]) of the matrix burner configuration versus methane mixture fraction (Z [-]) comparing to laminar flame speed of non-preheated stoichiometric Methane/air mixture.

5.2 Numerical simulation using ATF combustion model

In the current section the results of the numerical investigation of the matrix burner using ATF combustion model [11, 15] will be offered and discussed. Overall six numerical test cases are simulated using ATF combustion model and different wrinkling models on two different grid levels. The wrinkling models used in this section consist of the linear model proposed by Colin et al. [11] and power-law model of charlette et al. in the non-dynamic [12] and dynamic form [19] using a “Germano” [18] identity as proposed by [21].

5.2.1 Investigation of the non-dynamic power-law wrinkling model using the coarse and fine grid

At first, the simulation results of the test cases 1, 2 (See Tab.5.3) will be discussed and compared together and the experiment. In these two test cases the matrix burner is simulated on two grid levels using the ATF model and the non-dynamic version of the power-law wrinkling model with a fixed beta power ($\beta = 0.5$) [12].

The test case 1 consists of simulation of the matrix burner using the ATF combustion model and the non-dynamic power-law wrinkling model using the coarse grid. For the test case 2 the same combustion model and the power-law wrinkling model as test case 1 is used and the only difference is using a finer grid.

Different thickening factors are used for these test cases as a consequence of the different resolution. Following the definition of the LES filter for the artificially thickened flame as $\Delta = F * \delta_l^0$, for the test case 1 the appropriate filter width is found to be $\Delta = 0.0085$ $[mm]$ and for the test case 2 is $\Delta = 0.005$ $[mm]$.

The profiles of the time averaged axial and the radial velocity components and their corresponding averaged fluctuations, at 50 : 200 [mm] planes nozzle downstream positions are shown in Fig.5.5 and Fig.5.7 respectively. The axial velocity profiles show a good agreement for both test cases and the experiment. The radial velocity profiles and the corresponding averaged fluctuations of the simulation conducted with the fine grid are in good agreement with the experimental data but the simulation using coarser grid shows deviation to the simulation result of the finer grid and the experiment. This deviation also is getting larger with the growing distance of nozzle downstream. The deviation in radial velocity profiles using coarse grid is related one side to the flame dynamics and in other hand to the position of the flame. The observed deviation is just briefly addressed at this section and will be discussed in the coming section and [114].

The profiles of time averaged axial and radial velocity components and their corresponding rms, at 250 : 400 [mm] nozzle downstream positions are shown in Fig.5.6 and Fig.5.8 respectively. The axial velocity profiles show a good agreement for both test cases and the experiment as same as the lower planes. The radial velocity profiles and the corresponding rms of the test case using the finer grid are in good agreement with the experimental data but the test case using coarser grid shows deviation to simulation result of finer grid and experiment. This deviation is getting larger along the downstream direction of the nozzle similar to lower planes.

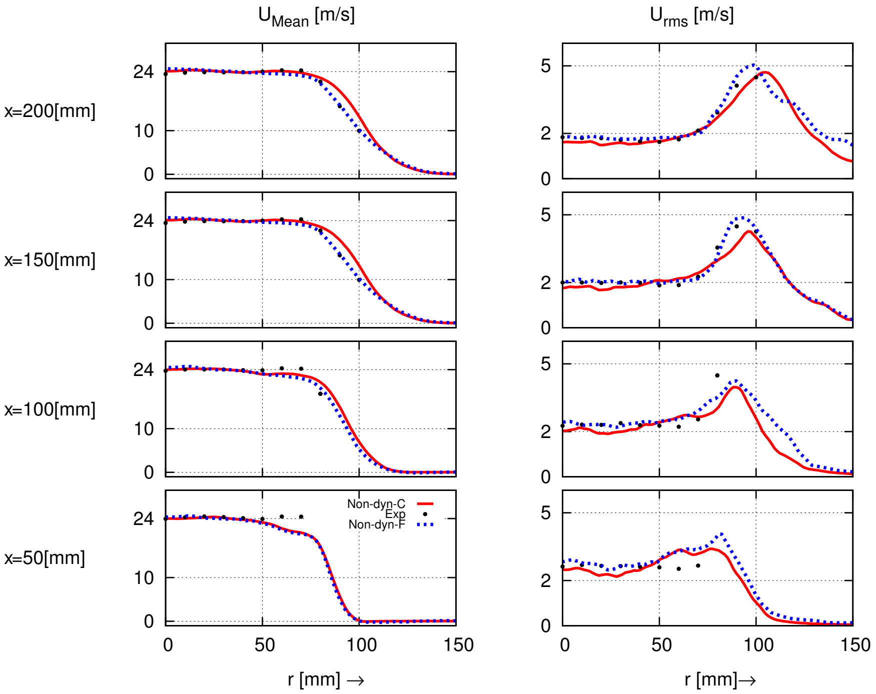

Figure 5.5: Profiles of time averaged axial velocity and the corresponding rms, at 50: 200 [mm] nozzle downstream positions (Solid line: test case 1, dotted line: test case 2, symbols: experiment).

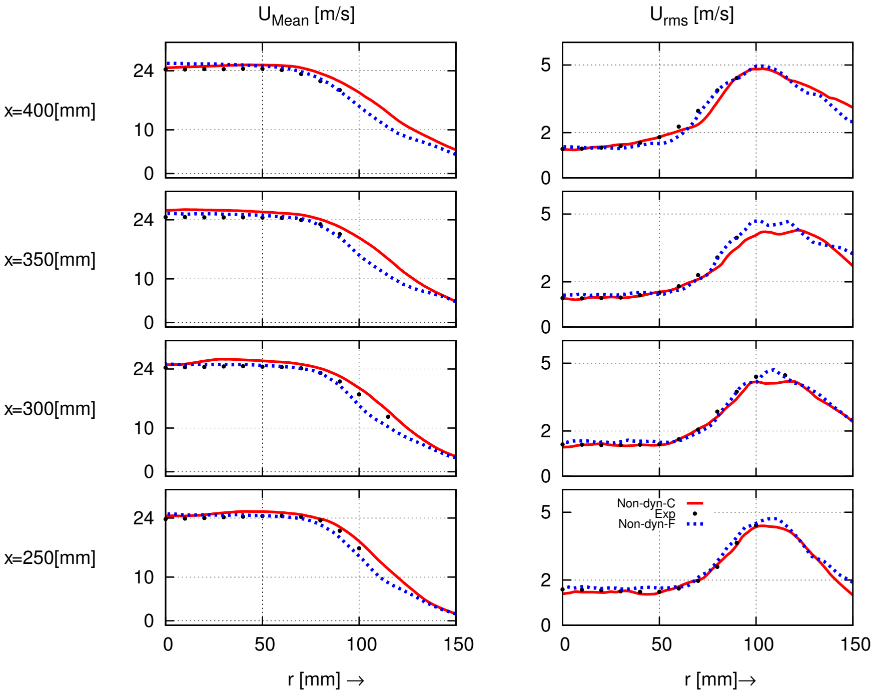

Figure 5.6: Profiles of time averaged axial velocity and the corresponding rms, at 250 : 400 [mm] nozzle downstream positions (Solid line: test case 1, dotted line: test case 2, symbols: experiment).

Fig.5.9 shows the profiles of time averaged temperature and the corresponding rms, planes 50 : 200 [mm] nozzle downstream positions for the test cases 1 and 2. The comparison to the experiment shows that both test cases could predict the structure of the flame. The fine grid has obviously a better agreement in profiles of temperature fluctuations than the coarse grid. The fine grid could also correctly predict the amplitude of the temperature fluctuations in all planes but is slightly shifted in planes 150 [mm] and 200 [mm] downstream of the burner nozzle.

Fig.5.10 shows the profiles of time averaged temperature and the corresponding rms, at 250 : 400 [mm] nozzle downstream positions for the test cases 1 and 2. The comparison to the experiment shows the same result for plane 250 [mm] downstream of the burner nozzle similar to the upstream planes described before. The deviation of the simulated test cases in comparison to the the experiment for the rest planes (300 to 400 [mm]) downstream of the nozzle is very large and is of the interest of this work. The comparison shows that the simulations conducted with both grid levels underestimate the flame height and consequently the flame and flow properties.

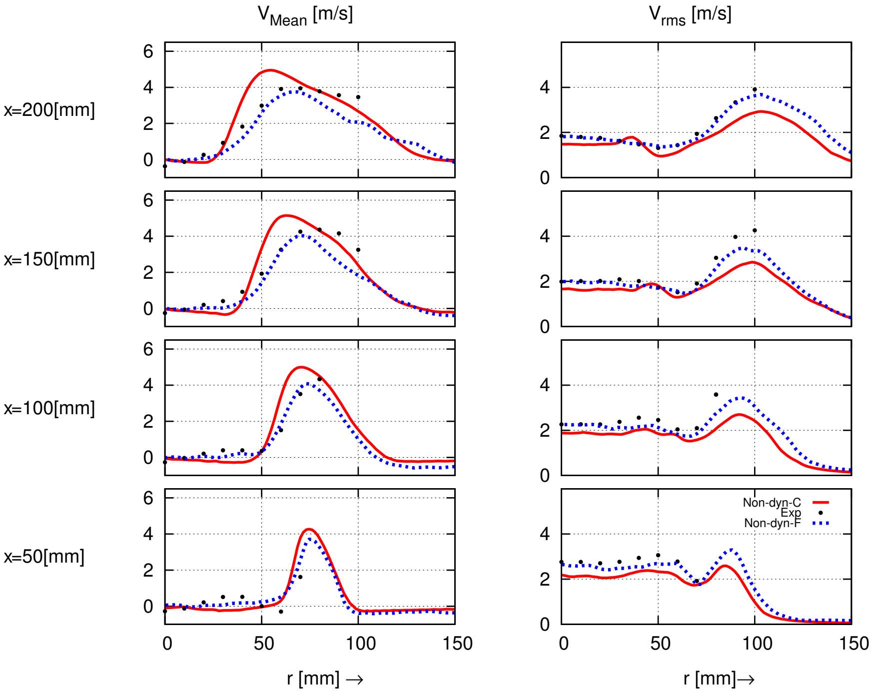

Figure 5.7: Profiles of time averaged radial velocity and the corresponding rms, at 50 : 200 [mm] nozzle downstream positions (Solid line: test case 1, dotted line: test case 2, symbols: experiment).

The flame height in premixed flames is directly related to turbulent flame speed S_t. As described in chap.4 the turbulent flame speed is written as $S_t = \Xi S_l$, therefore the correct prediction of the subgrid scale wrinkling factor is prerequisite for the correct calculation of turbulent flame speed and consequently the flame height in turbulent jet flames.

Back to the simulation results, one can observe that the flame height predicted by the coarser mesh is closer to the experimental data. Although the first guess would say the opposite as the finer grid has better results in resolving the fluctuations. The answer relies on the nature of the model used for these simulations. The power-law constant in the wrinkling model [12] is fixed for these both test cases and has the value of $\beta = 0.5$. The later simulation with the dynamic version of the power-law wrinkling model shows that this value is closer to the dynamically calculated value for the coarse grid for the investigated configuration.

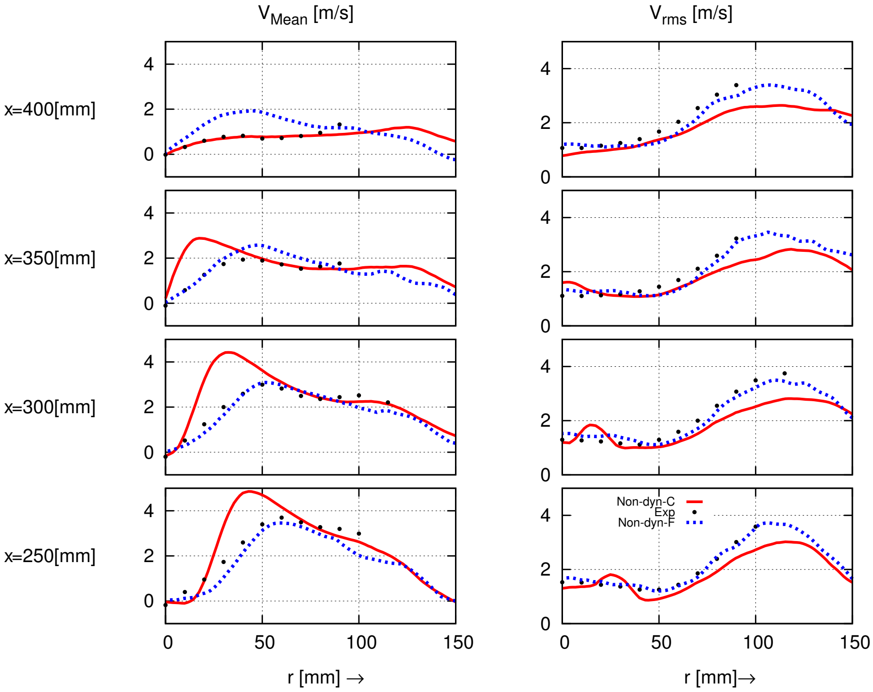

Figure 5.8: Profiles of time averaged radial velocity and the corresponding rms, at 50 : 200 [mm] nozzle downstream positions (Solid line: test case 1, dotted line: test case 2, symbols: experiment).

Fig.5.11 shows the contour plots of the averaged temperature [K], superimposed with the instantaneous flame sensor S [-] (Eq. 4.28) for the test cases 1 and 2. The contour plots show the flame and turbulence interaction. The detached pocket formation is also to observe. The comparison shows that the turbulence and flame interaction is obviously different for both test cases following the different grid resolution.

The simulation using the coarser grid (case 1) could only resolve the larger turbulent scales and is less sensitive to the small scales, the contrary can be observed in the contour plot of simulation using the finer grid.

Although using a finer grid concludes in the resolution of larger portion of the turbulence and flame interaction, results show that the predicted flame height comparing to the experiment and the test case using the coarser mesh is underestimated (See Fig.5.10).

The comparison of the simulation results using ATF combustion model coupled with the non-dynamic formulation of the power-law wrinkling model with the experiment has been shown in the current section (5.2.1). It can be concluded that despite using different grid mesh levels which leads to the different flame and flow resolution, none of the conducted simulation could predict the correct flame height comparing to the experiment. Specially the larger deviation of the flame characteristics for the finer grid mesh shows that just

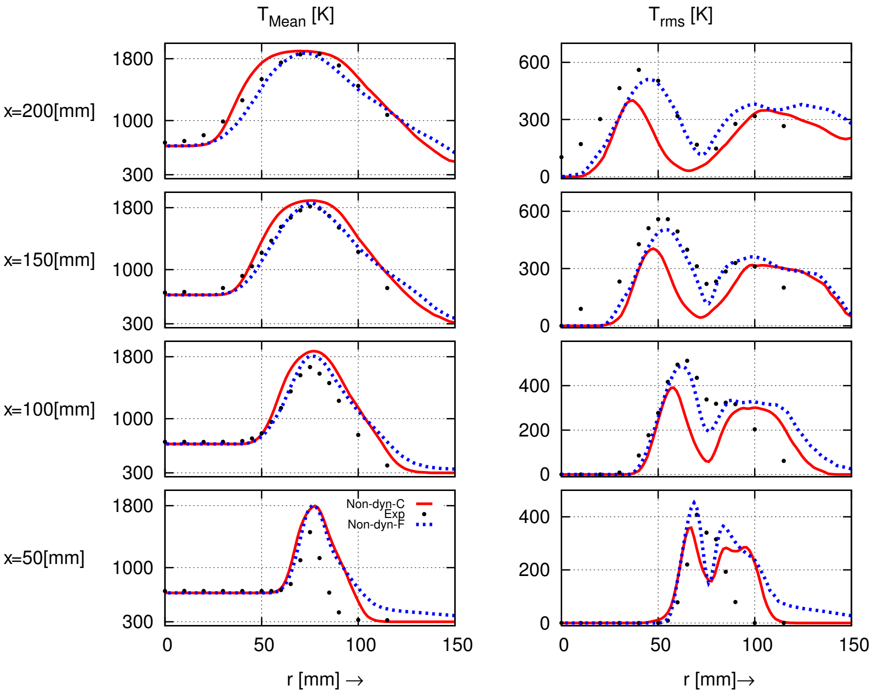

Figure 5.9: Profiles of time averaged temperature and the corresponding rms, at 50 : 200 [mm] nozzle downstream positions (Solid line: test case 1, dotted line: test case 2, symbols: experiment).

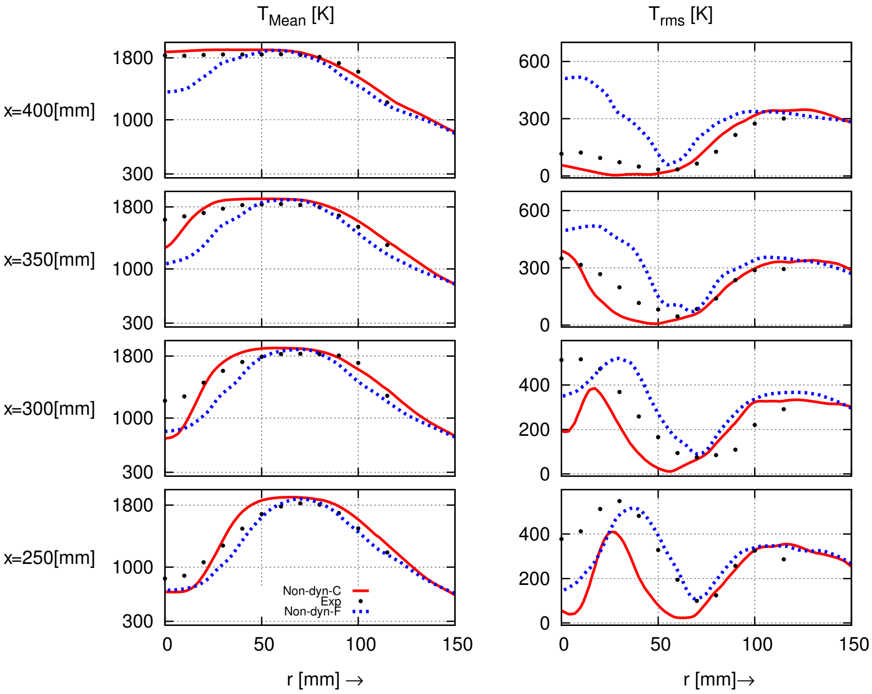

Figure 5.10: Profiles of time averaged temperature and the corresponding rms, at 250 : 400 [mm] nozzle downstream positions (Solid line: test case 1, dotted line: test case 2, symbols: experiment).

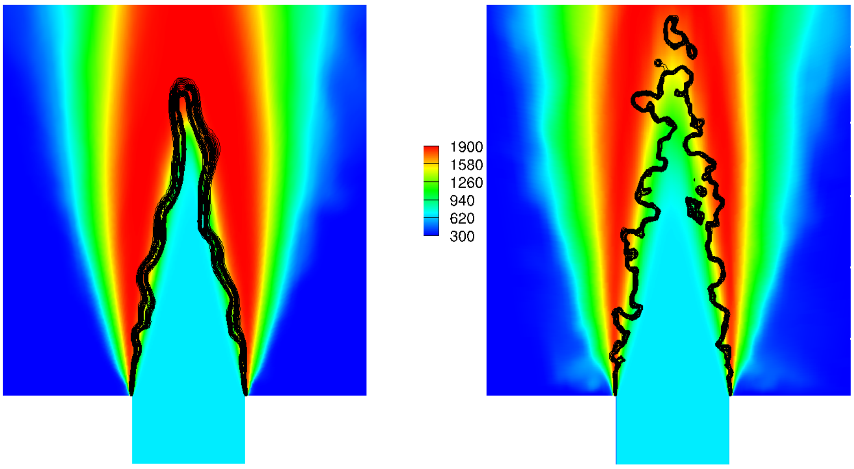

Figure 5.11: Contour plots of the averaged temperature [K], superimposed with the instantaneous flame sensor (lines), left hand side: test case 1 and right hand side: test case 2.

refining the grid mesh does not always leads to a better result. In the next section (5.2.2) we will apply the dynamic version of the power-law wrinkling model coupled with the ATF combustion model using the coarse mesh and compare the results to the non-dynamic version of the wrinkling model and the experiment.

5.2.2 Investigation of the dynamic/non-dynamic power-law wrinkling model using the coarse grid

In this section the simulation results of the test case 1 and the test case 3 will be reviewed and compared to each other and the experiment. The test case 1 as described in the section 5.2.1 is using the non-dynamic model of the power-law wrinkling model [12] with a β value of 0.5 on the coarse grid. The test case 3 uses the same grid and the combustion model as test case 1. The only difference is the utilization of the dynamic formulation of the power-law wrinkling model [19] using a "Germano" identity proposed by wang et al.[21]. The β power is considered to be uniform over whole domain and just subject of the temporal changes. For this purpose the β power is averaged over the whole domain.

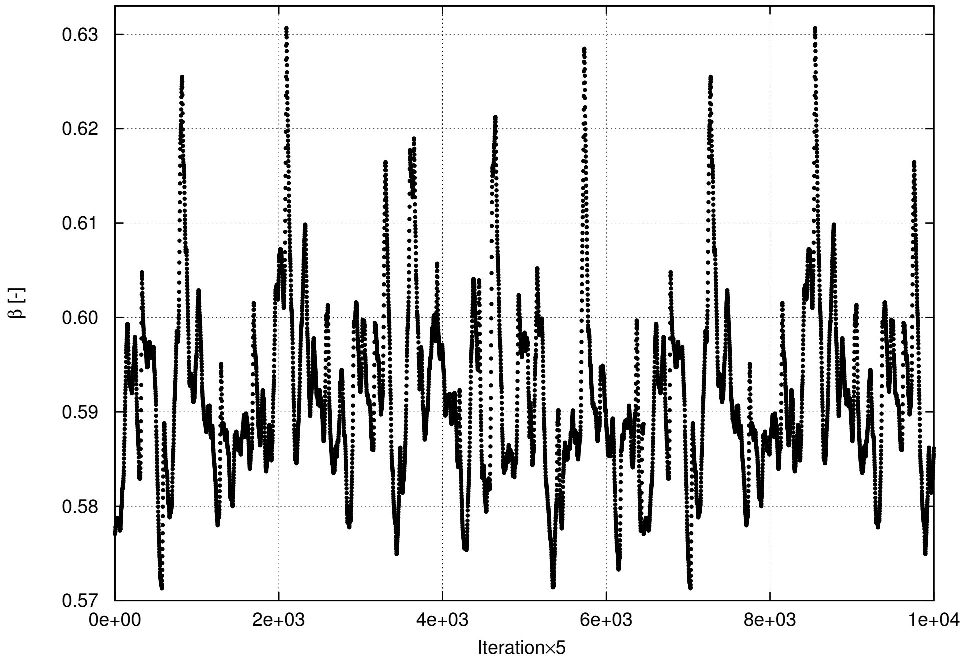

Figure 5.12: The temporal evolution of the β power averaged over whole domain for the test case 3.

The Fig.5.12 shows the temporal evolution of the β power averaged over the whole domain for the test case 3 over 50000 time steps. The dynamic formulation is invoked every five time steps and updated the β power in the wrinkling model. The range of the β power for the test case 3 varies between minimum values of 0.572 and maximum value of 0.632 and has an average of $\beta \approx 0.585$. The average value of the β for the test case 3 resulted from dynamic model is 16% larger than the value proposed by the Charlette et al.[12], considering equilibrium of flame and turbulence. The peaks in the temperature evolution is particularly the consequence of the packet formation in the turbulent jet flow which causes periodic growth and diminishment of the flame surface.

The conducted simulation shows that the β power can not be held as a single constant for this case. To check the impact of the different approaches we will compare the statistical results of the velocity components and the temperature characteristics of the cases 1 and 3 and the experiment.

The Fig.5.13 and Fig.5.14 show the averaged profiles of the axial velocity and the corresponding fluctuations for the planes 50 : 400 [mm] nozzle downstream for test case 1 and test case 3. The comparison shows not a significant difference between test cases. The overall results show good agreement with the experimental results of the both test cases.

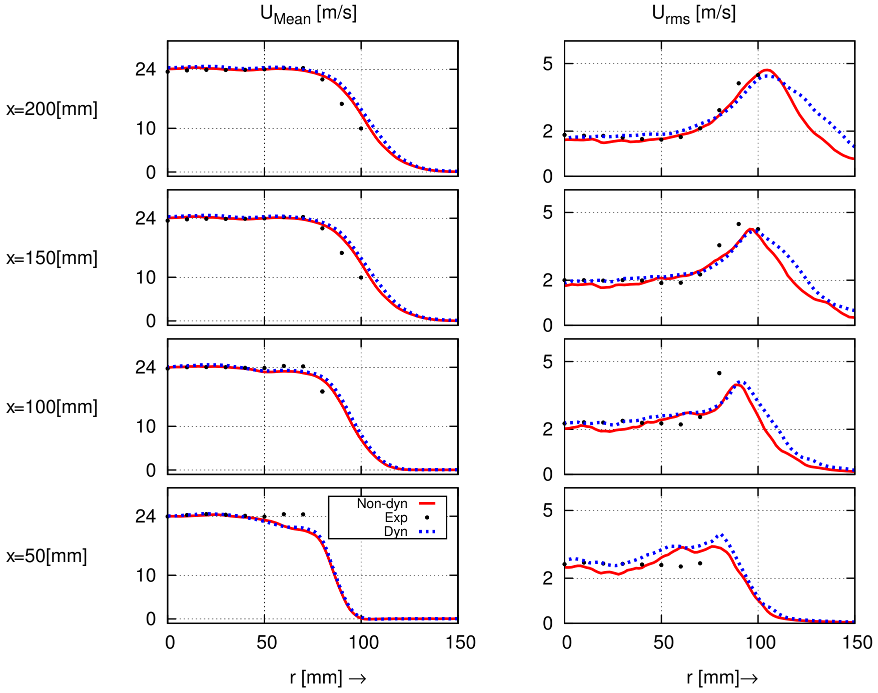

Figure 5.13: Profiles of time averaged axial velocity and the corresponding rms, at 50 : 200 [mm] nozzle downstream positions (Solid line: test case 1, dotted line: test case 3, symbols: experiment).

The averaged profiles of the radial velocity and the corresponding fluctuations for the planes 50 : 400 [mm] nozzle downstream are depicted in Fig.5.15 and Fig.5.16. The comparison shows that for the planes 50 : 250 [mm] downstream of the nozzle, both test cases are in agreement with each other.

The simulation results using the coarse grid show that the radial velocity is overestimated in this planes which is related to the flame dynamics. Conducting simulation with the coarse grid and consequently using higher values for thickening of the flame front, massively alters the turbulence and flame interaction which means lower flame dynamic in this case.

This can be seen in the averaged fluctuations of the radial velocity component. The averaged rms of axial and radial velocities in comparison to the experiment show that the coarse grid is able to resolve the non-reactive flow, however the resolution is not sufficient enough for reactive flows. The averaged rms of velocity in the main jet flame are resolved but in the regions with combustion has a very lower intensity in comparison to the experiment.

The Fig.5.16 shows the averaged profiles of the radial velocity and corresponding fluctuations for the planes 250 : 400 [mm] nozzle downstream. The comparison of the results

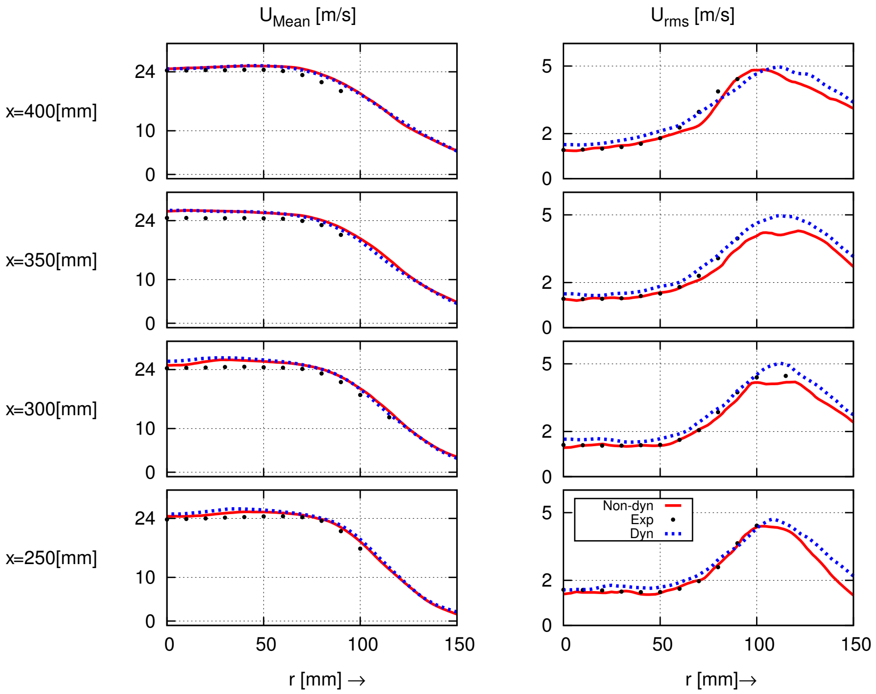

Figure 5.14: Profiles of time averaged axial velocity and the corresponding rms, at 250 : 400 [mm] nozzle downstream positions (Solid line: test case 1, dotted line: test case 3, symbols: experiment).

shows that that using dynamic formulation of the subgrid scale wrinkling model improve the results in planes 250, 300 and 350 [mm] nozzle downstream. The statistical results of the rms values of the radial velocity are also improved.

Fig.5.17 shows the contour plots of the instantaneous dynamic wrinkling model quantities. The test filtered progress variable source term $\widehat{\dot{\omega}_{\tilde{c}}}$ $[kg/m^3s]$ and the source term from test filtered progress variable and the mixture fraction $\dot{\omega}_{\hat{\tilde{c}}}$ $[kg/m^3s]$ for the test case 3. The comparison shows that the test filtered progress variable source term look likes a source term resolved on a coarser mesh grid.

In the current simulation the power β is considered to be constant over the whole domain and has just temporal evolution. To calculate the β using this simplification, the dynamic wrinkling quantities are global averaged over the whole domain.

For instance, the β power calculated for the time step shown in Fig.5.17 have the current values: the averaged resolved source term: $< \dot{\omega}_{\tilde{c}} > \approx$1.440e-3 $[kg/s]$; the averaged test filtered progress variable source term: $< \widehat{\dot{\omega}_{\tilde{c}}} > \approx$ 1.1986e-3 $[kg/s]$ and the averaged source term from test filtered progress variable and mixture fraction: $< \dot{\omega}_{\hat{\tilde{c}}} > \approx$ 1.5981e-3 $[kg/s]$. Using the β (Eq.4.40) delivers the instantaneous value β=0.58. As the Fig.5.17 also shows, in the current snapshot there is no detached pocket and therefore the power value is located in the lower zone as can be seen in Fig.5.12.

The averaged profiles of temperature and corresponding rms for the planes 50 : 400 [mm] nozzle downstream direction are depicted in Fig.5.18 and Fig.5.19. The comparison with the experiment shows that for the planes 50 : 250 [mm] downstream of the nozzle, the results of both test cases are in agreement with experiment. The profile shape could

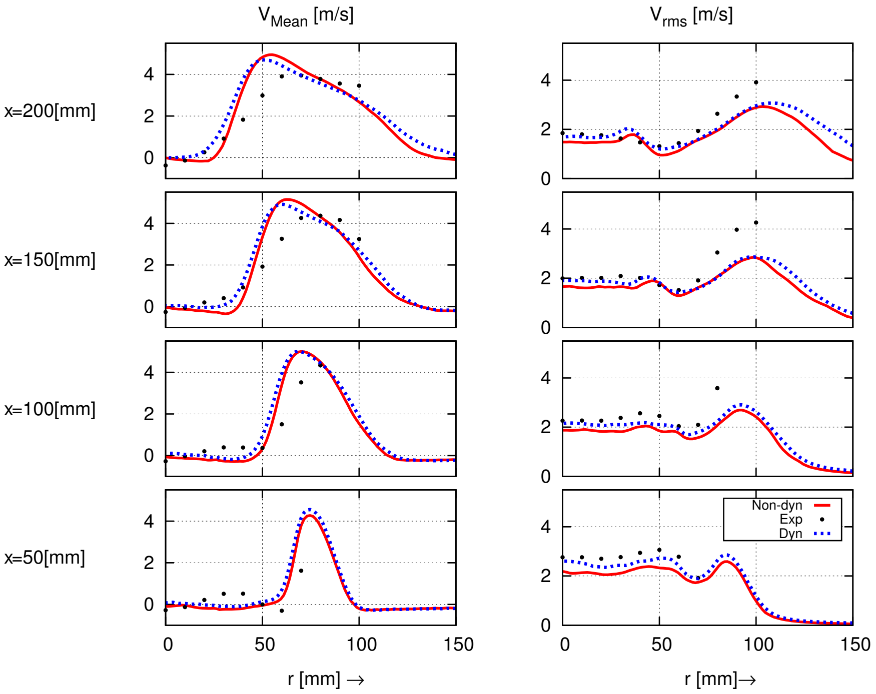

Figure 5.15: Profiles of time averaged radial velocity and the corresponding rms, at 50 : 200 [mm] nozzle downstream positions (Solid line: test case 1, dotted line: test case 3, symbols: experiment).

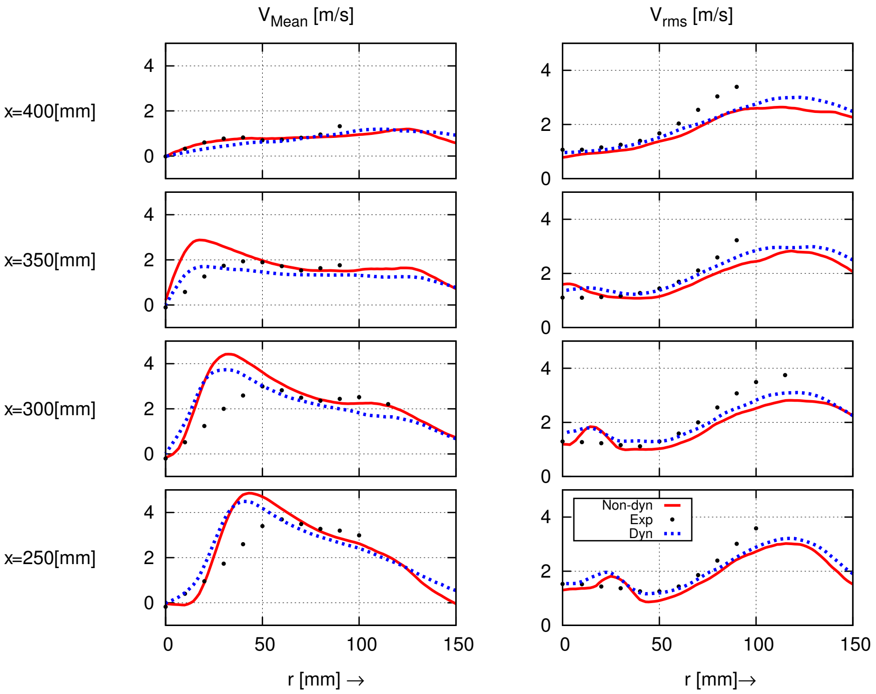

Figure 5.16: Profiles of time averaged radial velocity and the corresponding rms, at 250 : 400 [mm] nozzle downstream positions (Solid line: test case 1, dotted line: test case 3, symbols: experiment).

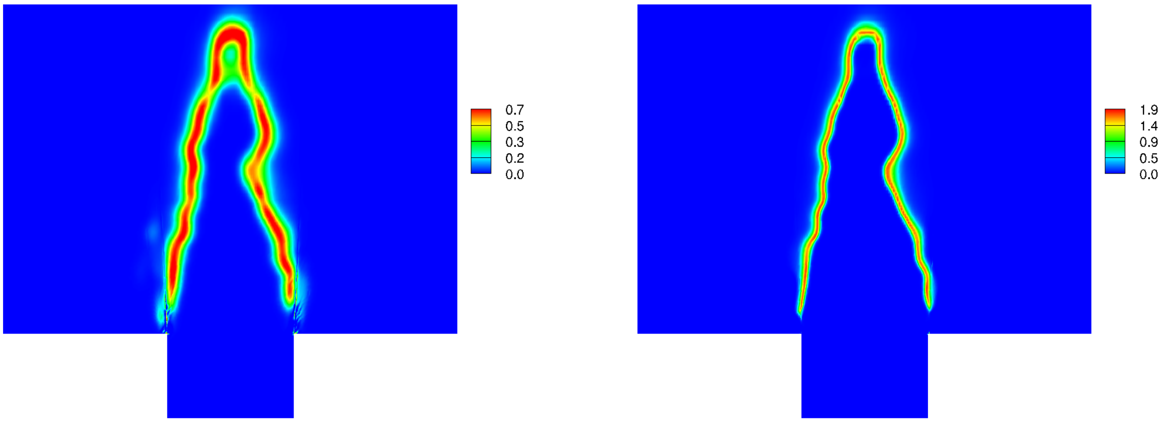

a. b.

Figure 5.17: Contour plots of the instantaneous dynamic wrinkling model quantities. a: test filtered progress variable source term $\widehat{\dot{\omega}_{\tilde{c}}}$ $[kg/m^3s]$; b: source term from test filtered progress variable and mixture fraction $\dot{\omega}_{\hat{\tilde{c}}}$ $[kg/m^3s]$ for the test case 3.

be predicted well. The maximum temperatures of the experimental data and simulation using tabulated detailed chemistry (FGM) are also matching.

The rms profiles of temperature are also following the experimental trend however the amplitudes are lower due to the coarse mesh. The results of simulation in planes $50 : 250$ [mm] using dynamic formulation of subgrid scale wrinkling models reveals that the rms of the temperature are improved as a consequence of higher predicted β value and higher subgrid scale wrinkling factor.

The simulation results of temperature profiles conducted with the dynamic version of the subgrid scale wrinkling models shows a significant improvement comparing to the simulation with fixed β. The averaged temperature profiles at plane 250 and 350 [mm] are in a very good agreement with experiment. Therefore the dynamically calculated subgrid scale wrinkling factor and consequently the averaged turbulent flame speed of the jet is in agreement with the experimental. The same comparison shows that simulation using fixed β fails to predict the flame height and turbulent flame speed.

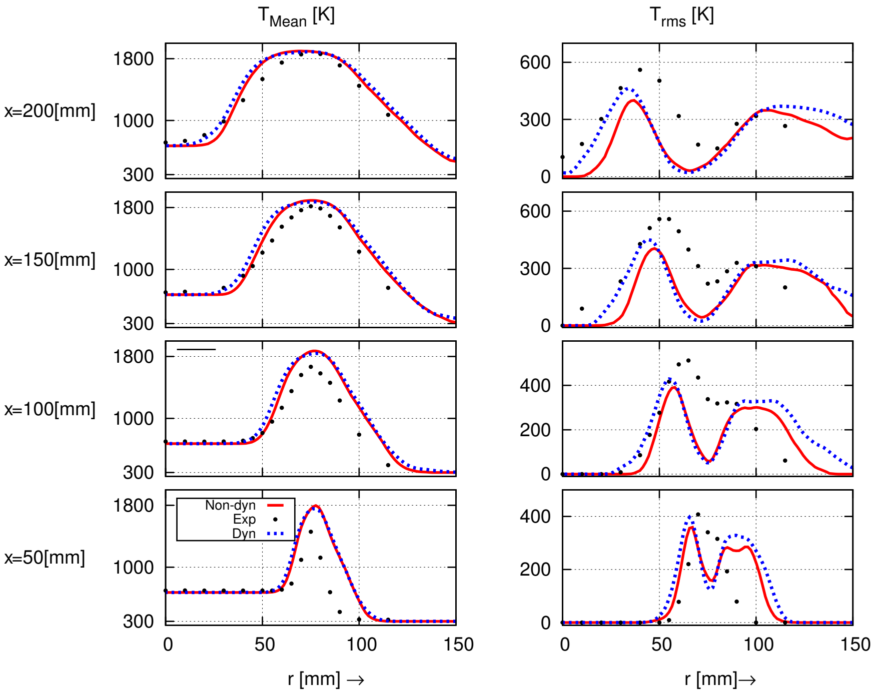

Figure 5.18: Profiles of time averaged temperature and the corresponding rms, at 50 : 200 [mm] nozzle downstream positions (Solid line: test case 1, dotted line: test case 3, symbols: experiment).

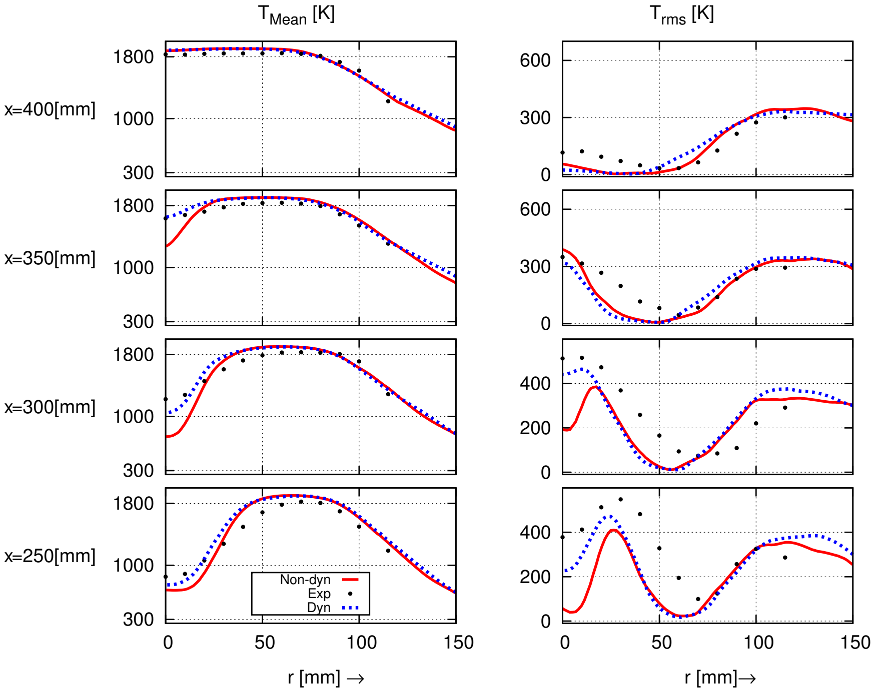

Figure 5.19: Profiles of time averaged temperature and the corresponding rms, at 250 : 400 [mm] nozzle downstream positions (Solid line: test case 1, dotted line: test case 3, symbols: experiment).

5.2.3 Investigation of the dynamic power-law wrinkling model and the effect of the different thickening factors

The test case 4 (See Tab.5.3) uses the ATF combustion model and the dynamic version of power-law wrinkling model of charlette et al. [19] on the fine grid. This test case is divided to three different sub-cases, in which the effects of the different thickening and the thickening strategies are investigated (Tab.5.4).

The appropriate thickening for this configuration found to be $F = 8 \; to \; 10$. For the same boundary condition the thickening factor is set one time to 8 and for other case to 10 to check the effect of increasing thickening factor on the calculated subgrid scale wrinkling factor and power-law wrinkling factor using dynamic model.

For the other test case the thickening factor is calculated dynamically as $F = C[(\Delta_x/\delta_l^0)^2 + 1]^{1/2}$, in which the Δ_x is the grid spacing and the $\delta_l^0 = 1/max(||\nabla(c)||)$, $c(Y_c, Z) = Y_c/max(Y_c)(Z)$ is the laminar flame thickness which is tabulated using CHEM1D [89] code a priory to CFD simulation. The later thickening strategy is to consider beside grid dependency also the mixture fraction dependency specially in shear layer where the premixed mixture is in contact to pure air causing dilution. The thickening is then called mixture fraction dependent and is updated every 5 time steps.

Combustion model	Thickening	Wrinkling model	β power	Grid	Case
ATF	10	Charlette	Dyn (global)	Fine	4a
	8	Charlette	Dyn (global)	Fine	4b
	8dyn	Charlette	Dyn (global)	Fine	4c

Table 5.4: The subcases for test case 4 depending on the different thickening.

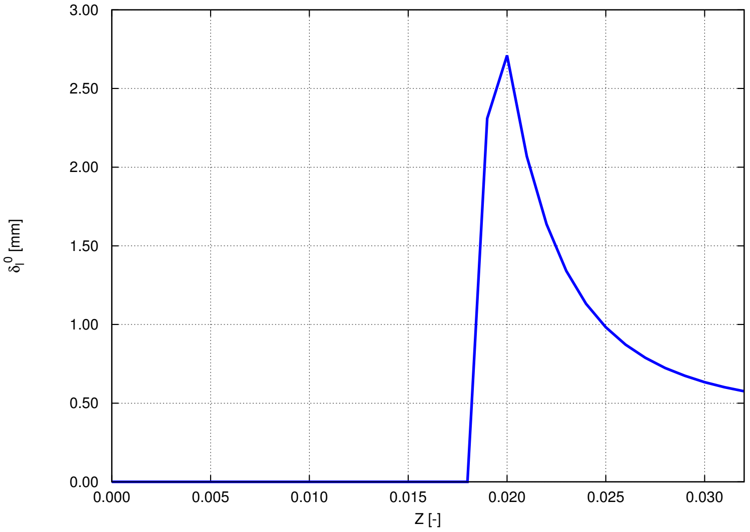

Figure 5.20: Laminar flame thickness $\delta_l^0[mm]$ versus progress variable mixture fraction $Z[-]$ for the matrix burner configuration.

The laminar flame thickness $\delta_l^0[mm]$ of the investigated configuration is depicted in Fig.5.20 dependent to the corresponding mixture fraction. It shows that laminar flame thickness $\delta_l^0[mm]$ increases as the mixture fraction decreases in the investigated configuration.

This behavior is used for implementation of a new flame front thickening strategy to prevent unnecessary thickening. The flame resolution is ensured in which thickening is adjusted to have sufficient resolution in the region with the flame minimum thickness $Z = 0.032[-]$. In regions with higher flame thickness then the thickening factor will be calculated dynamically.

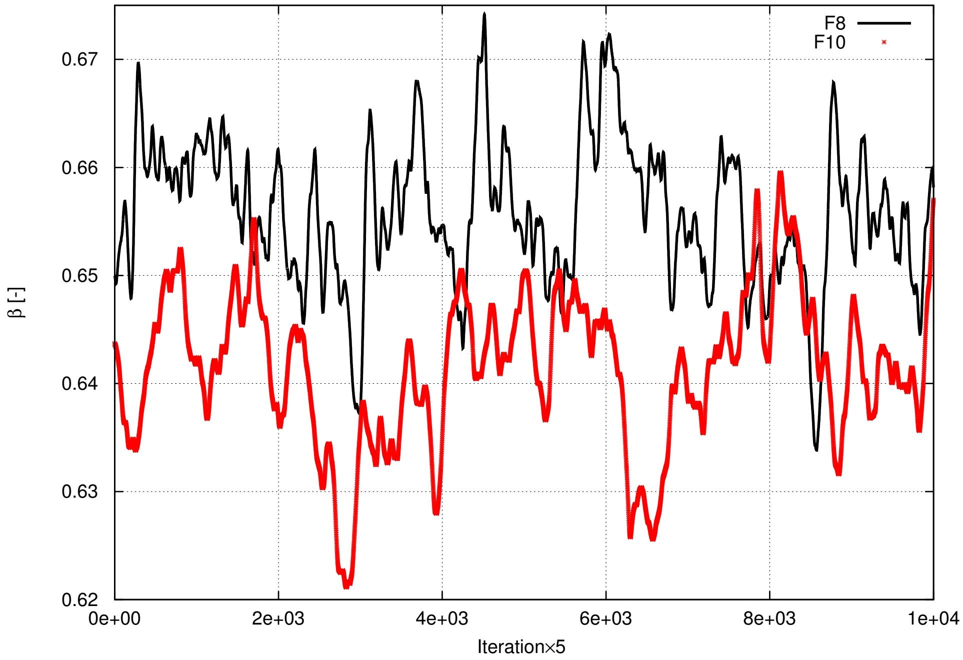

Figure 5.21: The temporal evolution of the β power averaged over whole domain for the test cases 4b (—–) and test case 4a (+++).

The Fig.5.21 shows the temporal evolution of the β power averaged over the whole domain for the test cases 4a and 4b over 50000 time steps. The temporal evolution of the β power for the test case 4c is not shown as it is very similar to the test case 4b. The dynamic formulation is invoked every five time steps and updated the β power in the wrinkling model. The range of the β power for the test case 4a varies between minimum values of 0.62 and maximum value of 0.66 and has an average of $\beta \approx 0.64$. The range of the β power for the test case 4b varies between minimum values of 0.64 and maximum value of 0.67 and has an average of $\beta \approx 0.655$.

The difference between the β power values show the effect of dynamic power-law wrinkling model which is based on the conservation of the flame surface. In these set of simulations the peaks are also to observe which are particularly the consequence of the pocket formation in the turbulent jet flow which causes periodic growth and diminishment of the flame surface as explained in last section.

The profiles of time averaged axial velocity and the corresponding resolved rms, at 50 : 400 [mm] nozzle downstream positions are depicted in Fig.5.22, Fig.5.23 for the cases 4a, 4b and 4c (See Tab.5.4). The results of time averaged axial velocity for all three investigated cases are in very good agreement with each other and also with experiment

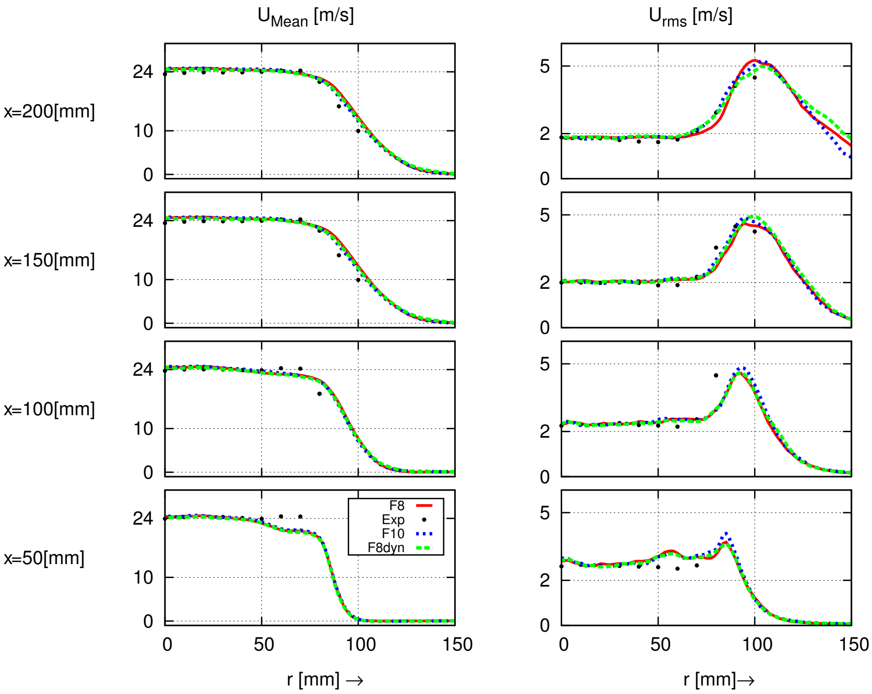

Figure 5.22: Profiles of time averaged axial velocity and the corresponding rms, at 50 : 200 [mm] nozzle downstream positions ((...): test case 4a; (—): test case 4b, (- - -): test case 4c and (●): experiment).

and show no significance change due to different thickening. The axial velocity is constant in the jet main stream and rapidly decreases in the shear layer.

The profiles of resolved rms of axial velocity are also in good agreement with the experiment. The rms of axial velocity shows an intensity of ≈ 13% in the main jet stream at first plane $x = 50[mm]$. The turbulence intensity gradually decreases in direction of nozzle downstream as a result of decaying turbulence. At last measured plane $x = 400[mm]$ of jet nozzle downstream the axial velocity has an intensity of ≈ 6% in the main jet stream. The turbulence intensity increases rapidly in the shear layer and is approximately constant in all investigated planes downstream of the jet nozzle.

The profiles of time averaged radial velocity and the corresponding resolved rms, at 50 : 400 [mm] nozzle downstream positions are illustrated in Fig.5.24, Fig.5.25 for the cases 4a, 4b and 4c (See Tab.5.4). Due to axis symmetric condition of the jet flow the radial velocity for non-reacting flows should have a value of zero. In reacting condition the radial velocity is perpendicular to the flame front.

The shape of the radial velocity follows the temperature profile. As it is known, the artificially thickened flame model has a smearing effect on the flame front. This smearing effect is clearly to observe in the temperature profiles of the flame specially in the early stages of the flame Fig.5.27 where the turbulence and the flame are not in equilibrium. As the radial velocity also follows the profile shape of the temperature, the same effect is to observe.

The test case 4c using dynamic thickening has an slightly thinner flame front than the other two test cases showing the effect of adaptive thickening. As here we have a lean

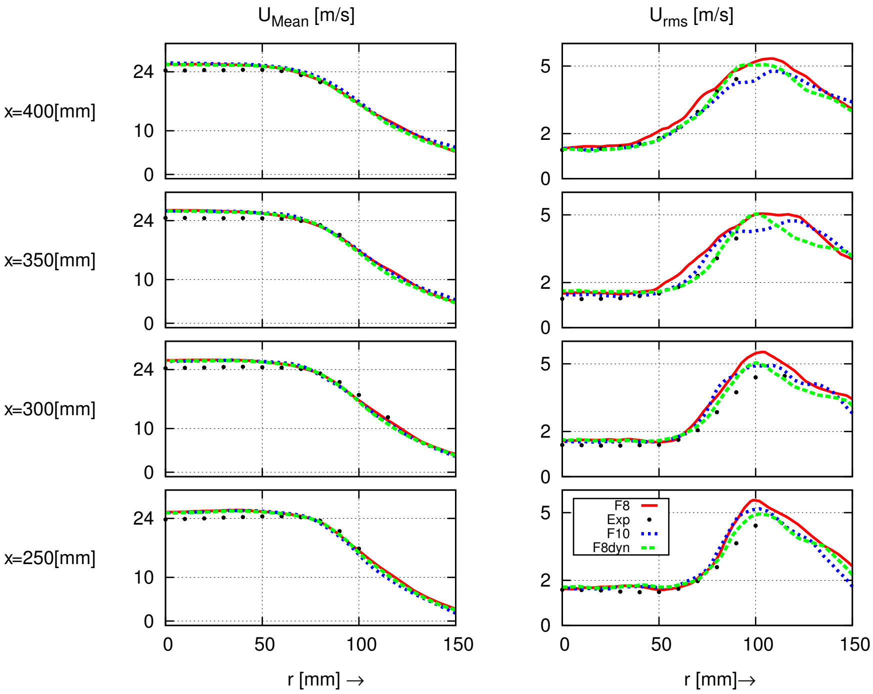

Figure 5.23: Profiles of time averaged temperature and the corresponding rms, at $250:400$ [mm] nozzle downstream positions ((...): test case 4a; (—): test case 4b, (- - -): test case 4c and (●): experiment).

mixture, may be the effect of the adaptive thickening is not so significant. But for sure it will be interesting to investigate this effect in partial premixed flames or flames with very rich mixture fraction.

The profiles of resolved rms of radial velocity are also in good agreement with the experiment. The rms of radial velocity shows an intensity of $\approx 13\%$ in the main jet stream at first plane $x = 50[mm]$, as like as the rms of axial velocity demonstrating the isotropic behavior of the flow. The turbulence intensity gradually decreases in direction of nozzle downstream as a result of decaying turbulence. At last measured plane $x = 400[mm]$ of jet nozzle downstream the axial velocity has an intensity of $\approx 6\%$ in the main jet stream. The turbulence intensity increases rapidly in the shear layer and is approximately constant in all investigated planes downstream of the jet nozzle.

Fig.5.26 shows the contour plots of the instantaneous dynamic wrinkling model quantities. The test filtered progress variable source term $\widehat{\dot{\omega}_{\tilde{c}}}$ $[kg/m^3s]$ and the source term from test filtered progress variable and the mixture fraction $\dot{\omega}_{\hat{\tilde{c}}}$ $[kg/m^3s]$ for the test case 4b. The test filtered progress variable source term look likes a source term resolved on a coarser mesh grid and the maximum magnitude is also decreased.

In the current simulation the power β is considered to be a global value having temporal evolution and constant over whole domain.

The β power calculated for the time step shown in Fig.5.26 have the current values: the averaged resolved source term: $<\dot{\omega}_{\tilde{c}}>\approx$1.119e-3 $[kg/s]$; the averaged test filtered progress variable source term: $<\widehat{\dot{\omega}_{\tilde{c}}}>\approx$ 1.044e-3 $[kg/s]$ and the averaged source term from test filtered progress variable and mixture fraction: $<\dot{\omega}_{\hat{\tilde{c}}}>\approx$ 1.327e-3 $[kg/s]$. Using

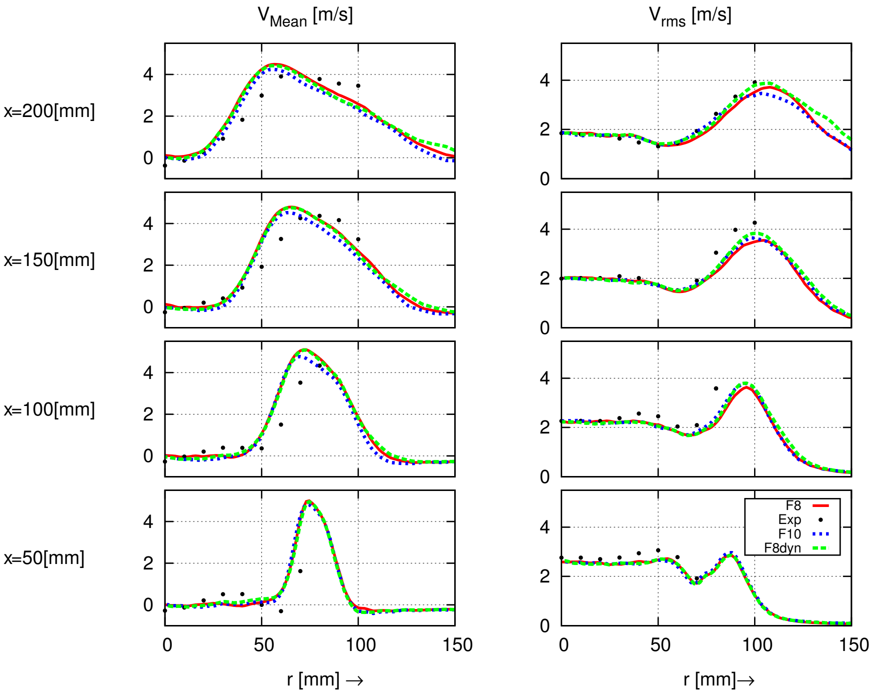

Figure 5.24: Profiles of time averaged radial velocity and the corresponding rms, at 50 : 200 [mm] nozzle downstream positions ((. . .): test case 4a; (—): test case 4b, (- - -): test case 4c and (●): experiment).

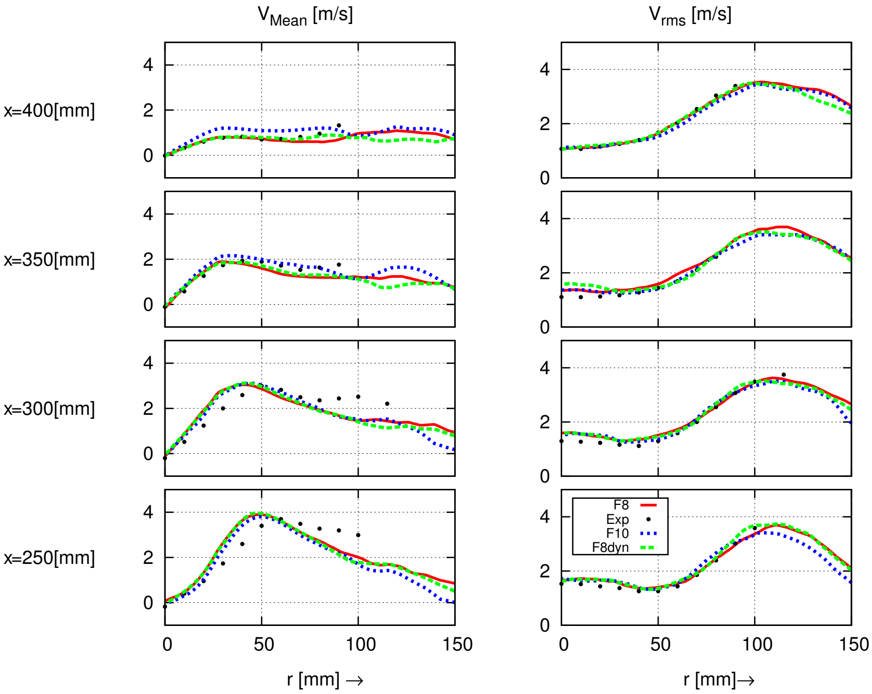

Figure 5.25: Profiles of time averaged radial velocity and the corresponding rms, at 250 : 400 [mm] nozzle downstream positions ((. . .): test case 4a; (—): test case 4b, (- - -): test case 4c and (●): experiment).

the Eq.4.40 delivers the instantaneous value of β=0.654. The same behavior is reported for the cases 4a and 4c which are not shown cause of similarity to the case 4b.

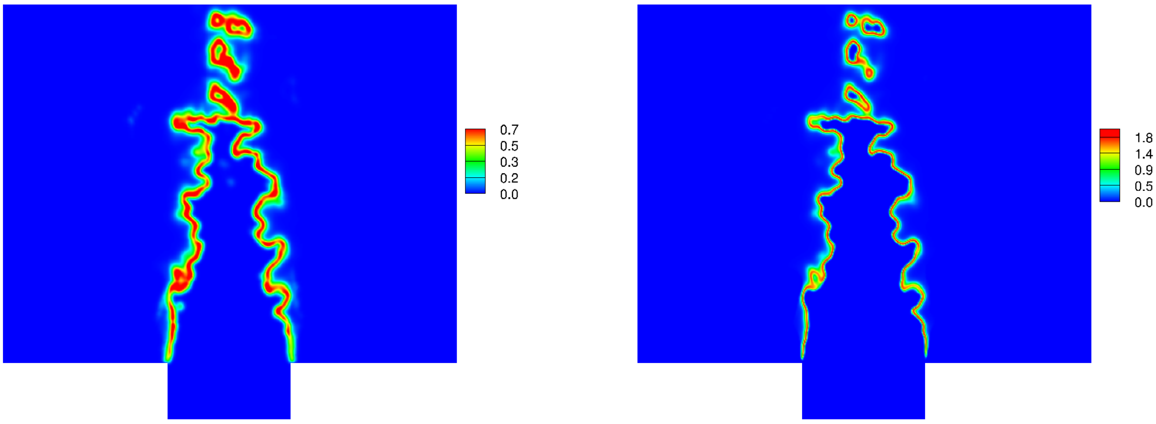

a. b.

Figure 5.26: Contour plots of the instantaneous dynamic wrinkling model quantities. a: test filtered progress variable source term $\widehat{\dot{\omega}_{\tilde{c}}}$ $[kg/m^3s]$; b: source term from test filtered progress variable and mixture fraction $\dot{\omega}_{\hat{\tilde{c}}}$ $[kg/m^3s]$ for the test case 4b.

The profiles of time averaged temperature and the corresponding resolved rms, at 50 : 400 [mm] nozzle downstream positions are depicted in Fig.5.27, Fig.5.28 for the cases 4a, 4b and 4c (See Tab.5.4). In this test cases the dynamic version of the power-law wrinkling model is used in which the power-law factor β is averaged over whole domain and has the same value for all grid cells. The dynamic calculation of the power-law factor β is updated every 5 time step in these investigated cases. The results of time averaged temperature for all three investigated cases are in very good agreement with each other and also with experiment. The flame height is in good agreement with experiment which is consequence of correct prediction of turbulent flame speed. The comparison of the results of the test cases 4a and 4b with different thickening factors shows the same behavior despite different thickening. The results of test cases with smaller thickening factor shows a slightly improvement in flame shape.

It is to note that in artificially thickened flame model the diffusion term is changing due to changes of thickening factor and subgrid scale wrinkling factor. A higher thickening factor increases the diffusion as well which consequently smears the flow front. In our case as we use the dynamic wrinkling model, the subgrid scale wrinkling factor Ξ also increase to compensate the effect of higher thickening. This is certainly a drawback of this model, and may be altered using local averaged dynamic model for the subgrid scale wrinkling factor.

The profiles of resolved rms of temperature are also in good agreement with the experiment. The rms of the temperature shows in all planes two peaks which are related to flame brush and mixing layer. The rms of the temperature also shows the flame dynamic.

The comparison of the simulation results with experiment shows that all three investigated cases can predict the trend of the rms of temperature very well, but have small discrepancies in early stage of the flame which is related to overestimated subgrid scale wrinkling factor using as global value.

In this case, also the effect of different thickening can be traced. As simulation results with higher thickening factor have a higher discrepancies comparing to the test cases having a lower thickening. In this case using an adaptive thickening also have improved the overall results slightly, although has not shown any significant change to the other cases.

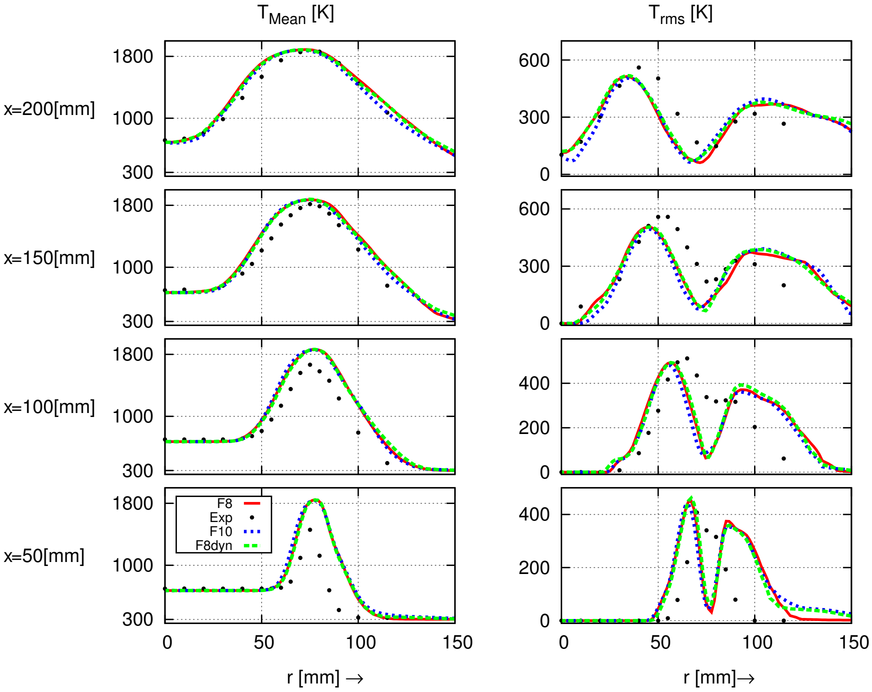

Figure 5.27: Profiles of time averaged temperature and the corresponding rms, at 50 : 200 [mm] nozzle downstream positions ((...): test case 4a; (—): test case 4b, (- - -): test case 4c and (●): experiment).

To show the effect of dynamic calculation of the thickening on the wrinkling model, the profiles of averaged subgrid scale wrinkling factor Ξ, thickening F and $\Xi\omega/F$ are depicted in Fig.5.29 and Fig.5.30. The same boundary condition and grid is used for all cases and the only difference is the thickening factor $F = \Delta/\delta_l^0$. This is to close the effect of any other parameter in this study rather than thickening factor.

It is to note that one can say, using a coarse or finer grid is equal to using different thickening factor. It is true, but in formulation of subgrid scale wrinkling factor, the subgrid scale turbulence intensity u'_Δ entering subgrid scale wrinkling factor is also being modeled (See Eq.4.27). The modeled subgrid scale turbulence intensity u'_Δ is also dependent on the mesh size Δ_x which causes another dependency in the study. Therefore we chose the same grid for this study to have only one changing parameter.

The profiles of averaged thickening factor F and averaged subgrid scale wrinkling factor Ξ show that with an increase in thickening factor the subgrid scale wrinkling is also increases to compensate the flame surface lost due to thickening. It is also to observe that the values of resolved reaction rate $\Xi\omega/F$ are approximately conserved for different thickening at all planes downstream of the nozzle.

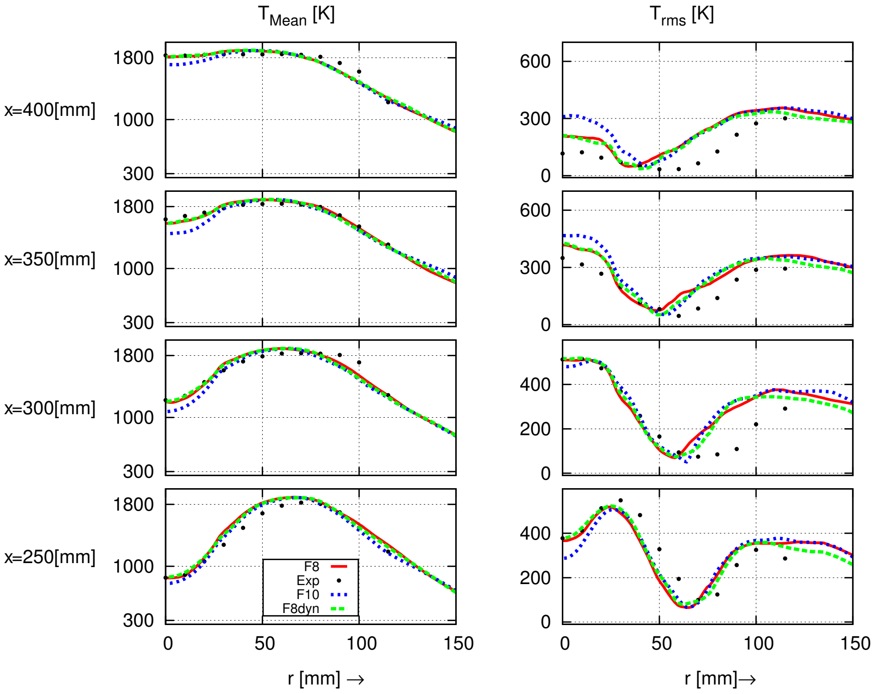

Figure 5.28: Profiles of time averaged temperature and the corresponding rms, at 250 : 400 [mm] nozzle downstream positions ((···): test case 4a; (—): test case 4b, (- - -): test case 4c and (●): experiment).

In the current section the influence of different thickening factors and different thickening strategies on the dynamically calculated wrinkling factor is investigated. The investigation shows that the dynamically calculated β changes also according tho a change in thickening factor. The overall comparison to the experiment and the different cases conducted under using different thickening factors and strategies show very good agreement. The investigation shows that the flame surface area is conserved using dynamic version of the power-law wrinkling factor. Hence the flame and flow characteristics prediction are not varying under a change in thickening factor.

In the next section the results of simulations using ATF combustion model coupled with power-law wrinkling model (dynamic and non-dynamic) [19, 21] and the linear model [11] will be presented and discussed.

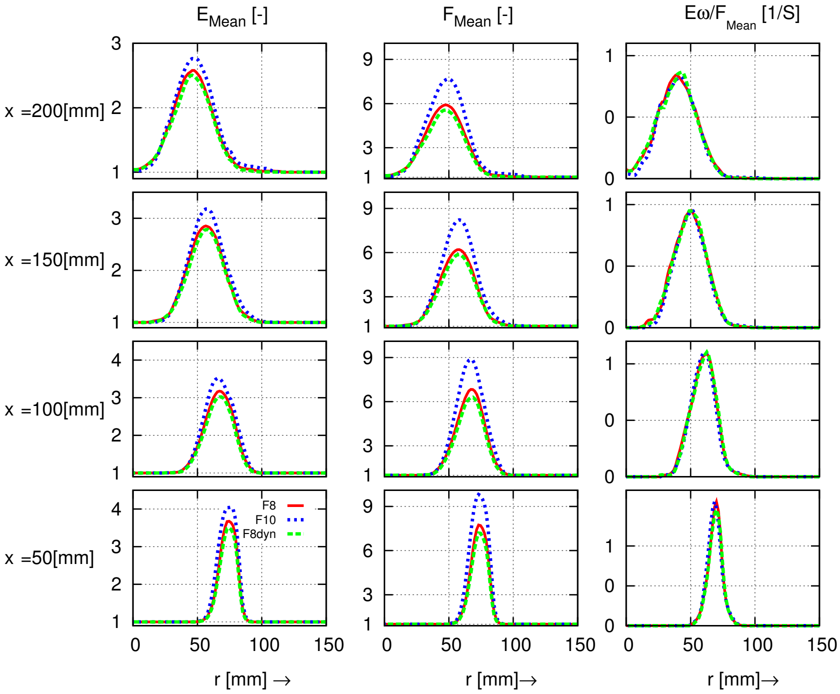

Figure 5.29: Profiles of time averaged E F, at 50 : 200 [mm] nozzle downstream positions ((...): test case 4a; (—): test case 4b, (- - -): test case 4c and (●): experiment).

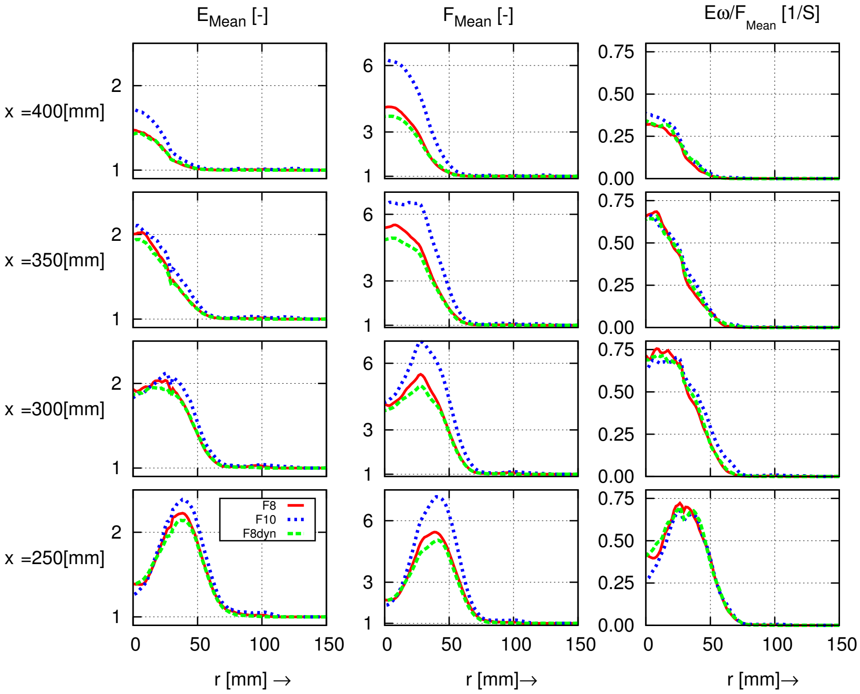

Figure 5.30: Profiles of time averaged E F, at 250 : 400 [mm] nozzle downstream positions ((...): test case 4a; (—): test case 4b, (- - -): test case 4c and (●): experiment).

5.2.4 Investigation of the dynamic/non-dynamic power-law wrinkling model and the linear wrinkling model using the fine grid

In the current section the simulation results of the test case 2 and the test case 4a (See Tab.5.4) and the test case 6 will be explained and compared to each other and the experiment. The test case 2 as described in section 5.2.1 is using the non-dynamic version of the power-law wrinkling model [12] with a β value of 0.5 using the fine grid. The test case 4a uses the same grid and combustion model as test case 2. The only difference is utilization of dynamic formulation of the power-law wrinkling model [19, 21] (Eq.4.20). The β power is considered to be uniform over whole domain and is just object of temporal changes. For this purpose the β power is averaged over whole domain. For the test case 6 the linear wrinkling model proposed by Colin et al. [11] (Eq.4.17) is used. The test case 6 also uses the fine grid (See Tab.5.3). The thickening factor is held as $F = 10$ for all three test cases which is applied just on the flame front using the flame sensor.

The purpose of the this comparison is to investigate the effect of the utilization of the different subgrid scale wrinkling models on the flow and flame characteristics.

The Fig.5.31 shows the temporal evolution of the β power averaged over whole domain for the test case 4a over 50000 time steps. The dynamic formulation is invoked every five time steps and updated the β power in the wrinkling model. The range of the β power for the test case 4a varies between minimum values of 0.625 and maximum value of 0.665 and has an average of $\beta \approx 0.64$. The average value of β for test case 3 resulted from dynamic model is approximately 28% larger than the value proposed by the Charlette et al.[12] considering equilibrium of flame and turbulence. The fluctuation in the temporal evolution of the β power is particularly consequence of the packet formation in the turbulent jet flow which causes periodic growth and diminishment of the flame surface and is corresponding to very small flame surfaces.

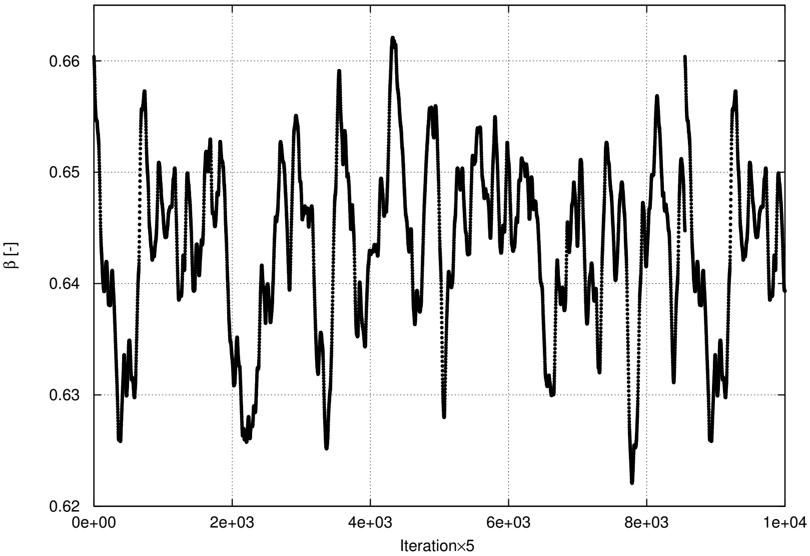

Figure 5.31: The temporal evolution of the β power averaged over whole domain for the test case 4a (See Tab.5.4).

The conducted simulation shows that the β power can not be held as a single constant for this case. To check the impact of different approaches the statistical results of the velocity and temperature for all three cases are compared to the experiment.

Fig.5.32 shows the contour plots of the averaged temperature [K], superimposed with the instantaneous RPV source term (lines) for the case 4a using dynamic power-law wrinkling model and the test case 6 using the linear wrinkling model. The different predicted flame height is clear to observe for both test cases. It is also to recognize that the resolved flame using linear wrinkling model is thinner than the resolved flame using dynamic power-law wrinkling model. The later results are directly a consequence of higher predicted wrinkling factor using dynamic power-law wrinkling model. As the diffusion is also directly increased, thus the resolved temperature profile is thicker. This effect can be better recognized in the comparison of the quantitative data with the experiment.

a. b.

Figure 5.32: Contour plots of the averaged temperature [K], superimposed with the instantaneous RPV source term (lines), a: test case 4a and b: test case 6.

The Fig.5.33 and Fig.5.34 show the averaged profiles of axial velocity and corresponding rms of the planes 50 : 400 [mm] nozzle downstream for test case 4a, 2 and the test case 6. The comparison shows no significant difference between these test cases. The overall results show also good agreement with experimental results for all three test cases.

The averaged profiles of radial velocity and corresponding rms of the planes 50 : 400 [mm] nozzle downstream are depicted in Fig.5.35 and the Fig.5.36. The comparison shows that for the planes 50 : 250 [mm] downstream of the nozzle, all test cases are in agreement with each other and the experiment. As explained before, the higher diffusivity causes a thicker flame front as can be observed in the current planes of the test case 4a.

The Fig.5.36 shows the averaged profiles of radial velocity and corresponding rms of the planes 250 : 400 [mm] nozzle downstream. The comparison of results shows that using dynamic formulation of the subgrid scale wrinkling model improves the results in all planes downstream of the nozzle. The statistical results of the rms values of the radial velocity are also improved. The statistical results for the test case 4a using dynamic

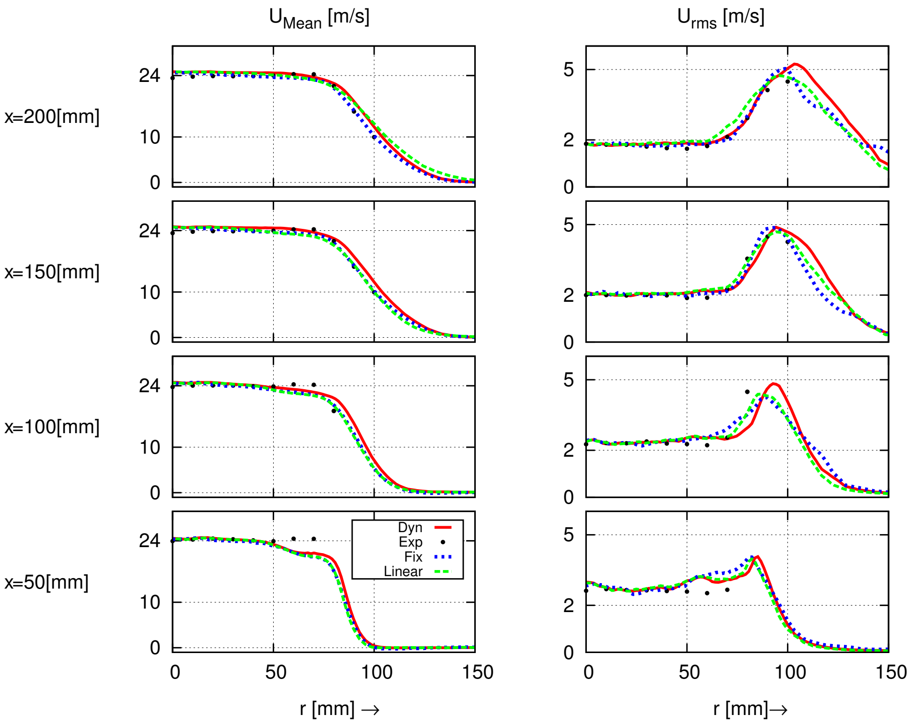

Figure 5.33: Profiles of time averaged axial velocity and the corresponding rms, at 50 : 200 [mm] nozzle downstream positions (—): test case 4a; (...): test case 2, (- - -): test case 6 and (●): experiment.

formulation of the power-law subgrid scale wrinkling model are in very good agreement with the experiment. The non-dynamic formulation of the power-law wrinkling model and linear model overestimated the flame height and consequently underestimates the turbulence flame speed as can be seen in plane 400 [mm] nozzle downstream. In which the radial velocity should be zero, which only the test case 4a using dynamic power-law wrinkling model could predict the correct value.

The averaged profiles of temperature and corresponding fluctuations for the planes 50 : 400 [mm] nozzle downstream are depicted in Fig.5.37 and the Fig.5.38. The comparison with the experiment shows that for the planes 50 and 100 [mm] downstream of the nozzle, the results of all three test cases are in agreement with experiment.

The deviations growth in planes 150 [mm] downward in which the test cases 2 and 7 underpredict the flame thickness. The flame is shifted to the right hand side as can be observed in averaged fluctuations of the temperature profiles. The profile shape could be predicted well. The maximum temperatures of the experimental data and simulation using tabulated chemistry (FGM) are also matching.

The rms profiles of temperature are also in a good agreement with the experimental results. The results of simulation in planes 50 : 250 [mm] using dynamic formulation of subgrid scale wrinkling models reveals that the rms of the temperature are improved as a consequence of higher predicted β value and higher subgrid scale wrinkling factor.

The simulation results of temperature profiles conducted with the dynamic version of the subgrid scale wrinkling models shows a significant improvement comparing to the simulation with fixed β and using a linear wrinkling model for the planes 250 : 400 [mm]

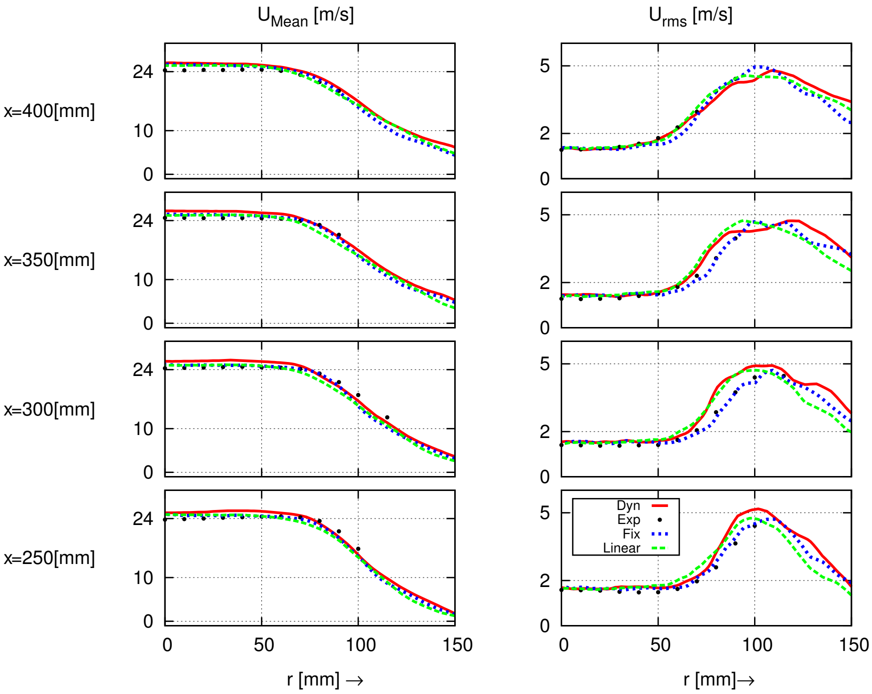

Figure 5.34: Profiles of time averaged axial velocity and the corresponding rms, at 250 : 400 [mm] nozzle downstream positions (—): test case 4a; (…): test case 2, (- - -): test case 6 and (●): experiment.

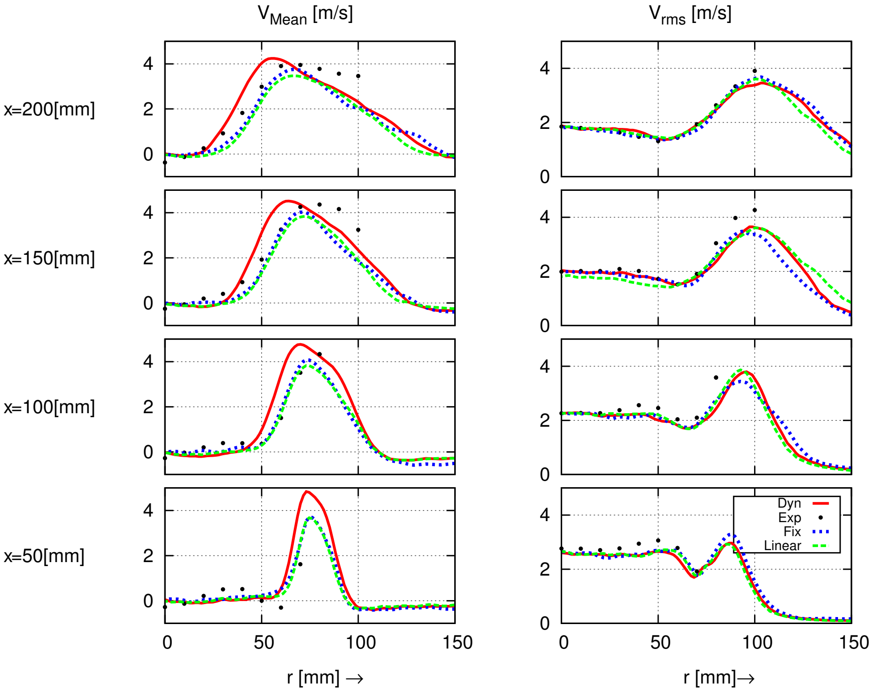

Figure 5.35: Profiles of time averaged radial velocity and the corresponding rms, at 50 : 200 [mm] nozzle downstream positions (—): test case 4a; (…): test case 2, (- - -): test case 6 and (●): experiment.

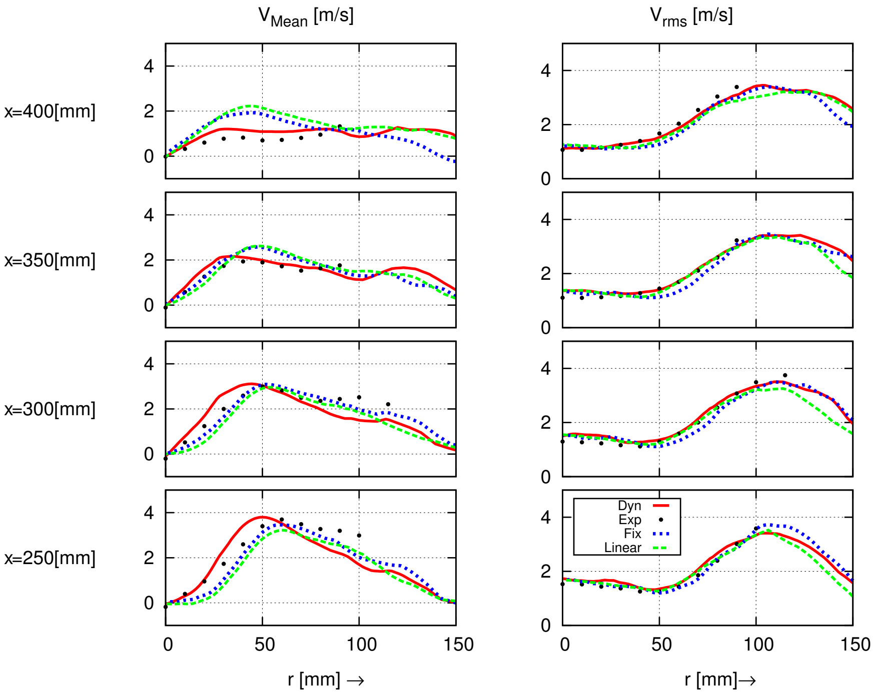

Figure 5.36: Profiles of time averaged radial velocity and the corresponding rms, at 250 : 400 [mm] nozzle downstream positions (—): test case 4a; (...): test case 2, (- - -): test case 6 and (●): experiment.

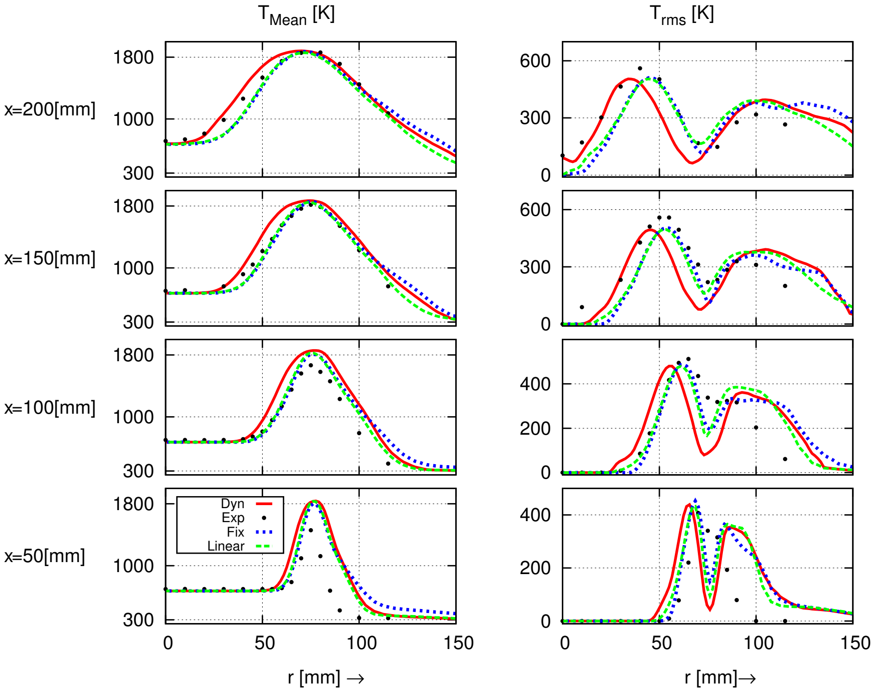

Figure 5.37: Profiles of time averaged temperature and the corresponding rms, at 50 : 200 [mm] nozzle downstream positions (—): test case 4a; (...): test case 2, (- - -): test case 6 and (●): experiment.

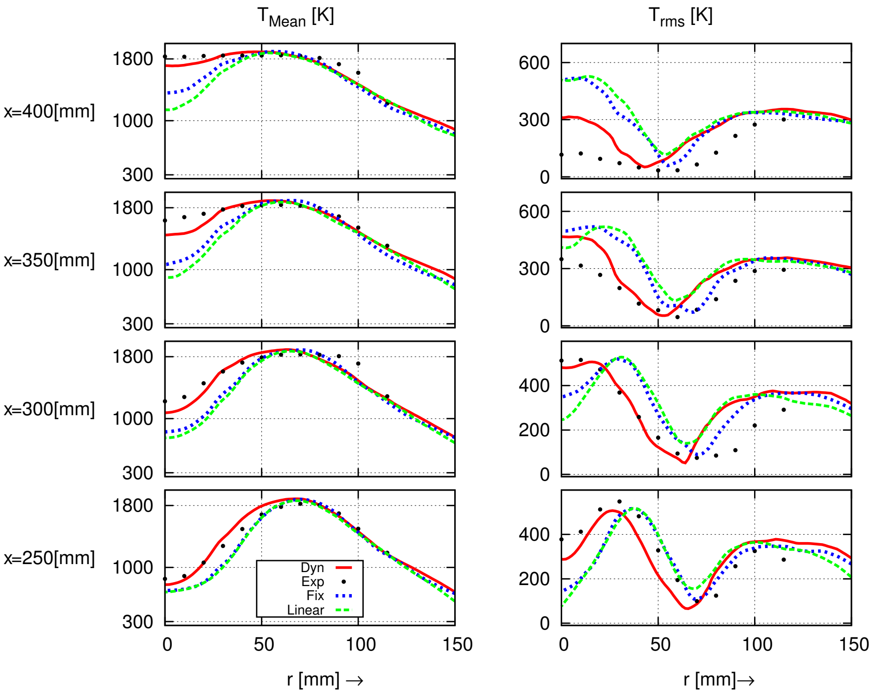

Figure 5.38: Profiles of time averaged temperature and the corresponding rms, at 250 : 400 [mm] nozzle downstream positions (—): test case 4a; (...): test case 2, (- - -): test case 6 and (●): experiment.

nozzle downstream.

The averaged temperature fluctuation profiles in all planes are also in a very good agreement with experiment for the test case 4a using dynamic power-law wrinkling model. The same comparison shows that simulations using power-law wrinkling model with fixed β and also the linear models fail to predict the flame height and turbulent flame speed.

The current investigation shows that using a finer grid alone do not conclude in a correct prediction of flame characteristics. For correct prediction of the flame characteristics one should use flame surface conservative methods as dynamic power-law wrinkling model.

5.2.5 Investigation of the dynamic power-law wrinkling model using the coarse and fine grid

In this section the simulation results of the test case 3 (See Tab.5.3) and the test case 4b (See Tab.5.4) will be reviewed and compared to each other and experiment. The test case 3 as described in section 5.2.2 is using dynamic model of subgrid scale power-law wrinkling model [19] on the coarse grid. The test case 4b as described in section 5.2.3 uses the same combustion model and the subgrid scale wrinkling model as the test case 3. The only difference is using the finer grid. The β power is considered to be uniform for whole domain and is just object of temporal changes for both simulations. For this purpose the β power is averaged over whole domain.

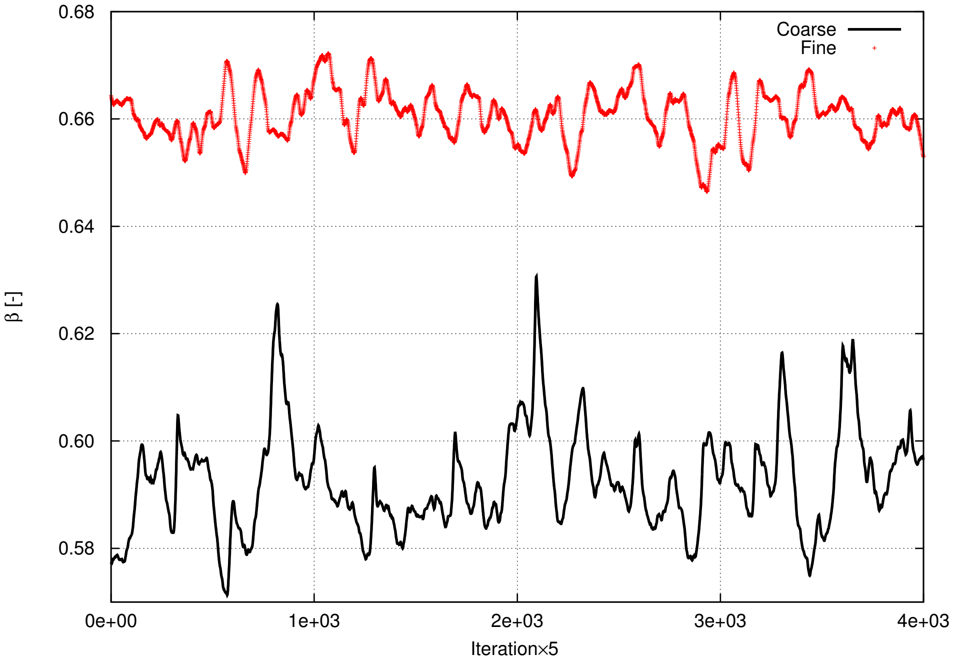

Figure 5.39: The temporal evolution of the β power averaged over whole domain for the test cases 3 (—–) and test case 4a (+++) (See Tab.5.3, 5.4).

The temporal evolution of β power is depicted in Fig.5.39 for both cases. The β power shows a significant difference for both cases. The mean β power for the coarse gird is about 0.59 and shows a value of 0.66 for the test case using the finer grid. Although the averaging is just to show the deviation from the fixed value (β= 0.5) and is not used for the simulations. The comparison clearly shows that using a non-dynamic version with a constant value is not justified for both simulations.

Fig. 5.40 shows the contour plots of the averaged temperature [K], superimposed with the instantaneous reaction progress variable source term. The quantitative comparison shows that the averaged flame height is similar for the both cases although the flame and turbulence interaction is more intensive for the test case 4b using the finer grid. The comparison also shows that using a coarser grid concludes in a thicker resolved flame which is a consequence of using higher thickening factor. As the dynamic power-law wrinkling factor assures the conservation of flame surface the both simulation should show the same

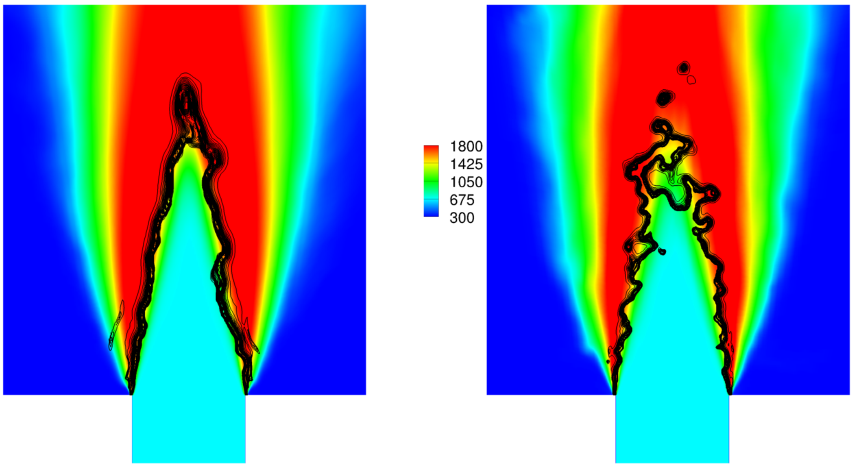

Figure 5.40: Contour plots of the averaged temperature [K], superimposed with the instantaneous RPV source term (lines), left: case 3 and right: case 4b.

characteristics in the time averaged quantities.

The Fig.5.41 and Fig.5.42 show the averaged profiles of axial velocity and corresponding rms of the planes 50 : 400 [mm] nozzle downstream for test case 3 and test case 4b. The comparison shows no significant difference between test cases. The overall results show good agreement with experimental results for both test cases.

The averaged profiles of radial velocity and corresponding rms of the planes 50 : 400 [mm] nozzle downstream are depicted in Fig.5.43 and Fig.5.44. The comparison shows that for all planes downstream of the nozzle, the result of test case 4b is in very good agreement with the experiment. As described in section 5.2.2 the result of test case 3 has a deviation to experimental data which is related to flame dynamics. As also described in section 5.2.1, using a finer grid results in better resolution and ultimately a better prediction in the rms of values in all planes.

The averaged profiles of temperature and corresponding rms of the planes 50 : 200 [mm] nozzle downstream are depicted in Fig.5.45 . The comparison with the experiment shows that for the planes 50 : 200 [mm] downstream of the nozzle, the results of both test cases are in agreement with experiment. In this planes there is no significant change comparing to the simulations non-dynamic version of the wrinkling factor as described in section 5.2.1. The finer mesh has a better resolution in fluctuations as expected.

The averaged profiles of temperature and corresponding rms of the planes 250 : 400 [mm] nozzle downstream are depicted in Fig.5.46.

The profiles of temperature fluctuation for the test case 4b are also in a good agreement with the experimental results and shows the difference in using a finer grid in comparison to results of test case 3.

The simulation results of temperature profiles conducted with the dynamic version of the subgrid scale wrinkling models show a significant improvement comparing to the simulation with fixed β (See section 5.2.1). The comparison of results of both test cases 3 and

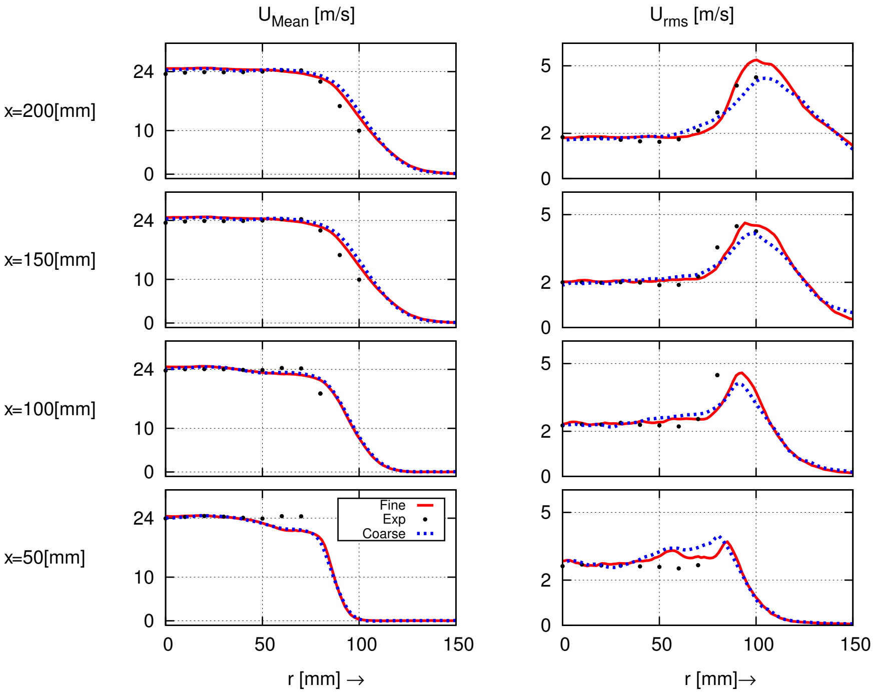

Figure 5.41: Profiles of time averaged axial velocity and the corresponding rms, at 50 : 200 [mm] nozzle downstream positions (Solid line: test case 4b, dotted line: test case 3, symbols: experiment).

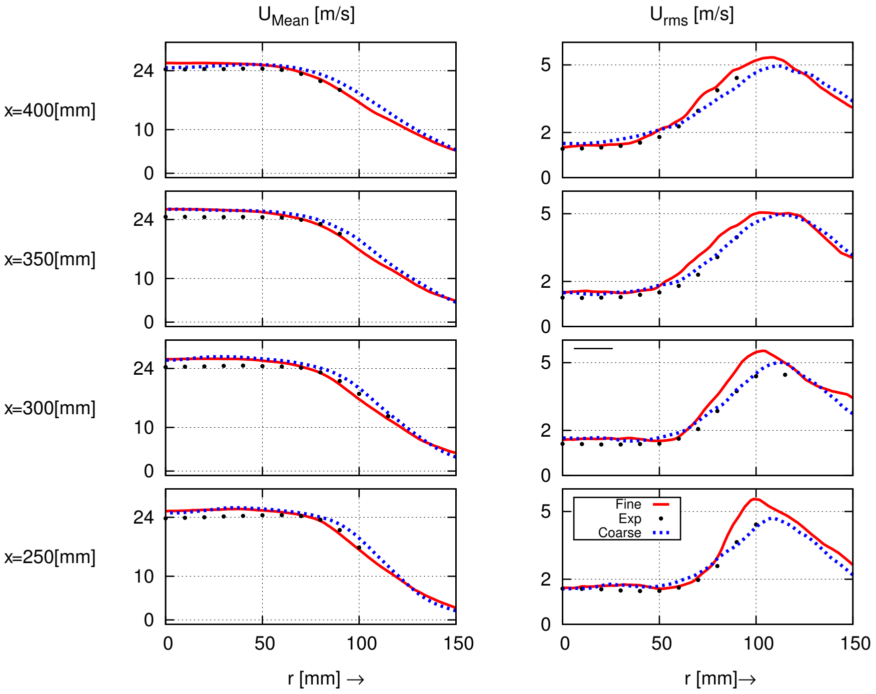

Figure 5.42: Profiles of time averaged axial velocity and the corresponding rms, at 250 : 400 [mm] nozzle downstream positions (Solid line: test case 4b, dotted line: test case 3, symbols: experiment).

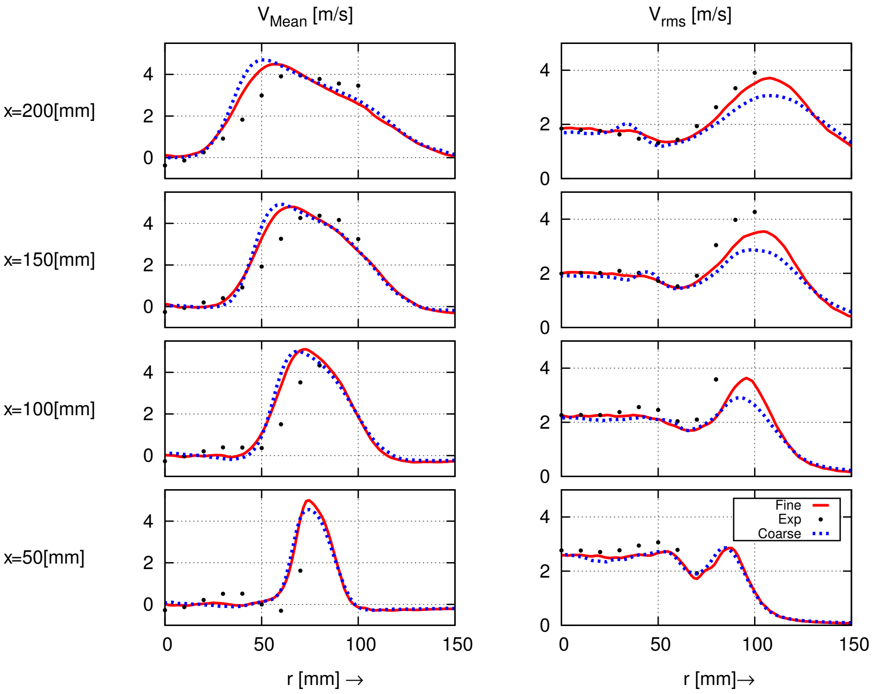

Figure 5.43: Profiles of time averaged radial velocity and the corresponding rms, at 50 : 200 [mm] nozzle downstream positions (Solid line: test case 4b, dotted line: test case 3, symbols: experiment).

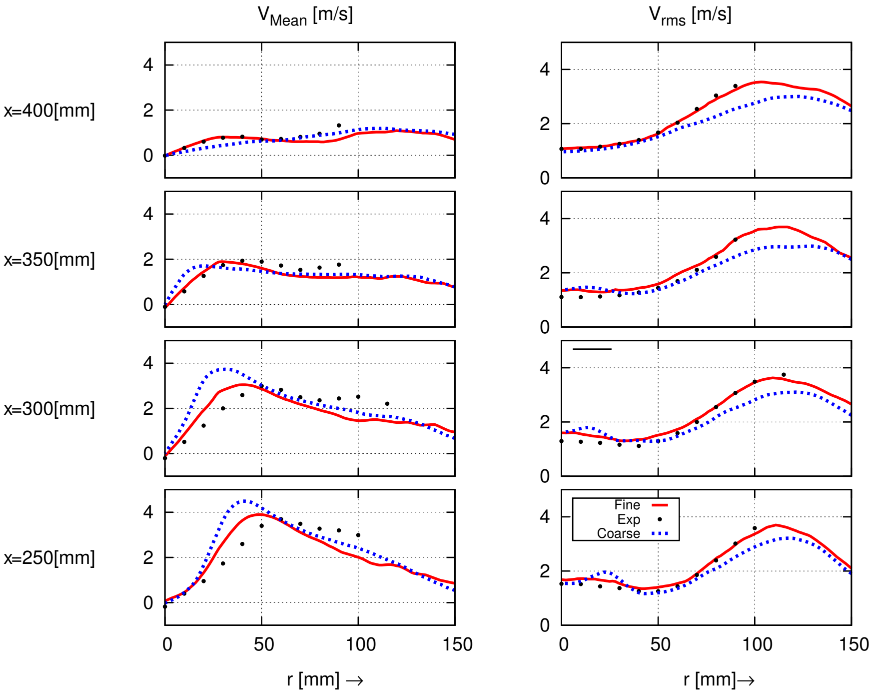

Figure 5.44: Profiles of time averaged radial velocity and the corresponding rms, at 250 : 400 [mm] nozzle downstream positions (Solid line: test case 4b, dotted line: test case 3, symbols: experiment).

4b with each other and experiment shows that despite using different grid resolution the flame height is predicted very well and matching to the experimental data. It shows that wrinkling factor is calculated correctly independent of grid resolution. The comparison of profiles of temperature fluctuation also shows that both simulation could predict the experimental trend. But the fine grid clearly shows better results than the simulation using coarse grid.

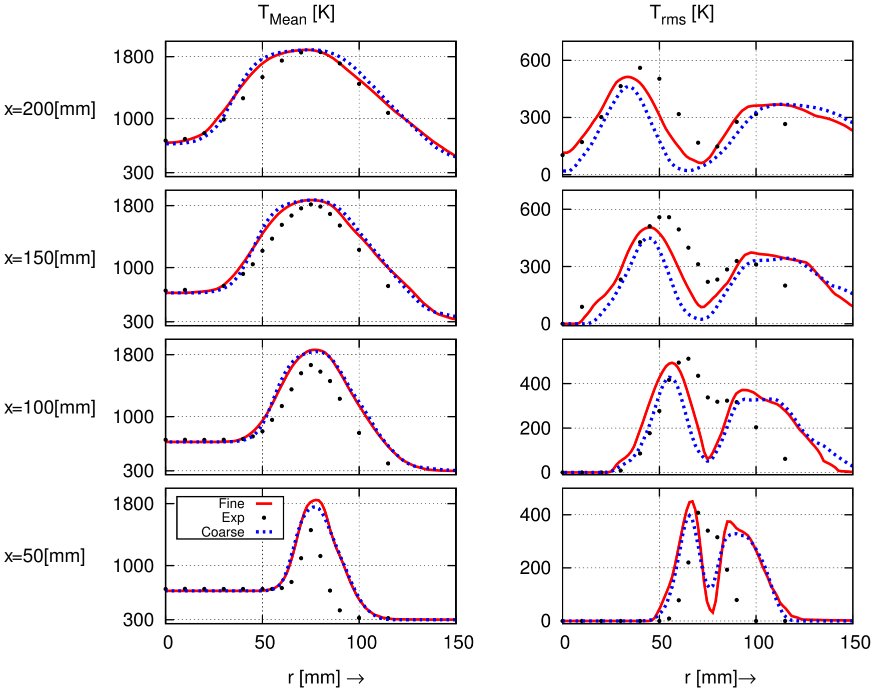

Figure 5.45: Profiles of time averaged temperature and the corresponding rms, at 50 : 200 [mm] nozzle downstream positions (Solid line: test case 4b, dotted line: test case 3, symbols: experiment).

The profiles of averaged subgrid scale wrinkling factor Ξ, thickening F and $\Xi\omega/F$ are depicted in Fig.5.48 and Fig.5.49. In this two configuration the grid is different which causes directly in the different thickening factor, and indirect in the different modeled subgrid scale fluctuation u'_Δ. Fig.5.47 shows a scatter plot of the modeled subgrid scale fluctuation u'_Δ for both grid levels along the nozzle downstream. As expected the finer mesh delivers smaller subgrid scale fluctuation u'_Δ than the coarse mesh.

Despite these differences the flame surface is conserved with a good accuracy. The Fig.5.48 and Fig.5.49 shows that the thickening factor and compensating efficiency function are very different for both cases but the resulting resolved source term has the same order in all plane downstream of the nozzle. The result of this section shows that using the dynamic formulation of the power-law wrinkling model which assures the conservation of the flame surface is adequate for this type of flame. The averaged flow and flame characteristics are matching independent of using the mesh grid and chosen thickening factor.

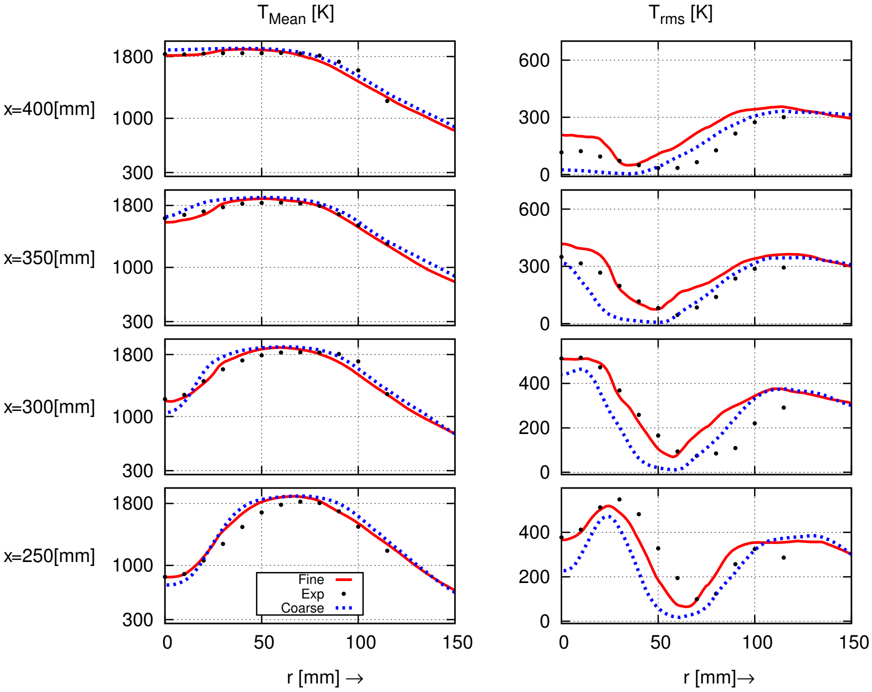

Figure 5.46: Profiles of time averaged temperature and the corresponding rms, at 250 : 400 [mm] nozzle downstream positions (Solid line: test case 4b, dotted line: test case 3, symbols: experiment).

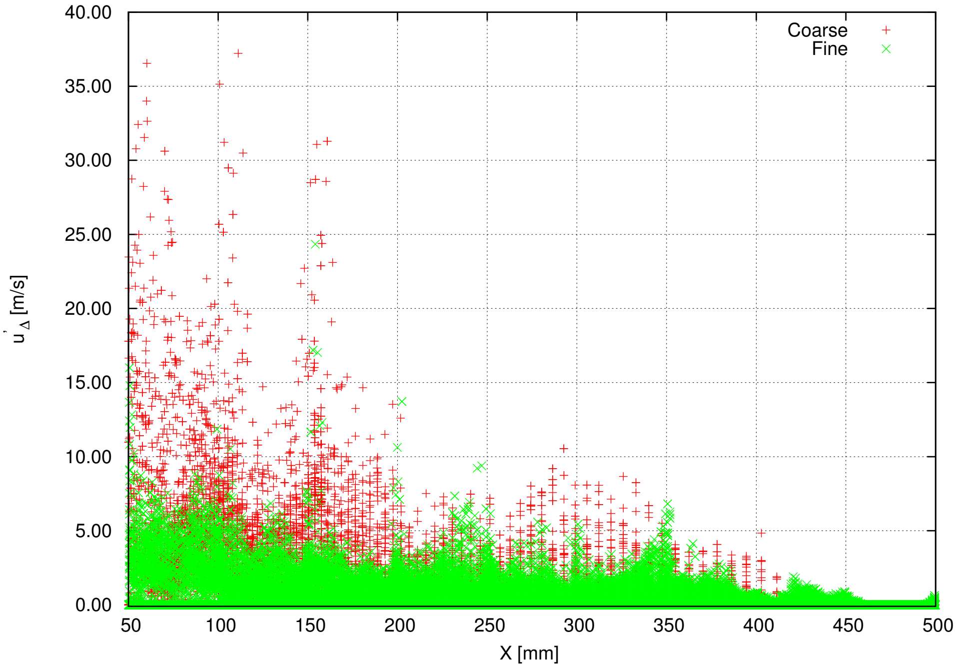

Figure 5.47: The scatter plot of the modeled subgrid scale fluctuation u'_Δ along the nozzle downstream position for the test cases 3 (+++) and test case 4b (× × ×).

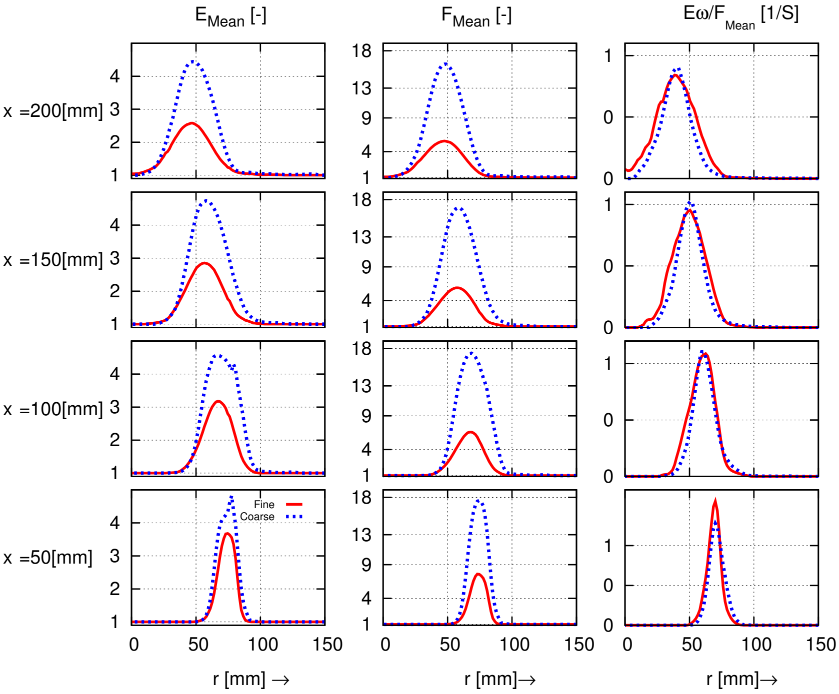

Figure 5.48: Profiles of time averaged E, F and Eω/F, at 50 : 250 [mm] nozzle downstream positions (Solid line: test case 4b, dotted line: test case 3, symbols: experiment).

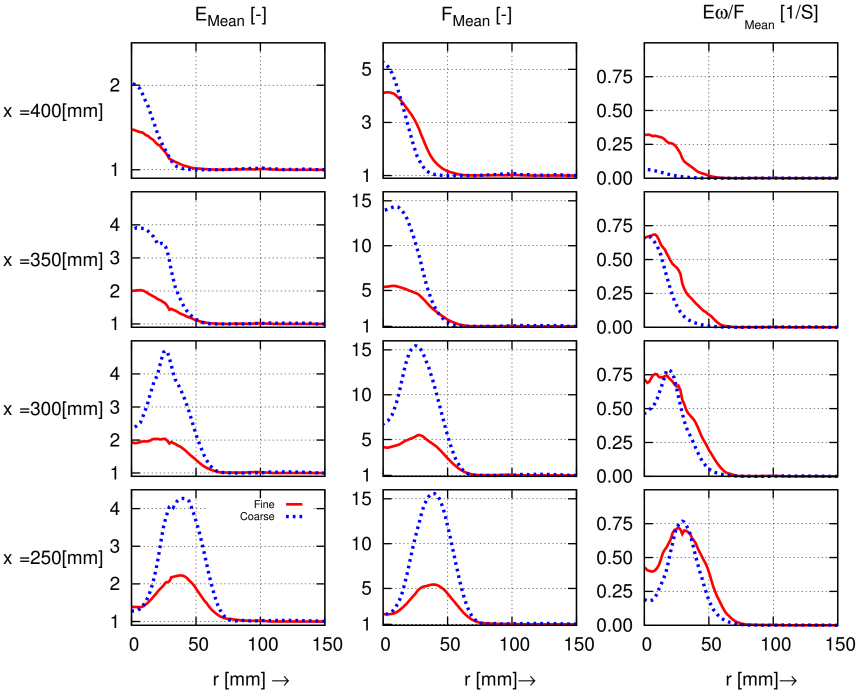

Figure 5.49: Profiles of time averaged E, F and Eω/F, at 50 : 250 [mm] nozzle downstream positions (Solid line: test case 4b, dotted line: test case 3, symbols: experiment).

5.2.6 Investigation of the global/local averaged dynamic power-law wrinkling model

The test case 5 (See Tab.5.3) is conducted with the same boundary conditions and same grid level as the test case 4b (See Tab.5.4). The only difference is using the local averaging method for the β power in the power-law subgrid scale wrinkling model. The local averaging means that, the β power is considered to have spatial and temporal evolution. For this mean, the β is calculated based on the value of certain amount of neighbor cells. In this study the β power is only considered to have axial spatial dependency.

Fig.5.50 shows the evolution of the 1-D β values along the downstream position of the nozzle. The mean power value decreases from $\beta = 0.75$ at nozzle downstream $x = 0.0$ $[mm]$ down to $\beta \approx 0.59$ at $x \approx 400$ $[mm]$. At the flame tip the β power value increases rapidly which is close to the same value for the nozzle exit. This jump is related to the detached pockets which have very small flame surfaces. The rms of the β is constant in the main flame area and has a jump at flame tip, indicating the high interval of the detached flame pocket formation.

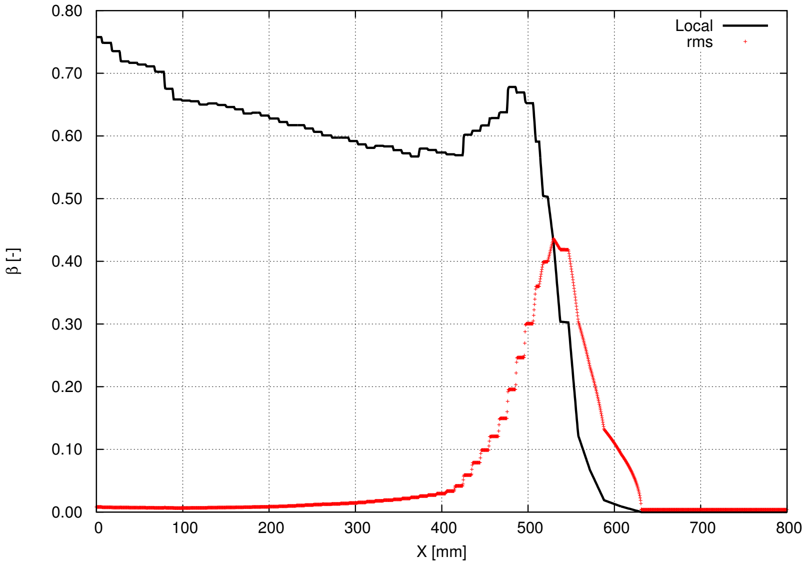

Figure 5.50: 1-D local averaged β values along the nozzle downstream for the test case 5. Mean value β_m(—), rms β_{rms} (+++).

The Fig.5.51 and Fig.5.52 show the profiles of averaged axial velocity and corresponding rms for the planes 50 : 400 [mm] nozzle downstream for test case 5 and test case 4b. The overall results show very good agreement with the experimental results for both test cases.

The profiles of the time averaged radial velocity and the corresponding fluctuations for the planes 50 : 400 [mm] nozzle downstream are depicted in Fig.5.53 and Fig.5.54. The comparison shows that for all planes downstream of the nozzle, the result of both test cases are in an very good agreement with the experiment.

The profiles of the time averaged temperature and corresponding fluctuations for the planes 50 : 400 [mm] nozzle downstream are depicted in Fig.5.55 and Fig.5.56 for the test case 4b and 6. The comparison with the experiment shows that the results of both test cases are in agreement with experiment. The both simulations are also in very good

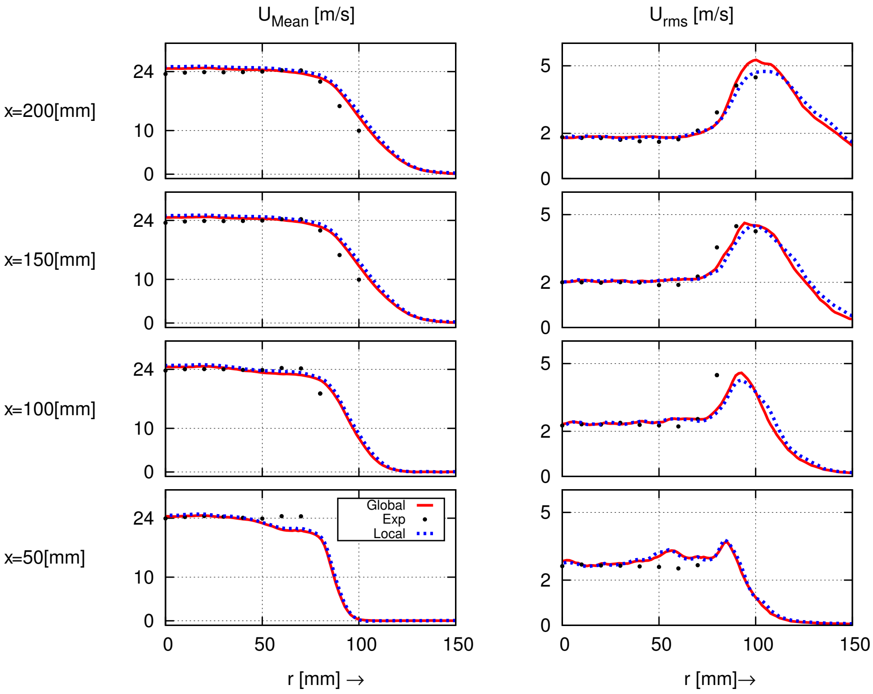

Figure 5.51: Profiles of time averaged axial velocity and the corresponding rms, at 50 : 200 [mm] nozzle downstream positions (Solid line: test case 4b, dotted line: test case 5, symbols: experiment).

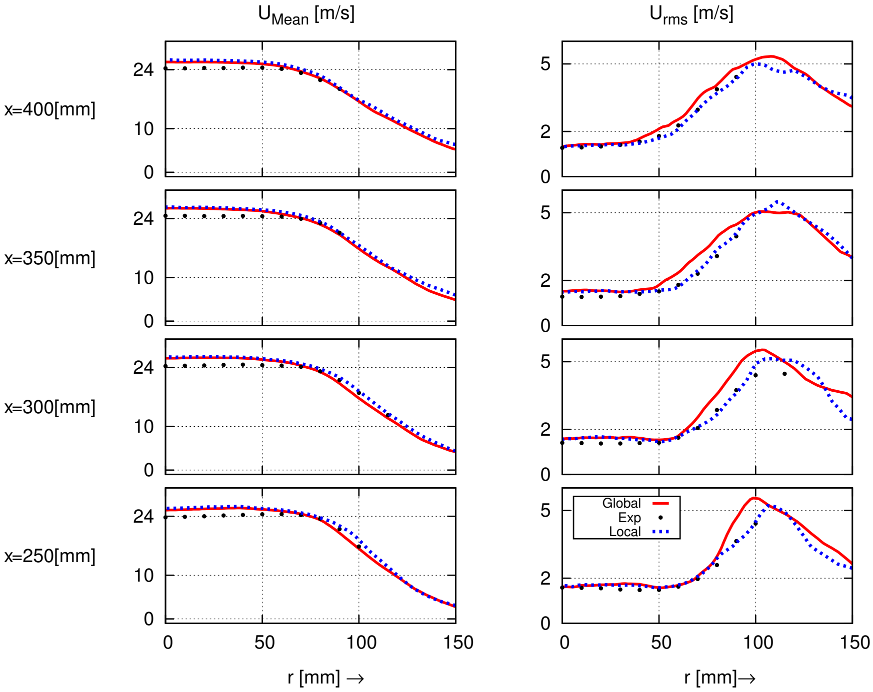

Figure 5.52: Profiles of time averaged axial velocity and the corresponding rms, at 250 : 400 [mm] nozzle downstream positions (Solid line: test case 4b, dotted line: test case 5, symbols: experiment)

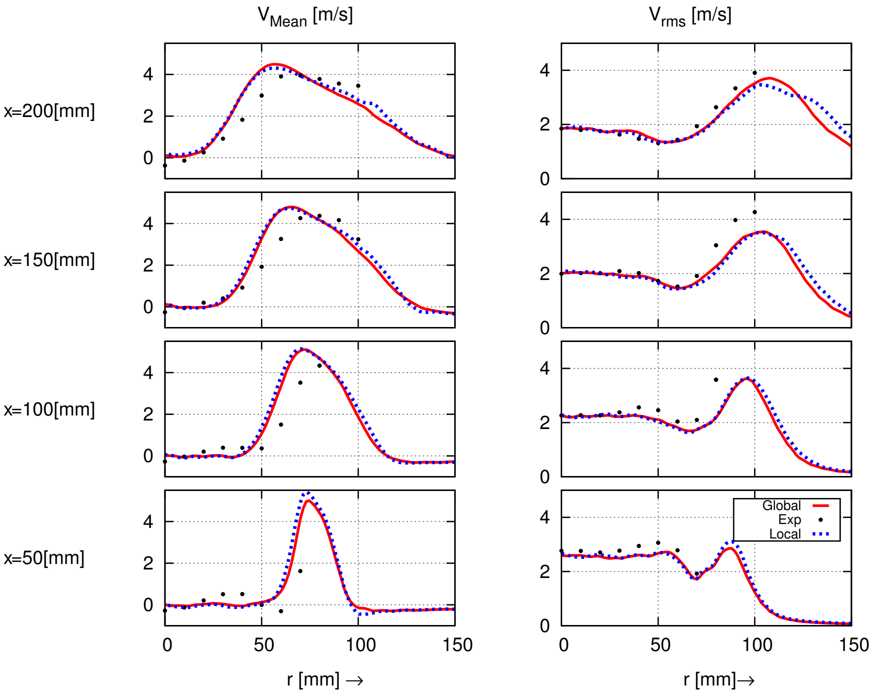

Figure 5.53: Profiles of time averaged radial velocity and the corresponding rms, at 50 : 200 [mm] nozzle downstream positions (Solid line: test case 4b, dotted line: test case 5, symbols: experiment).

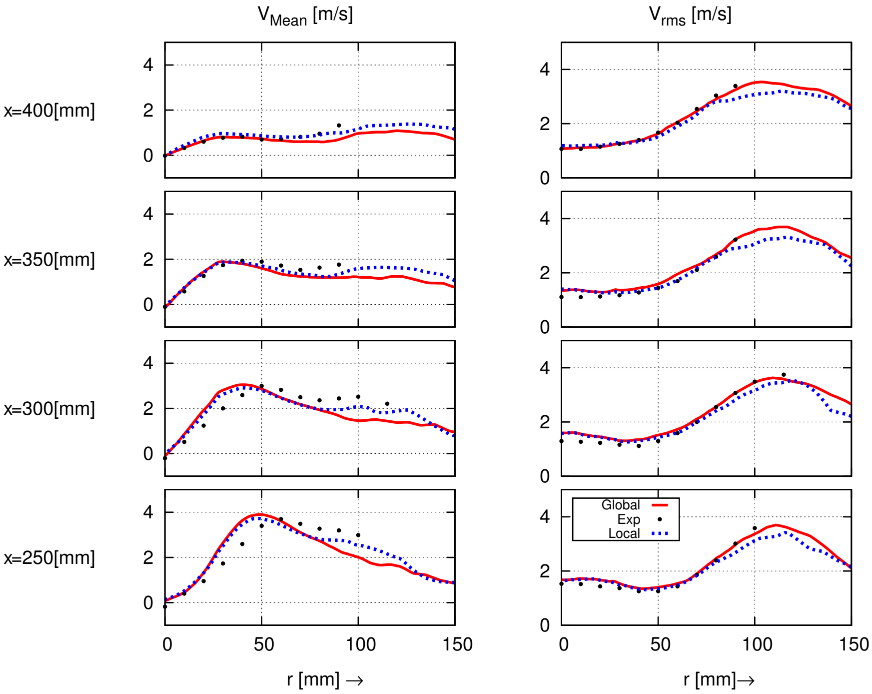

Figure 5.54: Profiles of time averaged radial velocity and the corresponding rms, at 250 : 400 [mm] nozzle downstream positions (Solid line: test case 4b, dotted line: test case 5, symbols: experiment)

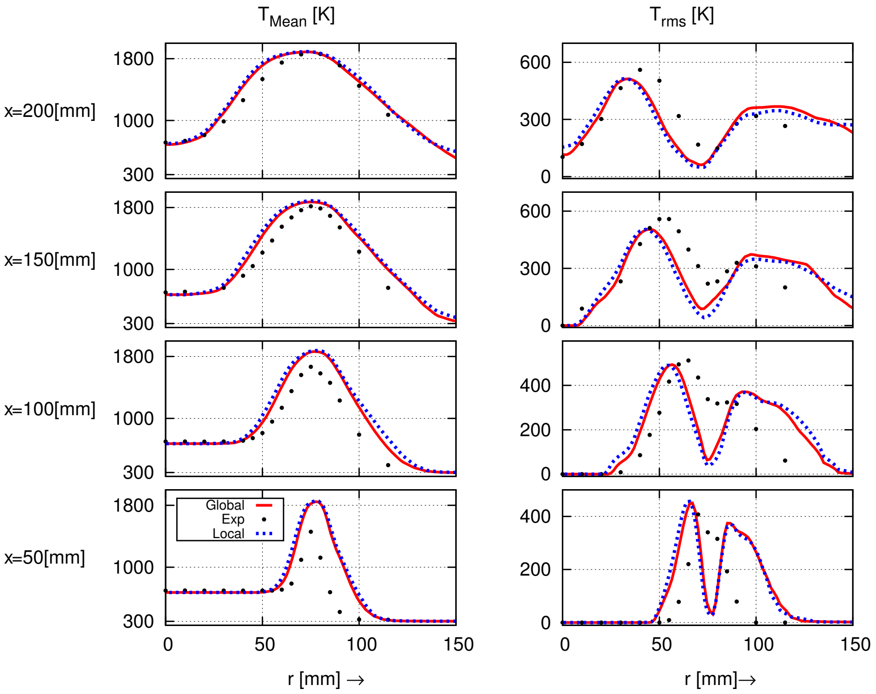

Figure 5.55: Profiles of time averaged temperature and the corresponding rms, at 50 : 200 [mm] nozzle downstream positions (Solid line: test case 4b, dotted line: test case 5, symbols: experiment).

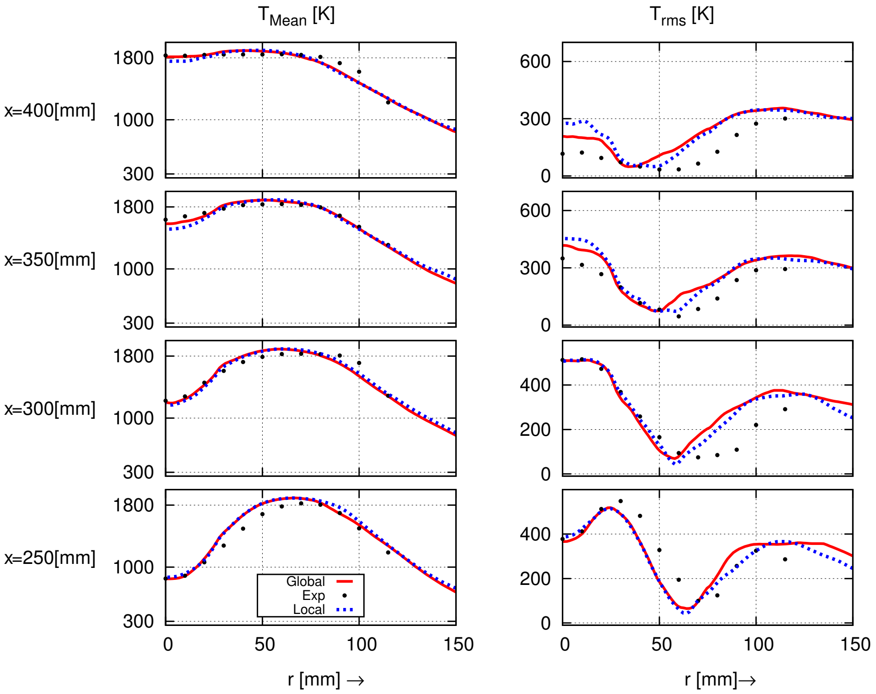

Figure 5.56: Profiles of time averaged temperature and the corresponding rms, at 250 : 400 [mm] nozzle downstream positions (Solid line: test case 4b, dotted line: test case 5, symbols: experiment).

agreement with the experimental data. The comparison of the simulations using local and global averaged β shows that the assumption of a uniform power for the whole combustion domain is adequate for the current configuration.

In the current section the LES (Large Eddy Simulation) of the matrix burner configuration using ATF (Artificially Thickened Flame) combustion model and different wrinkling models have been presented. The Simulation results reveals that despite using different grid level and consequently different resolutions, the simulations using dynamic formulation of the wrinkling model could deliver correct flame characteristics. Hence, the simulations using linear wrinkling model or non-dynamic version of the power-law wrinkling model fail to predict the correct flame and flow characteristics. The utilization of local or global averaging methods also has no major influence on the overall flame characteristics prediction. Therefore the global averaging method seems to have sufficient accuracy.

In the next section the simulation results of the same configuration using a F-TACLES (Filtered TAbulated Chemistry for LES) coupled with the power-law wrinkling model will be reviewed and discussed. The aim is to investigate the combustion model dependency of the wrinkling model.

5.3 Numerical investigation using F-TACLES combustion model

In the second part of this chapter the numerical investigation results of matrix burner using F-TACLES combustion model [13], [14] will be reviewed. In this section four different test cases are simulated using F-TACLES combustion model and different wrinkling models. The wrinkling models used in this section consist of the power-law model of charlette et al. in both non-dynamic [12] and dynamic form [19]. The simulations which are investigated with dynamic version of power-law wrinkling model [19] are also conducted using tow grid levels [115].

5.3.1 Investigation of the non-dynamic power-law wrinkling model using the coarse gird

Different simulations are conducted using two grid levels, a coarse grid with $\Delta_x \approx 2$ [mm] and a finer grid with $\Delta_x \approx 1$ [mm] using uniform mesh spacing in the interested zone. The first set of simulations is carried out on the coarse gird with non-dynamic formulation of the power-law wrinkling model to check the prediction accuracy of the power-law wrinkling model and its sensitivity to different values of β power parameter used for non-dynamic approach.

The boundary conditions are the same for all simulations. The only difference is the values of exponent β in Eq.4.20. The values of β are 0.3 and 0.5 for the conducted simulations.

Fig.5.57 shows the qualitative comparison of contour plots of averaged resolved temperature for the simulations with a non-dynamic model and different values of the power-law exponent using coarse grid. Fig.5.57 shows that the flame shape is obviously different for both cases, showing different computed turbulent flame velocities. First, the flame height is different and higher in case of $\beta = 0.3$ and, second, the early stages of the resolved flames are also different, one is not fully resolved ($\beta = 0.3$) and the other is over resolved ($\beta = 0.5$).

This shows that, using the same combustion model, boundary conditions and mesh grid, the resolved temperature field can be obviously different using different wrinkling factors.

Fig.5.58 shows the radial profiles of averaged axial velocity and their corresponding rms for the planes 50:200 [mm] nozzle downstream. The comparison shows that both simulations could predict the velocity profiles and their averaged fluctuation correctly in axial direction. The same behavior is observed in Fig.5.59 for the axial velocity in planes 250:400 [mm] downstream of the nozzle. It is shown that the velocity in axial direction is not dependent on the combustion.

The profiles of radial velocity are depicted in Fig.5.60. The radial velocity is in a non-reacting jet flame always zero, a result of axisymmetric behavior of the jet. In reacting jets the radial velocity is perpendicular to the flame front and is a measure of the flame dynamic. The comparison to the experiment shows that the simulation using $\beta = 0.5$ is overestimating the radial velocities in planes 50:250 [mm] above the nozzle. The opposite behavior can be observed in Fig.5.61 for planes 300:400 [mm] nozzle downstream. It is

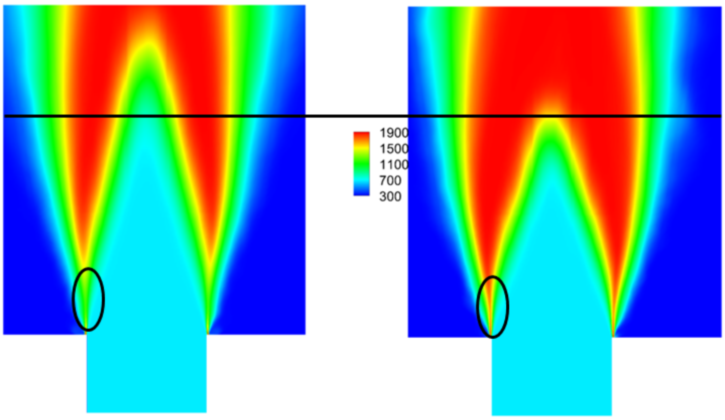

Figure 5.57: Contour plots of averaged temperature [K] left $\beta = 0.3$ and right with $\beta = 0.5$ for the test case 7.

demonstrated that using a $\beta = 0.5$ results in a very high turbulent flame velocity and consequently in a higher slope of the jet flame.

The comparison of the statistical result of radial profiles of radial velocity of the test case using the lower value $\beta = 0.3$ shows good agreement in planes 50:250 [mm] but overestimates the radial velocity in planes 300:400 [mm] above the nozzle. The later overestimation is a result of a lower predicted turbulence flame velocity and corresponding higher flame height. These comparisons show that the correct prediction of the turbulent flame velocity is very dependent on a correct prediction of wrinkling factor. On the other hand, the correct prediction of the wrinkling factor seems to be strictly dependent on the right value of β prediction.

The comparison of planes 50:200 [mm] nozzle downstream with the experiment shows that simulations deliver very different behavior (see also Fig.5.57). The simulation using $\beta = 0.3$ underestimate the maximum temperature in plane 50 [mm] nozzle downstream of 500 [K]. The profiles of the averaged temperature are thinner than the experiment shows, and are shifted to the right side. In all other planes 100:400 [mm] the same behavior is repeated.

The quantitative comparison of the averaged radial profiles of temperature for the test case using $\beta = 0.5$ with the experiment shows overestimation in all planes downstream of the nozzle. The temperature profile is much thicker than the experiment and the flame height is very low as depicted in Fig.5.57.

The quantitative comparison of different planes downstream of the nozzle with the experiment shows that none of the above simulations are able to predict the correct flame characteristics as a result of a wrong turbulent flame velocity approximation. Consequently it is shown that the assumption of a fixed exponent in power-law wrinkling model is not justified in this configuration.

The same simulations using a finer grid and non-dynamic version of the power-law wrinkling model are investigated (not shown here). They provided the same results . None of the simulations could correctly predict the flow and the flame characteristics using such fixed values for β.

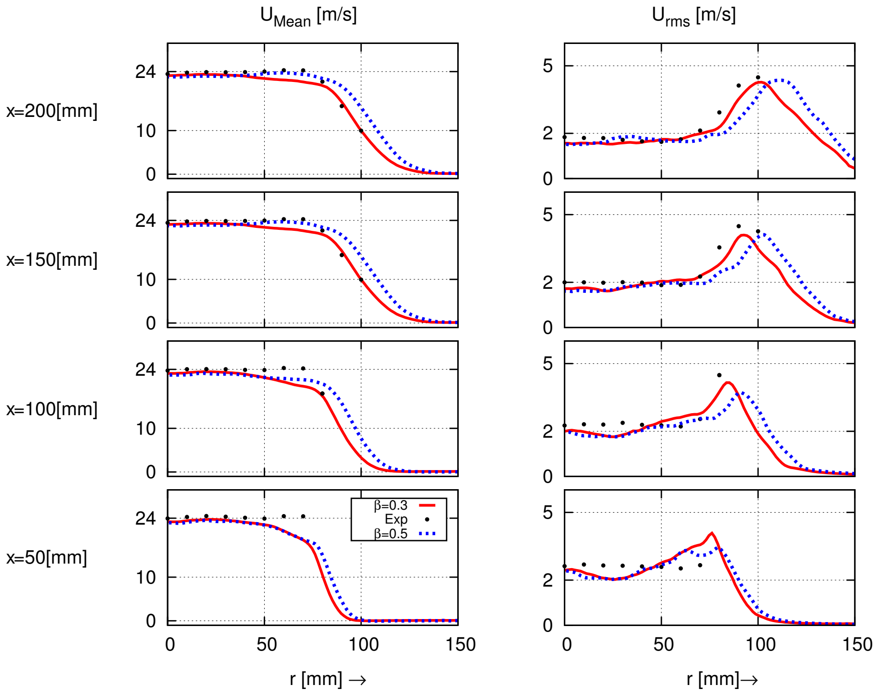

Figure 5.58: Profiles of time averaged axial velocity and the corresponding rms, at 50 : 200 [mm] nozzle downstream positions for the test case 7 (Solid line: β=0.3, dotted line: β=0.5, symbols: experiment).

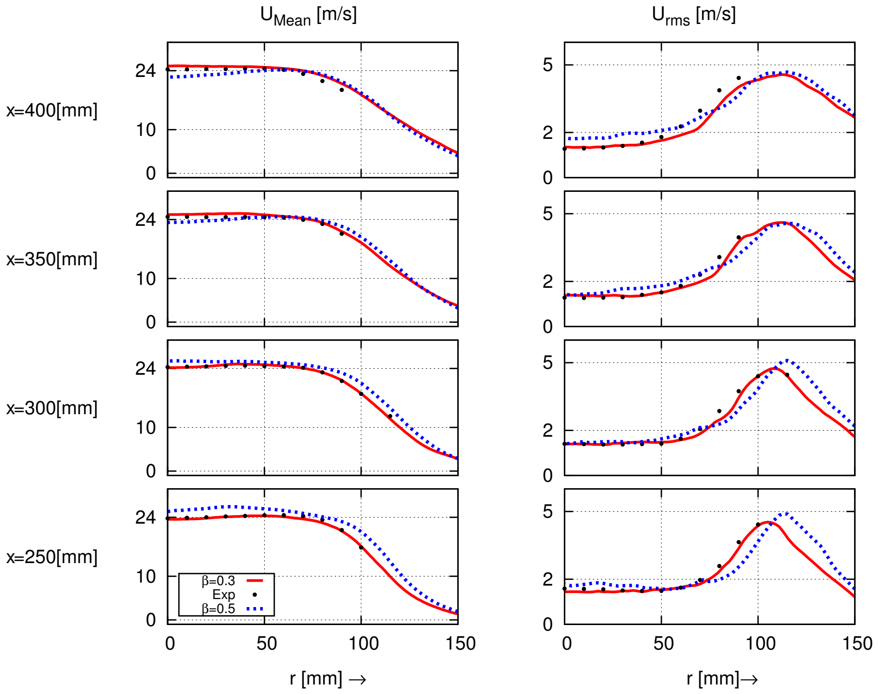

Figure 5.59: Profiles of time averaged axial velocity and the corresponding rms, at 250 : 400 [mm] nozzle downstream positions for the test case 7 (Solid line: β=0.3, dotted line: β=0.5, symbols: experiment).

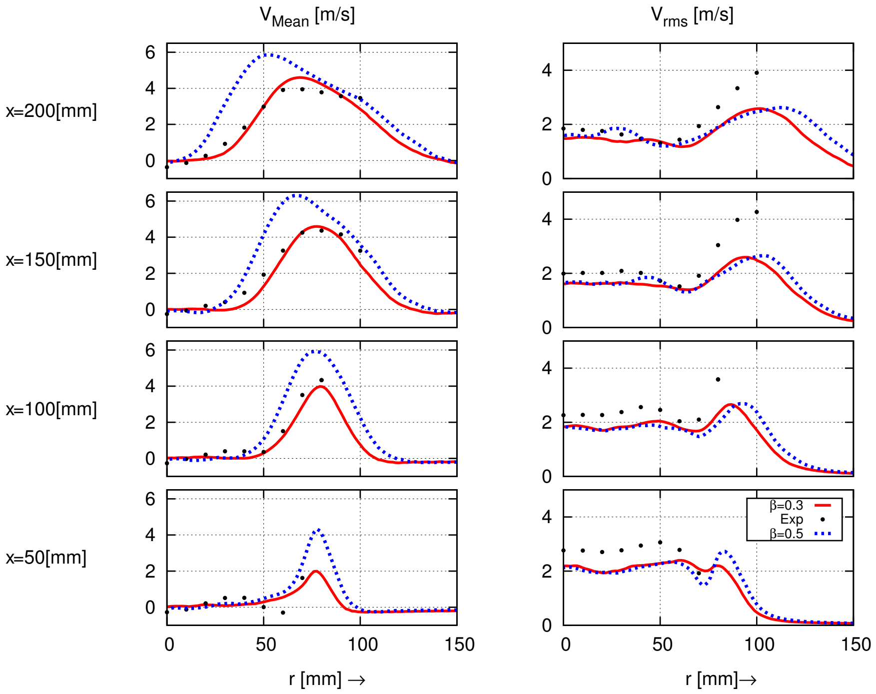

Figure 5.60: Profiles of time averaged radial velocity and the corresponding rms, at 50 : 200 [mm] nozzle downstream positions for the test case 7 (Solid line: β=0.3, dotted line: β=0.5, symbols: experiment).

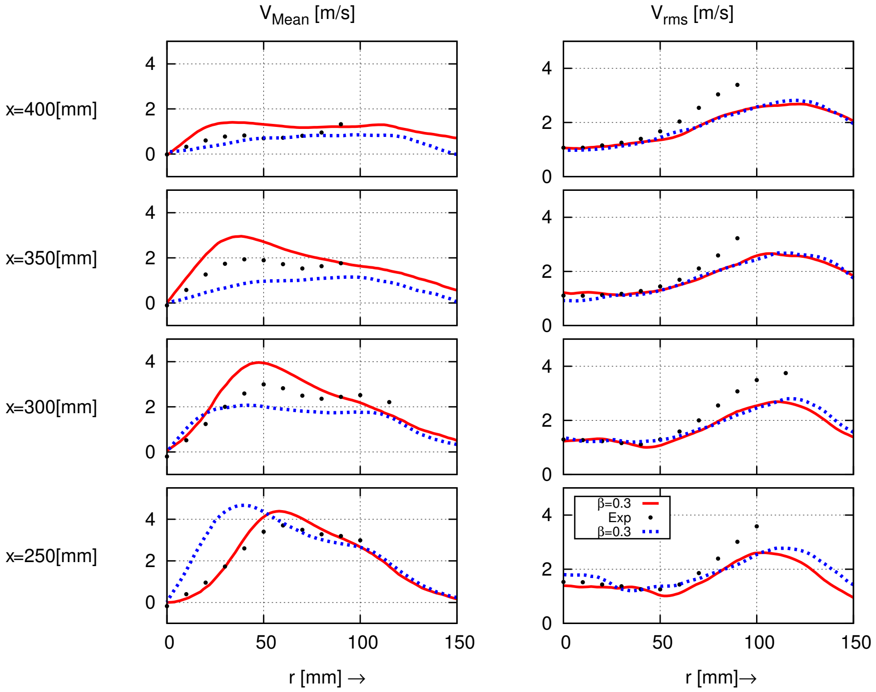

Figure 5.61: Profiles of time averaged radial velocity and the corresponding rms, at 250 : 400 [mm] nozzle downstream positions for the test case 7 (Solid line: β=0.3, dotted line: β=0.5, symbols: experiment).

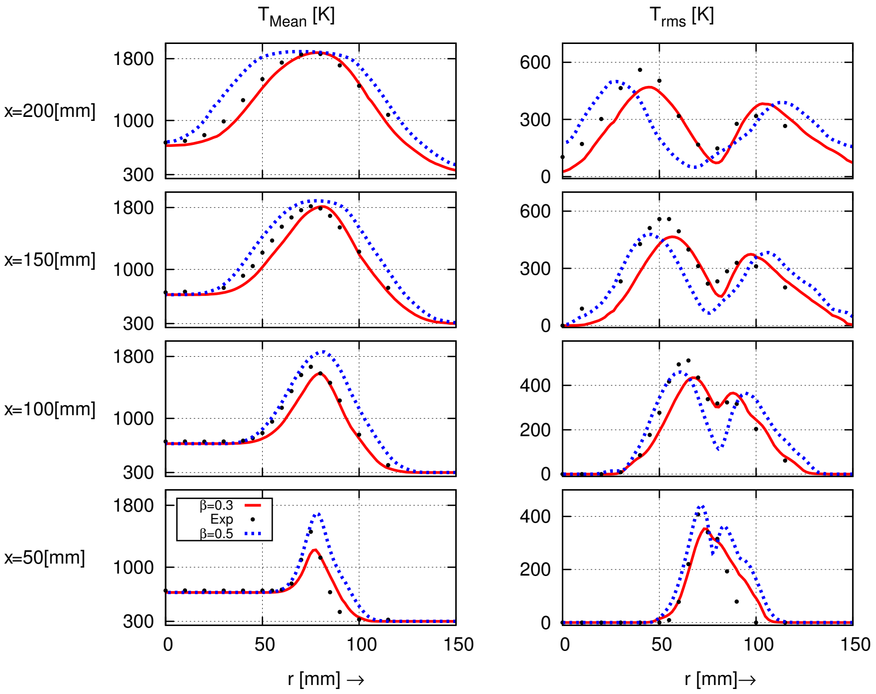

Figure 5.62: Profiles of time averaged temperature and the corresponding rms, at 50 : 200 [mm] nozzle downstream positions for the test case 7 (Solid line: β=0.3, dotted line: β=0.5, symbols: experiment).

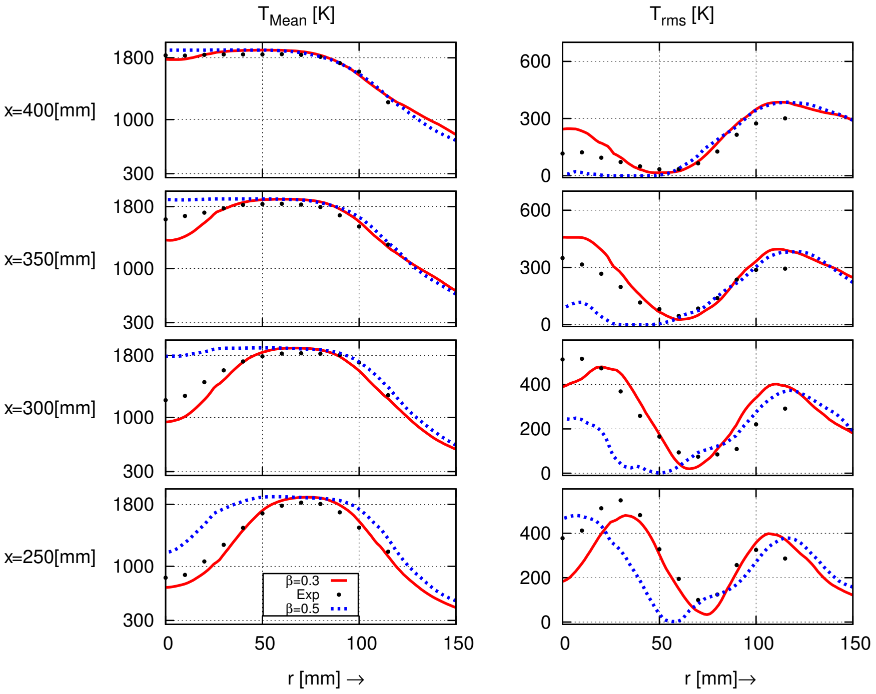

Figure 5.63: Profiles of time averaged temperature and the corresponding rms, at 250 : 400 [mm] nozzle downstream positions for the test case 7 (Solid line: β=0.3, dotted line: β=0.5, symbols: experiment).

5.3.2 Investigation of the dynamic power-law wrinkling model using the coarse and fine grid

The other set of simulations is carried out using the dynamic formulation of the power-law wrinkling model [23] on both grid levels. The power-law exponent is averaged over whole domain and holds as a single constant which has only temporal evolution.

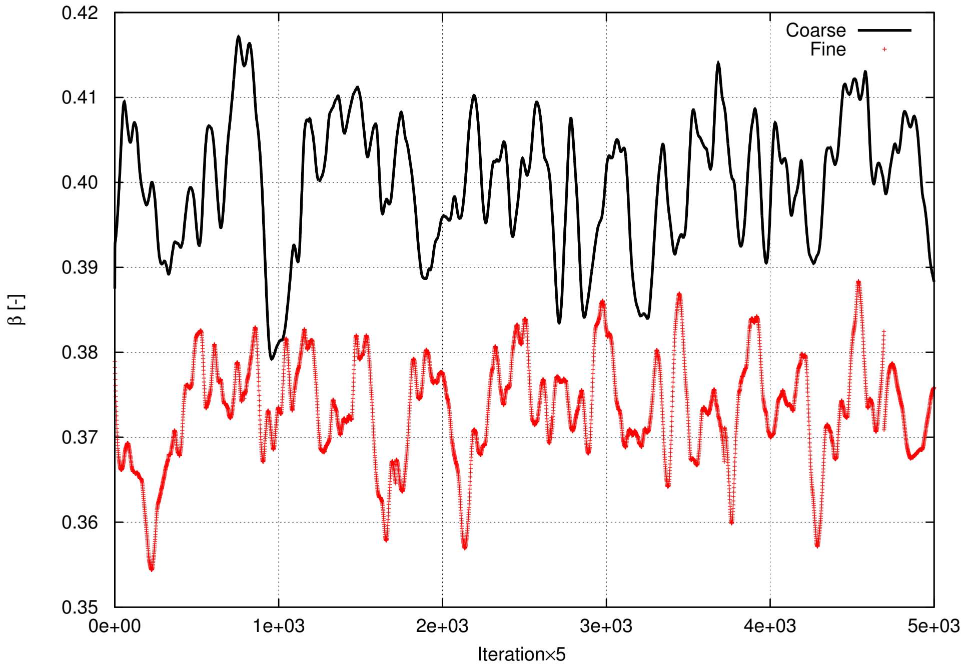

Figure 5.64: The temporal evolution of the β power averaged over whole domain for the test cases 8 (− −) and test case 9 (+++)

Fig.5.64 shows the temporal evolution of the global averaged power-law exponent β for both grid levels. The β exponent varies from a minimum value 0.38 to a maximum 0.415 and has an average of 0.399 for the coarse mesh. For the fine mesh the β exponent changes from minimum 0.355 to maximum 0.39 and has an average of 0.374. The peaks in the temporal evolution of the power-law exponent are related to the detached packet at the flame tip with corresponding very low flame surface as can be observed in Fig.5.65

The filtering and averaging procedure is conducted and updated the β exponent every five time steps. The dynamic simulations show that the exponent β has a temporal evolution and cannot be held as an universal constant.

Fig.5.65 shows the contour plots of averaged temperature superimposed with the progress variable source term. It shows clearly that the simulation conducted with fine grid can resolve the small scales of the turbulent flow. In opposite, the coarse grid can only resolve large scale turbulence.

The dynamic wrinkling model assures the conservation of the flame surface. As a result, comparison of statistical averaged data shows that using dynamic formulation of the power-law wrinkling model delivers similar results for both grid levels despite the demonstrated different resolved flame structure.

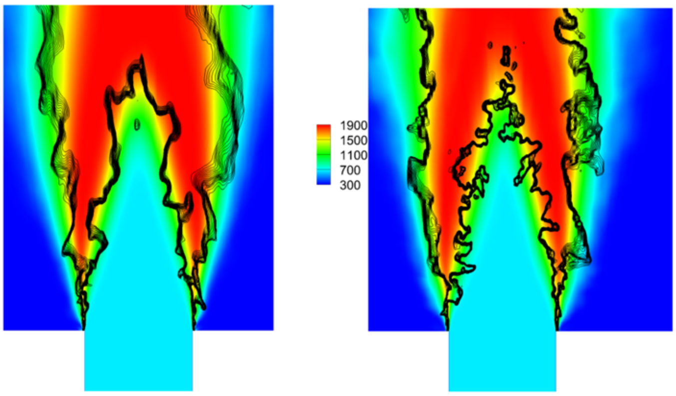

Figure 5.65: Counter plots of averaged temperature superimposed with profiles of progress variable source term. Left: test case 8, right: test case 9.

Fig.5.66 shows the radial profiles of time averaged axial velocity and their corresponding rms for the planes 50:200 [mm] nozzle downstream for both grid levels. The comparison shows that both grid levels could predict the axial velocity profiles and their averaged fluctuation correctly. Just as expected the finer grid can better resolve the rms of this velocity component than the coarse grid does. The same behavior is observed in Fig.5.67 for the axial velocity in planes 250:400 [mm] downstream of the nozzle.

The profiles of radial velocity are illustrated in Fig.5.68 and Fig.5.69 for simulations on both grid levels. The results show improvement in comparison to the non-dynamic simulations. The overall radial velocity profile shows that the fine grid achieves a better flame dynamic due to better resolution of the flame and turbulence interaction. The profiles of radial velocity fluctuation for the fine grid are in better agreement with the experiment as expected.

Fig.5.70 and Fig.5.71 show the radial profiles of the time averaged temperature and temperature fluctuation on both grid levels. The calculated averaged temperature is in excellent agreement with experiment. Despite different resolutions, the predicted averaged modeled reaction rate and corresponding temperature seems to be conservative in all planes (see also Fig.5.65).

The profiles of temperature fluctuation show also a good agreement between experiment and simulations for both grid levels while the finer grid provides superior achievement.

The numerical investigation show that the non-dynamic model with constant values of exponent β is not able to predict the correct turbulent burning velocity, and consequently, the flame characteristics. The statistical results with a dynamically determined model parameter are very encouraging and allow for very good predictions.

The results show that the value of the beta exponent is case dependent and cannot be held as a fixed general value for all different configurations. Therefore the utilization of a dynamic formulation of the power-law wrinkling model is inevitable for a correct prediction of the turbulent burning velocity.

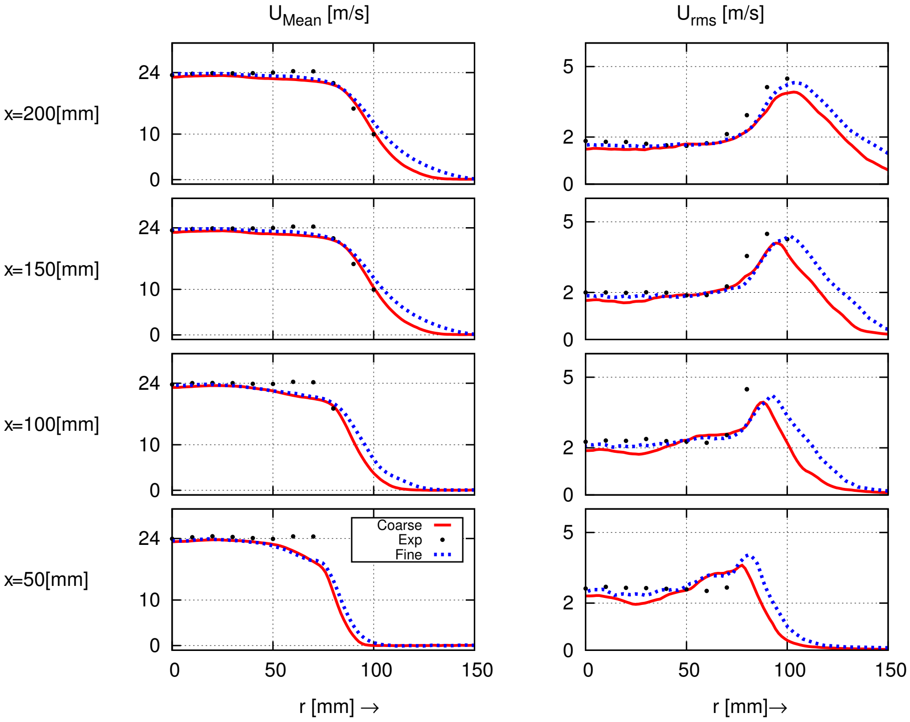

Figure 5.66: Profiles of time averaged axial velocity and the corresponding rms, at 50 : 200 [mm] nozzle downstream positions (Solid line: test case 8, dotted line: test case 9, symbols: experiment).

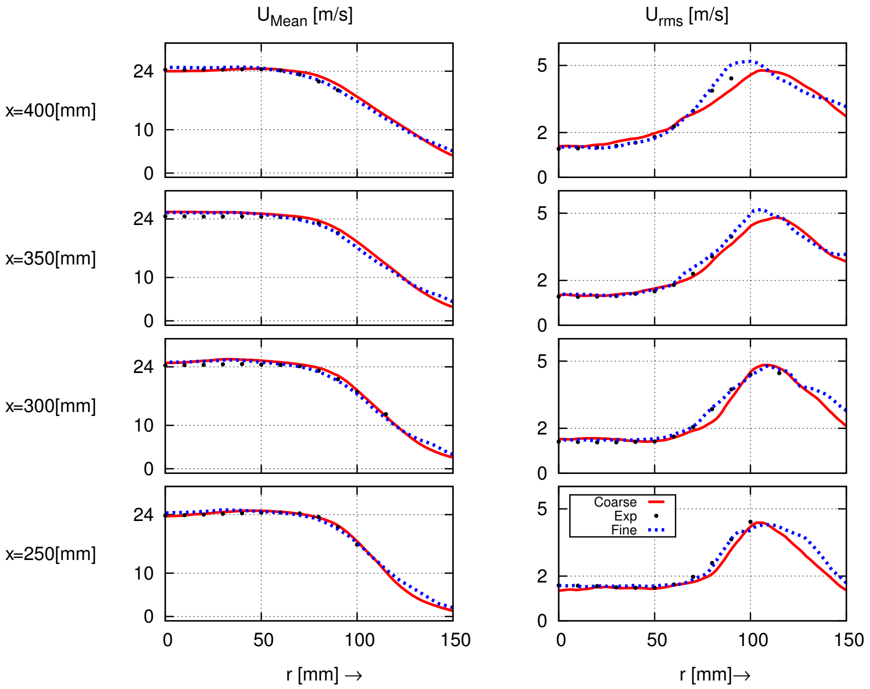

Figure 5.67: Profiles of time averaged axial velocity and the corresponding rms, at 250 : 400 [mm] nozzle downstream positions (Solid line: test case 8, dotted line: test case 9, symbols: experiment).

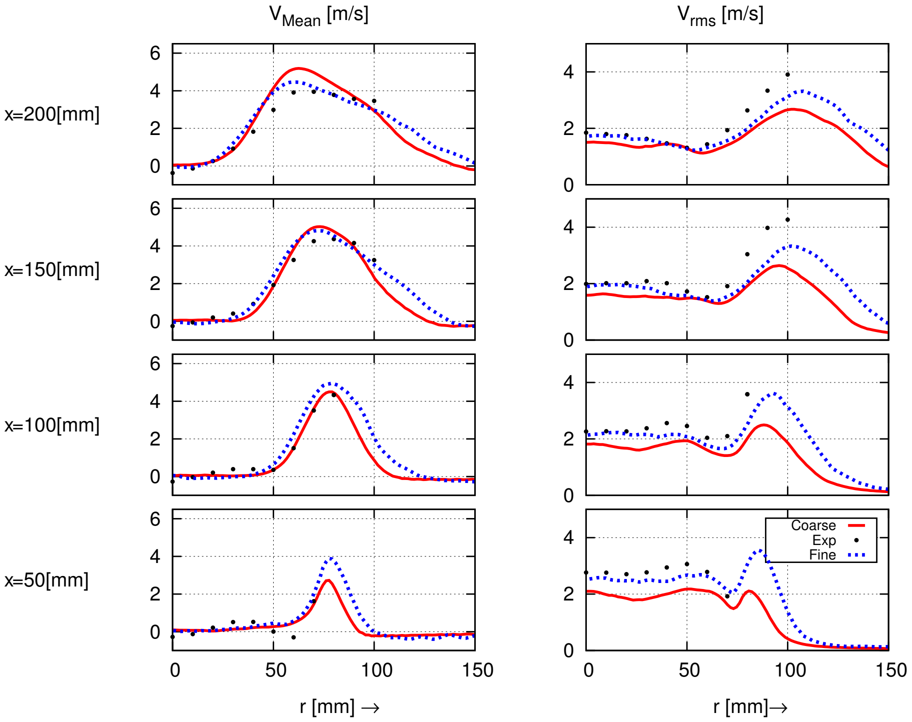

Figure 5.68: Profiles of time averaged radial velocity and the corresponding rms, at 50 : 200 [mm] nozzle downstream positions (Solid line: test case 8, dotted line: test case 9, symbols: experiment).

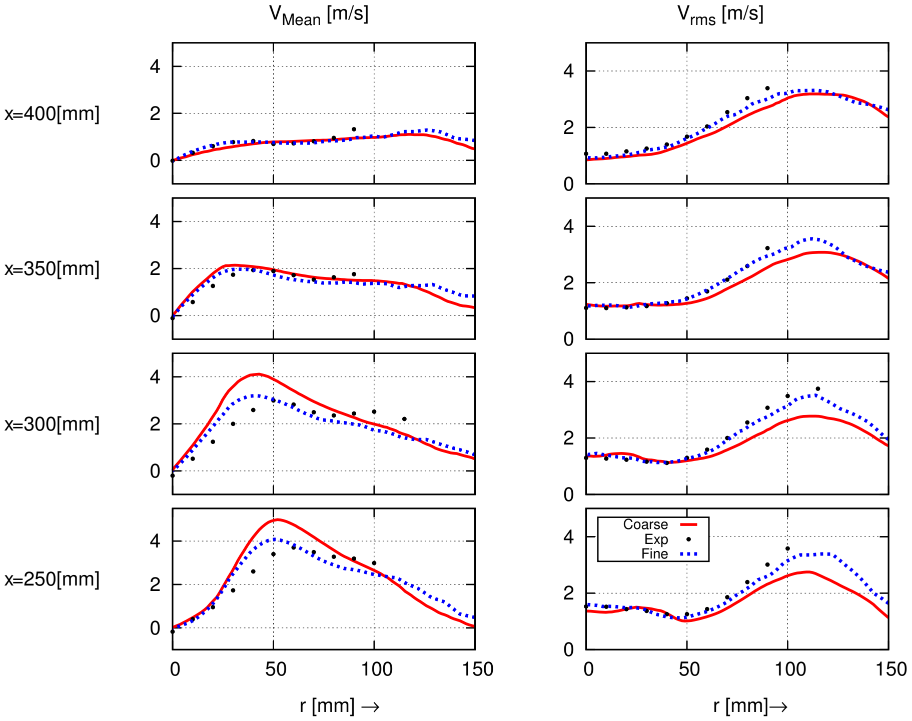

Figure 5.69: Profiles of time averaged radial velocity and the corresponding rms, at 250 : 400 [mm] nozzle downstream positions (Solid line: test case 8, dotted line: test case 9, symbols: experiment).

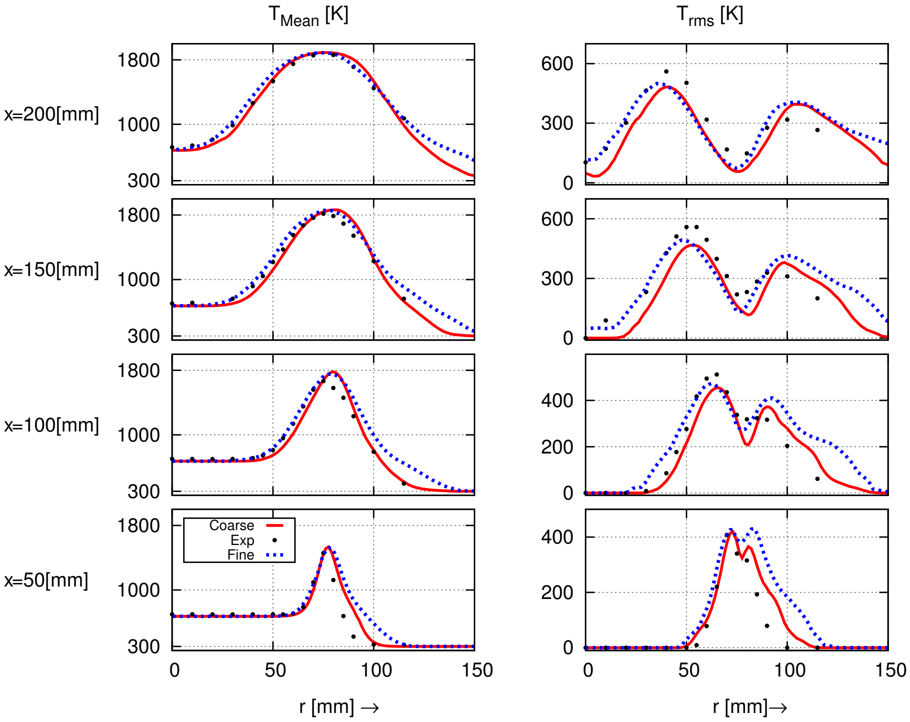

Figure 5.70: Profiles of time averaged temperature and the corresponding rms, at 50 : 200 [mm] nozzle downstream positions (Solid line: test case 8, dotted line: test case 9, symbols: experiment).

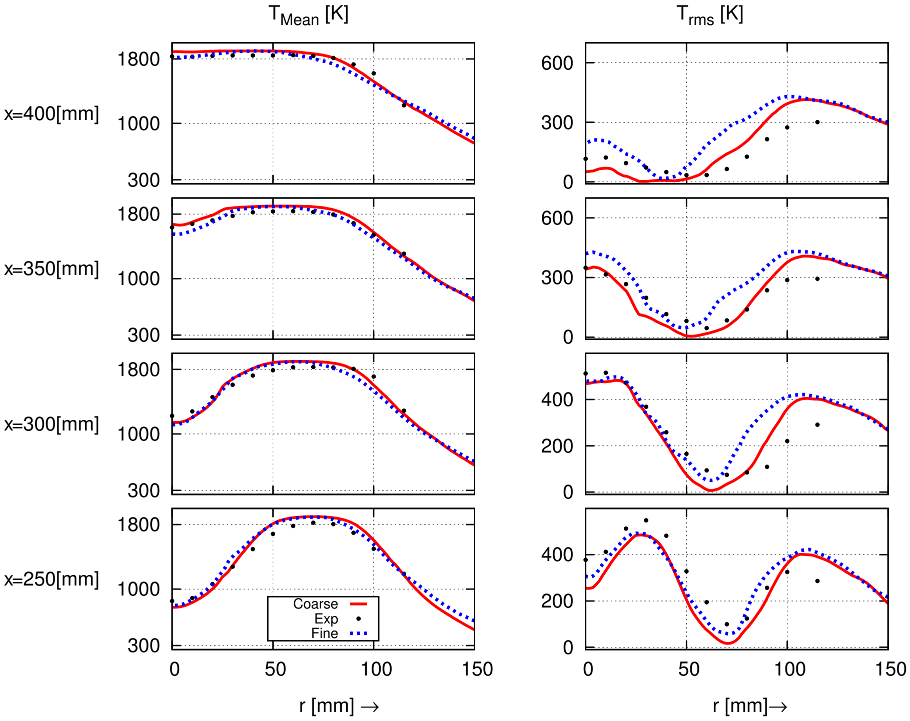

Figure 5.71: Profiles of time averaged temperature and the corresponding rms, at 250 : 400 [mm] nozzle downstream positions (Solid line: test case 8, dotted line: test case 9, symbols: experiment).

5.4 Conclusions

In this chapter the simulation results of a lean premixed Bunsen type flame (Matrix Burner) (Sec.5.1.0.4) with high turbulent intensity on two grid levels are presented. The simulations are conducted using the ATF (Artificially Thickened Flame) (Sec.5.2) and F-TACLES (Filtered TAbulated Chemistry for LES)(Sec.5.3) combustion approaches. Both combustion models are coupled with the different wrinkling models.

The simulation results in comparison to the experiment show that only the simulations using dynamic formulation of power-law wrinkling model could predict the flame and flow characteristics, independent of the combustion model and grid level.

The averaging procedure of the power-law exponent in the dynamic model is considered to have just temporal or both temporal and spatial dependency. The conducted simulations using both averaging methods show same results in the averaged statistical comparison. Therefore the global averaging seems to be sufficient for this type of comparison.

Chapter 6

Application: Berlin burner

A generic Bunsen type burner was designed and experimentally investigated in the Technische Universität Berlin [116], [117]. The burner is designed to exclusively study the impact of different preheating temperatures and different momentum on the formation of combustion induced noise [118]. The burner design should exclude any other environmental or flow effects on the combustion induced noise rather than the altered preheating temperature or momentum. The result of the averaged momentum of the flow and the flame dynamics are compared with the experiment and the results of the ATF and the F-TACLES combustion models both coupled with power-law wrinkling model in non-dynamic and dynamic form.

6.1 Experimental and numerical setup

6.1.0.1 Experimental setup

The generic designed configuration is characterized by its simple construction. Fig.6.1 shows the experimental setup of the Berlin burner. It begins with the downstream mixing tap from the main air, methane and optionally including the seeding particles stream (1). This leads to a annular injection of the pre-mixed methane-air mixture (2). From there, the mixture will be homogenized in the settling chamber (3) and the quartz glass (4) and flows in to the convergent nozzle (outlet diameter d = 35 mm, (5)), concluding with the burner plate (6). The nozzle produces a block profile, while the plate prevents or reduces the ambient air entrainment.

The different experimental test cases are gathered in Tab.6.1. The experimental investigations show that due to the non-stabilized free-burning designed construction, the operating range of the burner is severely limited. It was found that specially at higher Reynolds numbers and preheating temperatures the flame stabilize only by means of very rich mixtures as a result of imbalance between flow velocity and burning velocity of the flame [116].

For this reason the equivalence ratio is held as $\phi = 1.3$ in the main investigated test cases. Three different Reynolds number are chosen 6000, 7500 and 9000 to identify the acoustic scaling laws. The preheating temperatures are also varied from the minimum of T=293 [K] to the maximum of T=433 [K]. Overall five cases are investigated using equivalence ratio of $\phi = 1.3$ and one test case with a leaner and non-preheated mixture (equivalence ratio of $\phi = 1.05$) with moderate Reynolds number (See Tab.6.1).

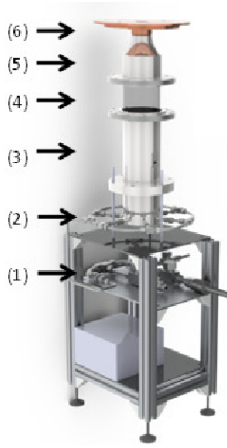

Figure 6.1: Berlin burner experimental setup [116].

Case	Re	T_u	ϕ
1	7500	293	1.3
2	7500	373	1.3
3	6000	373	1.3
4	7500	433	1.3
5	9000	373	1.3
6	7500	293	1.05

Table 6.1: Berlin burner experimentally investigated cases.

The velocity profiles are measured in the quartz glass (See Fig.6.1 section 4) upstream of the nozzle using the LDA (Laser Doppler Anemometry) technique. The upstream measured velocities are used in the numerical investigations as the inlet boundary condition. The radial profiles of velocities are measured using PIV (Particle Image Velocimetry) at three different planes (x=1.0d, 3.0d and 5.0d) downstream of the nozzle. The acoustic benchmark is obtained using condenser microphones [117].

6.1.0.2 Numerical setup

The Berlin burner is numerically investigated using two different combustion models (ATF and F-TACLES) coupled with the dynamic and non-dynamic versions of the power-law wrinkling model. The numerically investigated test cases for the Berlin burner configuration are gathered in Tab.6.2.

The computational domain consists of a part of the nozzle starting from quartz glass (See Fig.6.1 section 4). The grid has a size of approximately 3.1 million cells which is systematically refined with a grid size of $\Delta_{min} = 1.0$ (mm) in the region of interest. The grid form is held cubic in the nozzle up and downstream.

The chemistry look up table is constructed using FGM (Flamelet-Generated Manifolds) [68] technique. It consist of one progress variable (CO_2 mass fraction) and one mixture fraction variable. All other dependent variables are tabulated based on these two variables. The CHEM1D code [89] is used to calculate the internal flame structure applying the GRI 3.0 mechanism [90] which contains 325 reactions and 53 species. Overall 4 different look-up tables have been produced depending on the equivalence ration and fuel preheating temperature.

Fig.6.2 shows the maximum progress variable source term $[kg/m^3s]$ at the corresponding equivalence ratio. The effect of preheating is clearly to observe. The progress variable source term increases with the increasing the preheating temperature. This concludes to a higher laminar flame speed as also depicted in Fig.6.3.

Fig.6.3 shows the corresponding laminar flame speed of the investigated test cases against equivalence ratio ϕ. The comparison shows the effect of preheating on the laminar flame speed of the methane/air flame. The preheating causes a direct increase of laminar flame speed. For example the maximum laminar flame speed of the flame with $T_u = 293$ $[K]$ at equivalence ratio ϕ=1.05 is the $S_l \approx 28$ (cm/s) which is increased to the $S_l \approx 38$ (cm/s) with a $T_u = 373$ $[K]$ and is $S_l \approx 47$ (cm/s) corresponding to the $T_u = 433$ $[K]$.

Fig.6.4 shows the adiabatic flame temperature of the investigated methane/air flame with different preheating conditions. It is to observe that the preheating has not a very strong effect on the adiabatic flame temperature. Furthermore, the laminar flame thickness (thermal) δ_l^0 is also not strongly affected due to the preheating in these configurations.

The turbulence parameters T_i and L_t are used by the inflow generator [57] together with the velocity profile $U_{inlet}(r)$ corresponding to boundary condition of the experimental configuration. The co-flow considered as air at ambient conditions which is also tabulated in look up tables.

Combustion model	**Wrinkling model**	ϕ	T_u **[K]**	**Re**	**Case**
ATF [a]	Power-law	1.3	293	7500	1b
	Power-law (Dyn)	1.3	373	7500	2b
	Power-law	1.3	373	6000	3b
	Power-law (Dyn)	1.3	433	7500	4b
	Power-law	1.3	373	9000	5b
	Power-law	1.05	293	7500	6b
F-TACLES [b]	Power-law	1.05	293	7500	7b

[a] Artificially Thickened Flame
[b] Filtered Tabulated Chemistry For LES

Table 6.2: The different numerical test cases investigated for the Berlin burner configuration.

6.2 Results

6.2.0.3 Analysis of the influence of the different operating conditions

For the analysis of the influence of the operating conditions on the induced combustion noise the Reynolds number, the equivalence ratio and the preheating were systematically varied using the generic burner [117], [118]. The seven numerically investigated test cases are summarized in Tab.6.2. The case 1b represents the reference configuration. For the analysis of the flame with the momentum variations, the cases 3b and 5b are investigated. For the analysis of preheating temperature variations, the cases 2b and 4b have been investigated and compared . The cases 6b and 7b are the additional configurations with a leaner fuel-air mixture which are used for the verification and validation of the newly developed F-TACLES combustion model [13], [23].

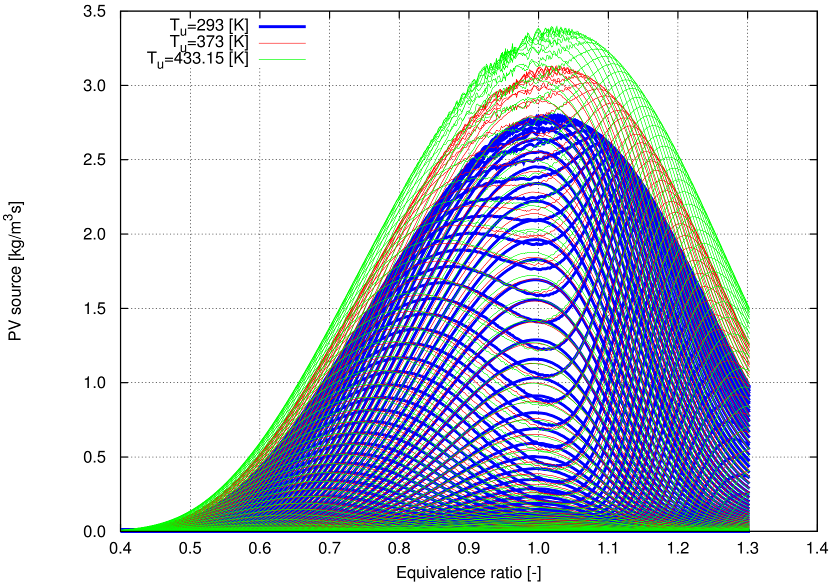

Figure 6.2: Effect of the preheating on the PV source term ($\dot{\omega}$), left with T_u=373 [K] and right with T_u=433.15 [K].

6.2.1 Numerical investigation of the momentum variation

The main aim of this investigation is to analyze the interaction of the boundary condition, model and numeric on the combustion induced noise. In the first step the influence of the different momentum on the flame structure and the induced noise were investigated using LES/CAA approach [118].

Fig.6.5 gives an impression of the contours of the averaged progress variable at the Re = 6000 (case 3b) and at the Re = 7500 (case 2b). The contours have a similar structure. The premixed flame with a smaller Reynolds number (case 3b), as expected, is slightly shorter than the flame at higher Reynolds number in (case 2b). The enveloping diffusion flame shows a contrasting behavior, as the fuel is consumed faster at the higher flow rates.

Fig.6.6 shows the comparison of the mean velocities for the both test cases as compared with the measurements. Increasing the Reynolds number in configurations with the identical mixture composition and same pre-heating temperature results in a direct increase in the flow rate and consequently to a higher degree of turbulence consequently an increase in the sound level [118]. The comparison of the mean axial and radial velocities shows a good agreement with the experimental results at the different axial planes.

The temperature profiles are not provided by the experiment for this configuration. Nevertheless, the actual premixed flame height can be estimated from the predicted profiles of radial velocity. Fig.6.6 shows that the simulation slightly over predict the radial velocity in x=5.0d0. Therefore, we can conclude that the predicted flame height is under predicted and the corresponding turbulent flame speed is over predicted using fixed values ($\beta = 0.5$) of the exponent in the power-law wrinkling model [19]. The application of the dynamic procedure for calculation of the power-law wrinkling factory will be further discussed in the section 6.2.4.

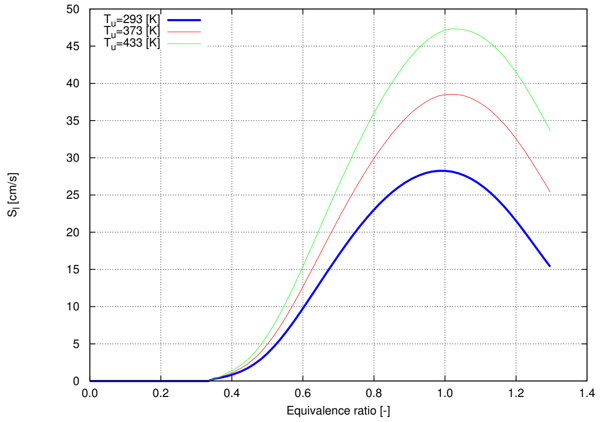

Figure 6.3: Effect of the preheating on the laminar flame speed for an atmospheric methane/air flame.

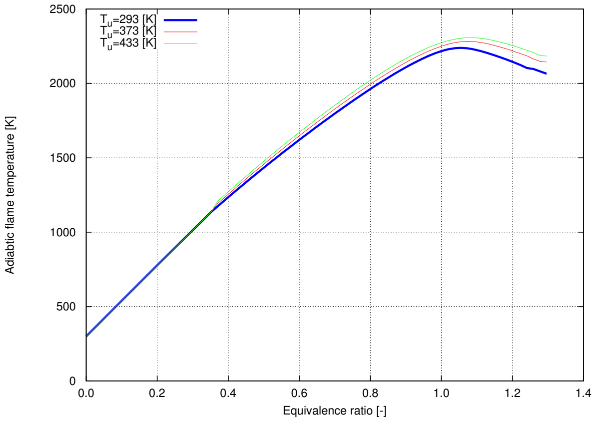

Figure 6.4: Effect of the preheating on the adiabatic flame temperature.

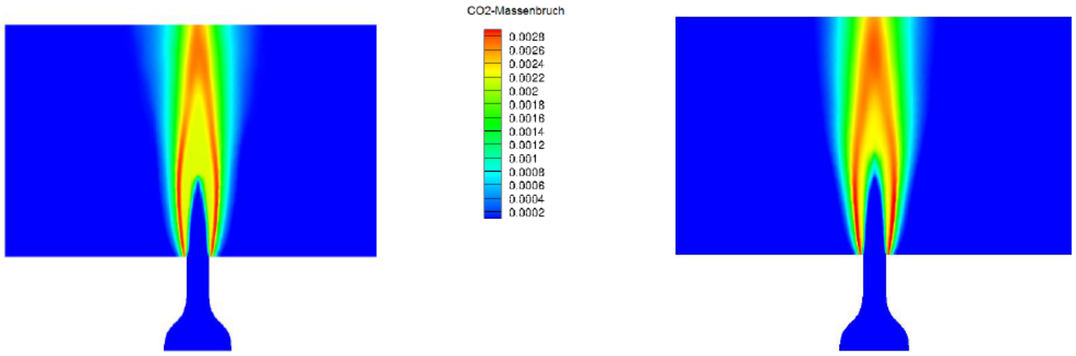

Figure 6.5: Contour plots of the reaction progress variable (CO_2 mass fraction), left hand side: case 3b (Re=6000) and right hand side: case 2b (Re=7500).

6.2.2 Numerical investigation of the preheating variation

Furthermore, the influence of the different fuel preheating on the flame structure and acoustic emission was investigated by means of the LES/CAA approach.

Fig.6.7 shows a comparison of the contour plots of the averaged progress variable for both test cases 2b and 4b. A significant difference between these two cases is observed. The enveloping diffusion flame is smaller in the case with higher preheating temperature (4b). As shown in Fig.6.3 the case 4b has the largest laminar flame speed which is an indicator of higher consumption rate in comparison to the other cases.

Furthermore the flame index proposed by Yamashita et al. [119] is applied to the investigated configurations. Using the flame index the premixed and diffusion flame can be identified. The normalized form of the flame index reads as:

$$\alpha = \frac{\nabla Y_F \cdot \nabla Y_O}{|\nabla Y_F \cdot \nabla Y_O|}, \tag{6.1}$$

where ∇Y_F is the gradient of the fuel mass fraction and the ∇Y_O is the gradient of the oxidizer mass fraction. The α=1 indicates the premixed regime when the gradient of the fuel and oxidizer are in the same direction and the α=-1 shows the diffusion like combustion when the fuel and oxidizer gradient are in the opposite direction.

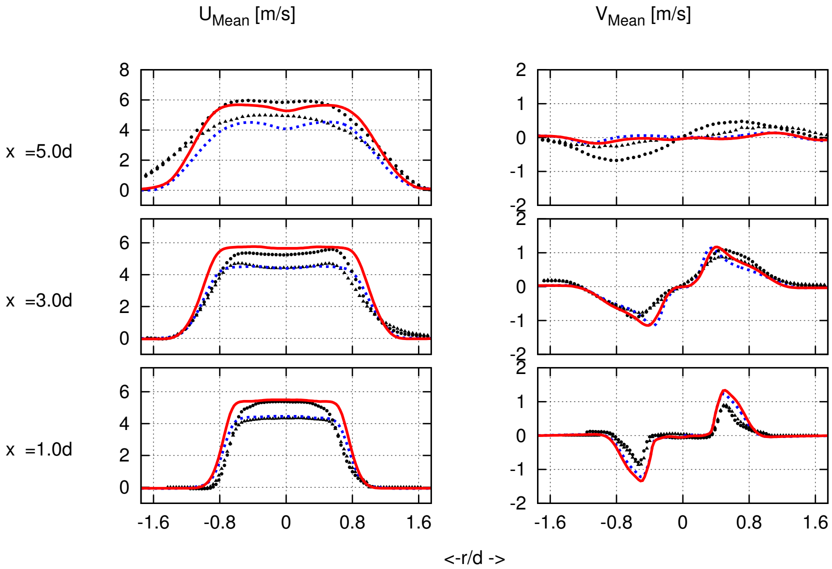

Figure 6.6: Profiles of time averaged axial and radial velocities at x=1.0d, 3.0d0 and 5.0d0 nozzle (d=35 (mm) downstream positions. Solid line: test case 2b, dotted line: test case 3b, experiment, ●: test case 2b and ▲: test case 3b.

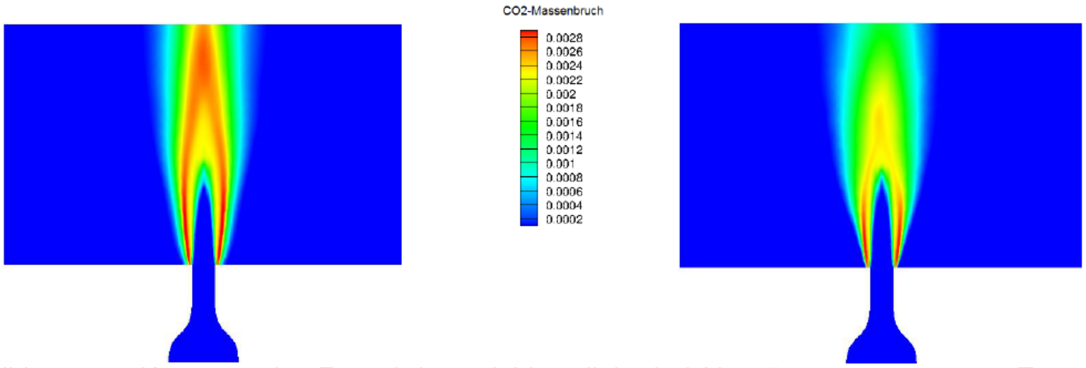

Figure 6.7: Contour plots of the reaction progress variable (CO_2 mass fraction), left hand side: case 2b (T_u=373 [K]) and right hand side: case 4b (T_u=433 [K]).

Fig.6.8 shows the comparison of the flame index superimposed with the equivalence ratio lines for both test cases 2b and 4b. The flame index shows a rich premixed regime with equivalence ratio of $\phi \approx 1.3$ and a thin surrounding diffusion flame ($\phi \approx 1.0$). Concerning the progress variable reaction rate $\dot{\omega}_c$, it can be concluded that the main reaction zone is the rich premixed one, the diffusion regime occurs only within a very small reaction rate and therefore are very slow.

Fig.6.9 shows the comparison of the mean velocities for the altered preheating and the corresponding experimental data. Increasing the preheating temperature while keeping the same composition of the mixture and the same Reynolds number, results in a significant increase in the flow rate, cause of simultaneous decrease of the density and increase of the viscosity. The corresponding increase in the flow rate results in a larger turbulence intensity and in turn an increase in the sound level [118]. The comparison of the mean

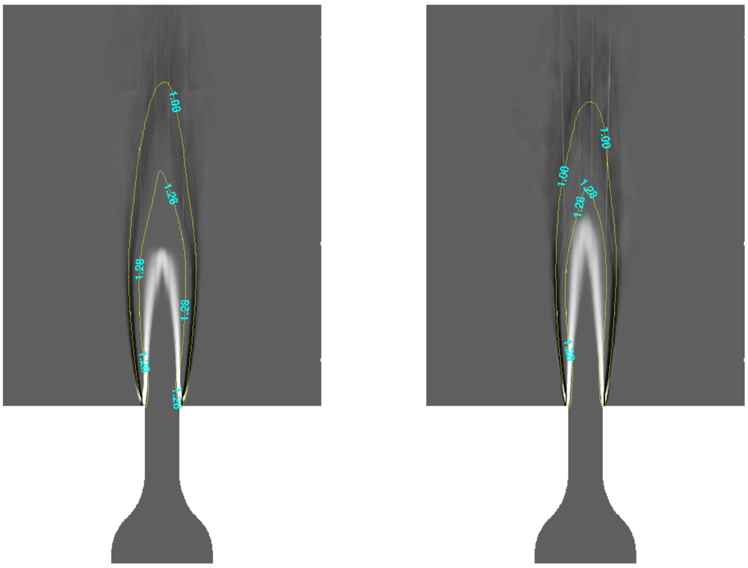

Figure 6.8: Contour plots of the normalized flame index superimposed with the equivalence ratio of the mixture, left hand side: case 2b (T_u=373 [K]) and right hand side: case 4b (T_u=433 [K]). Premixed flame: white color, diffusion flame: black color.

axial and radial velocities shows a good agreement with the experimental results at different axial planes. In the case (4b), the predicted premixed flame height is shorter than the experiment, according to the radial velocity measurements.

6.2.3 Numerical investigation of the Berlin burner using F-TACLES combustion model

As explained previously, the analysis of the combustion induced noise source terms with the acoustic perturbation equations (APE) approach shows that the total time derivative of the density represents the dominant term in the combustion noise generation [118]. Since the ATF model is based on the thickening of the flame front, it should be assured that this spatial smearing of the density jump is permitted. The next question is the effect of thickening on the predicted induced noise and the corresponding limits (Mesh resolution and thickening factor).

The newly developed F-TACLES [13] combustion model is based on a preliminary filtering of the flamelets, so that the premixed flames are better resolved by the LES mesh grid. This method thus promises less smearing of the density jump.

The 1d filtered flame structure is shown in Fig.6.10 for a set of filter widths at the equivalence ratio of $\phi = 1.05$[-]. The progress variable source term is depicted in the progress variable space. The effect of filtering is limited for small filter width Δ. For larger filter width values the diffusion increases strongly specially for progress variable

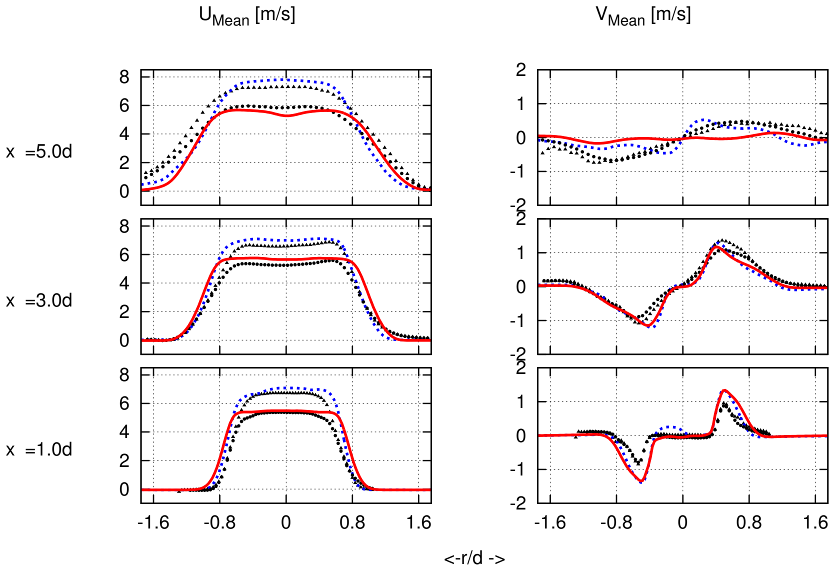

Figure 6.9: Profiles of time averaged axial and radial velocities at x=1.0d, 3.0d0 and 5.0d0 nozzle (d=35 (mm) downstream positions. Solid line: test case 2b, dotted line: test case 4b, experiment, ●: test case 2b and ▲: test case 4b.

values smaller than 0.5.

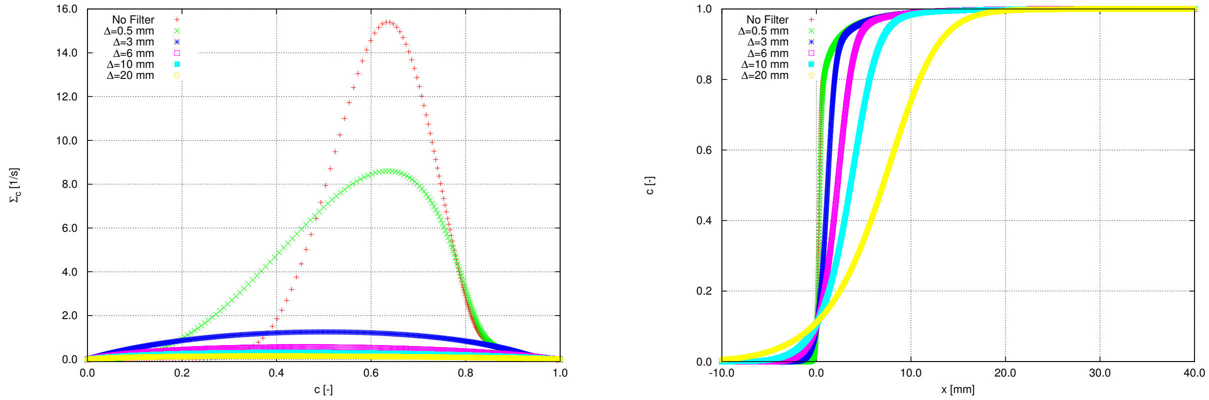

Figure 6.10: 1d filtered flames for different filter widths for the equivalence ratio ϕ=1.05. Left: filtered progress variable source term and right filtered progress variable.

The filtered progress variable (Normalized CO_2 mass fraction) are depicted in Fig.6.10. The larger filter Δ makes the progress variable to be smeared. It's to note that the filter width used in the F-TACLES model can be approximately compared to the ATF thickening factor. For example as illustrated in Fig.6.11 at the equivalence ratio of $\phi =$ 1.05[-], the $\Delta = 6\ mm$ corresponds to a thickening factor of F=Δ_x/δ_l^0 and has a value of approximately 6. The Fig.6.11 shows that the same behavior can be observed for the ϕ=0.85 to 1.1. For leaner or richer mixtures the behavior is not linear any more.

Fig.6.11 shows the maximum $\Sigma_c = -\Omega_c + \tilde{\dot{\omega}}_c$ $[1/s]$ and the ratio of the corresponding filtered laminar flame thickness δ_l^f $[m]$ to the laminar flame thickness δ_l^0 $[m]$ for a set of different filter widths Δ in the equivalence ratio ϕ $[-]$ space extracted from the F-TACLES look-up table. The comparison shows that the filtering effect by choosing a filter width of smaller or equal to the thermal flame thickness is limited. Choosing a larger filter Δ than the thermal flame thickness δ_l^0 $[m]$ causes in an increase in filtered laminar flame thickness δ_l^f $[m]$ and consequently make the premixed flame resolvable using LES mesh.

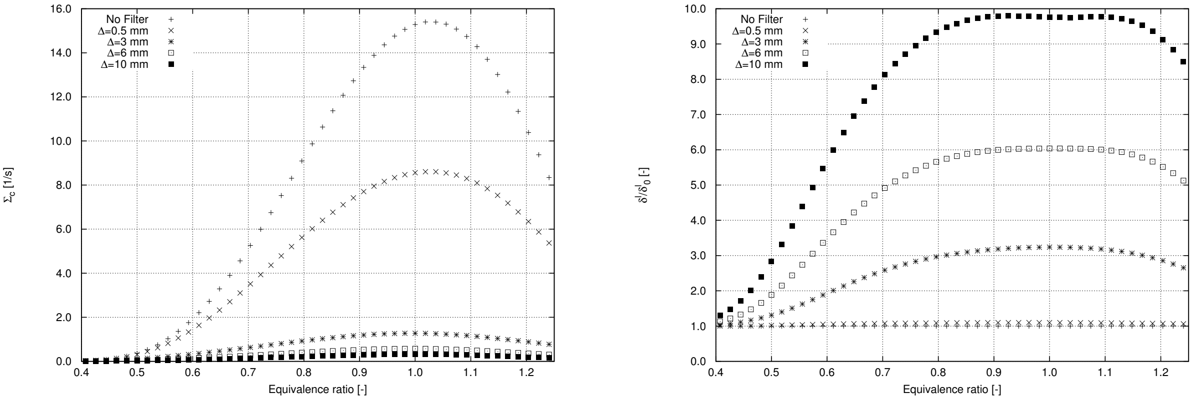

Figure 6.11: The Σ_c $[1/s]$ and the ratio of the filtered to non-filtered laminar flame thickness (thermal) δ_l^f/δ_l^0 $[-]$ for different filter widths in F-TACLES combustion model.

The test cases 6a and 7b (See Tab.6.2) are investigated to check the effect of the different combustion modeling on the predicted induced noise using LES/CAA. The comparison of the flow and combustion properties is addressed in this work.

The experimental test case 6 (See Tab.6.1) uses a mixture of methane and air without preheating at ambient temperature. The Reynolds number at the nozzle exit is Re $= 7500$ and the equivalence ratio is phi $= 1.05$. Since this is a comparison between two combustion models, all boundary conditions and the computational grid for both simulations are set to be identical, the thickening factor of the ATF combustion model and the filter width in the F-TACLES combustion model is also kept identical.

Since this flame in comparison with the other cases (1 to 6 See Tab.6.2) has been operated with smaller equivalence ratio ($\phi = 1.05$), the premixed flame is predominant.

The both combustion models show comparable results in instantaneous and averaged contours. the FTACLES combustion model shows a higher interaction between the flame and turbulence as too be seen also in OH PLIF from experiment, even though the flame exist in a quasi-laminar flow regime following the comparatively low Reynolds numbers (Re $= 7500$).

Figure 6.12 shows the quantitative comparison between the radial profiles of the averaged velocities for the ATF and the F-TACLES model and the experiment. The comparison of the mean axial and radial velocities for both combustion models shows a good agreement with the experimental results in planes x=1.0 d and x=5.0 d nozzle downstream. Just in plane x=3.0 d nozzle downstream the predicted radial velocity using ATF model shows deviation comparing to the experiment and F-TACLES model. However it has been shown that this is an effect of wrong calculation of the turbulent flame speed using non-dynamic version of the power-law wrinkling model. Thus this deviation is not related to the chosen combustion model.

A comparison of the mean temperature and temperature fluctuation (Fig.6.13) are also very satisfactory in all levels for both combustion models in all planes downstream of

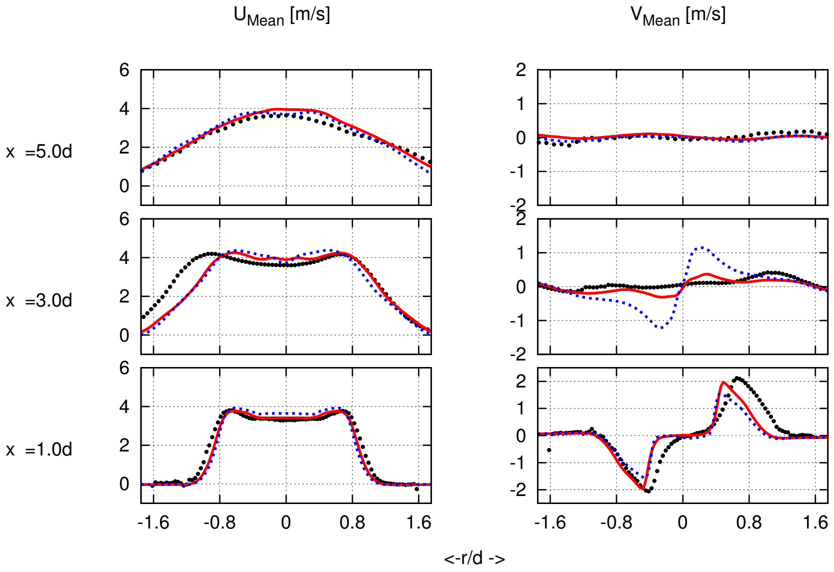

Figure 6.12: Profiles of time averaged axial and radial velocities at x=1.0d, 3.0d0 and 5.0d0 nozzle (d=35 (mm) downstream positions. Solid line: test case 7b, dotted line: test case 6b, symbol (•) : experiment.

the nozzle. The deviation observed in plane x=3.0 d nozzle downstream is related to overestimated wrinkling factor as explained before.

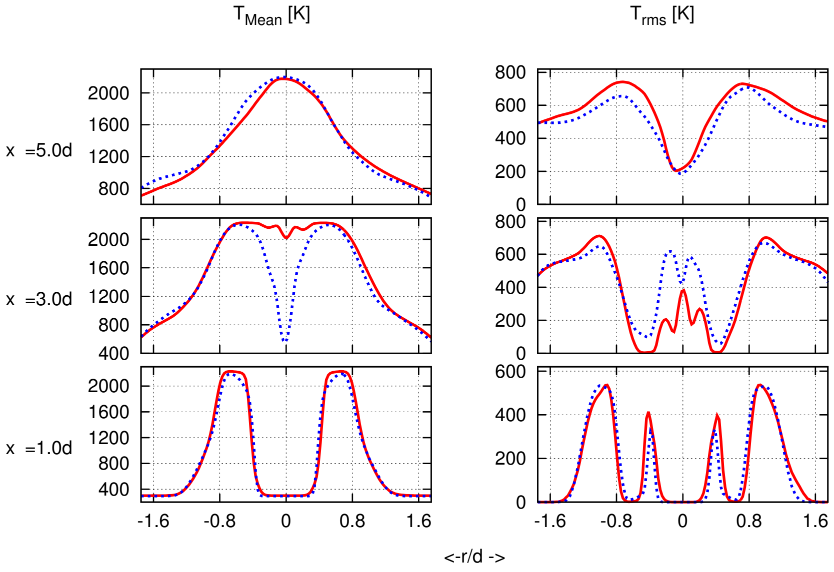

Figure 6.13: Profiles of time averaged temperature and the corresponding fluctuation at x=1.0d, 3.0d0 and 5.0d0 nozzle (d=35 (mm) downstream positions. Solid line: test case 7b, dotted line: test case 6b, symbol (•) : experiment.

6.2.4 Dynamic power-law wrinkling model applied to the Berlin burner

The investigated benchmark is located in the quasi laminar regime and the turbulence intensity is very low in this configuration. Therefore the turbulence and flame interaction is very low and the investigation shows that the flame is not strongly wrinkled. Nevertheless the dynamic wrinkling model is applied to the benchmark to investigate the model in these low turbulence regimes.

Two cases are investigated using ATF combustion model [11], [15] and the dynamic version of the power-law wrinkling model [19], [21]. The Reynolds number is held as constant (Re=7500) and just fuel preheating is considered to change (T=373 and 433) (See also Tab.6.2).

The simulation results introduced in section 6.2 are all conducted using non-dynamic version of the power-law wrinkling model with the fixed power value of $\beta = 0.5$. In this section the test cases 2b and 4b are calculated using dynamic formulation of the power-law wrinkling model. The results of the simulations are then compared with the results of the section 6.2 which uses the non-dynamic version of the power-law wrinkling model with a fixed power value of β=0.5.

6.2.4.1 Investigation of test case 2b using DATF

The dynamic version of the power-law wrinkling model [19] is applied to the test case 2b. The temporal evolution of β power averaged over whole domain is depicted in Fig.6.14 for the test case 2b. The β has a maximum value of 0.33 and minimum value of 0.26 and average value of 0.3. As mentioned before due to the small turbulence intensity the wrinkling factor is also very small.

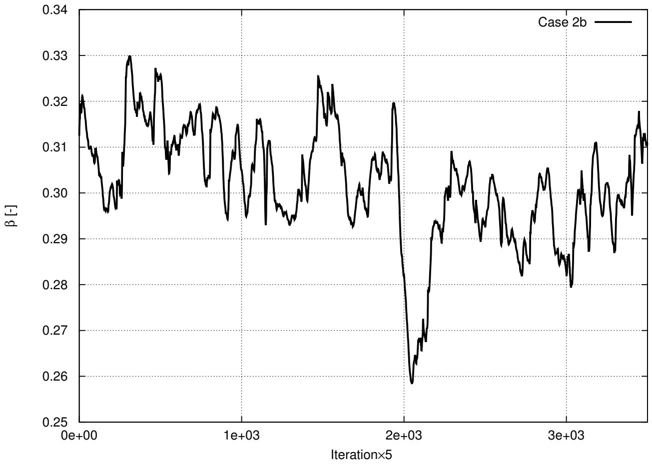

Figure 6.14: The temporal evolution of the β power averaged over whole domain for the test cases 2b.

Fig.6.15 shows the instantaneous contour plots of the dynamic power-law wrinkling model quantities. The resolved progress variable source term from LES $\dot{\omega}_{\tilde{c}}$ $[kg/m^3s]$, the test filtered progress variable source term $\widehat{\dot{\omega}_{\tilde{c}}}$ $[kg/m^3s]$ and the source term from test filtered progress variable and mixture fraction $\dot{\omega}_{\hat{\tilde{c}}}$ $[kg/m^3s]$. The test filtered source term looks like the resolved source term on a coarser mesh grid. In this case the progress

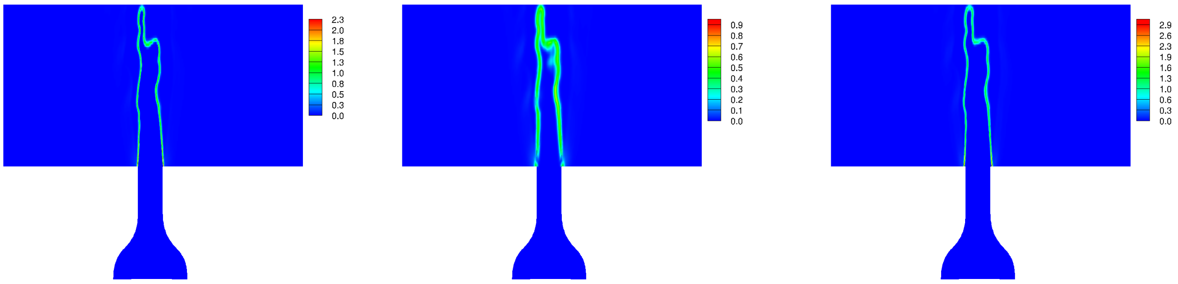

a. b. c.

Figure 6.15: Contour plots of the instantaneous dynamic wrinkling model quantities. a: resolved progress variable source term $\dot{\omega}_{\tilde{c}}$ $[kg/m^3 s]$; b: test filtered progress variable source term $\widehat{\dot{\omega}_{\tilde{c}}}$ $[kg/m^3 s]$; c: source term from test filtered progress variable and mixture fraction $\dot{\omega}_{\hat{\tilde{c}}}$ $[kg/m^3 s]$ for the test case 2b.

variable source term from test filtered progress variable and mixture fraction $\dot{\omega}_{\hat{\tilde{c}}}$ $[kg/m^3 s]$ is similar to the LES resolved source term and has only a higher maximum magnitude.

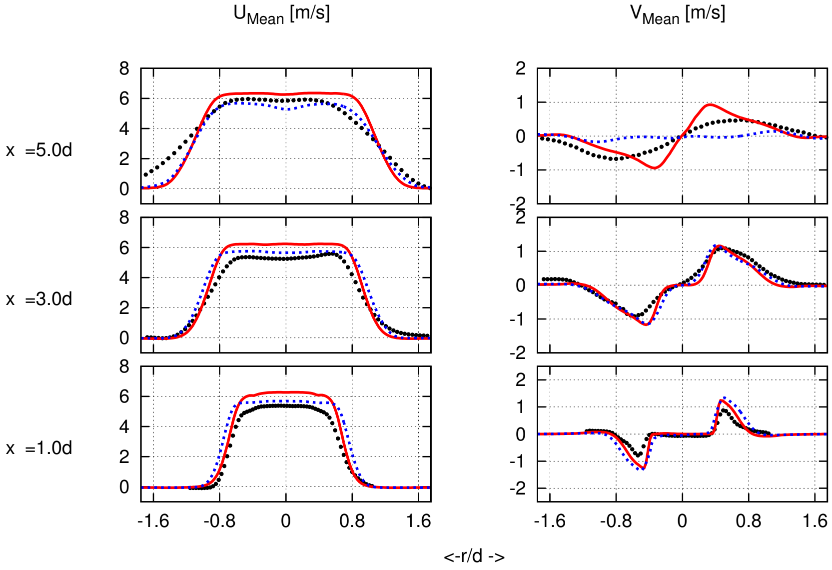

Figure 6.16: Profiles of time averaged axial and radial velocities at x=1.0d, 3.0d0 and 5.0d0 nozzle (d=35 (mm)) downstream positions. Solid line: test case 2b (Dyn), dotted line: test case 2b (Non-dyn), experiment.

Fig.6.16 shows the comparison of the mean velocities for the test case 2b using dynamic and non-dynamic version of the wrinkling model. The comparison of the mean axial and radial velocities shows a good agreement with the experimental results at different axial planes for both wrinkling models. Just in plane x=5.0d the radial velocity shows deviations from the experiment.

In the Bunsen type flame, the radial velocity is perpendicular to the flame. Therefore the radial velocity will be zero when the flame vanishes. In this configuration, the experiment shows that the flame height is larger than the 5.0d. The same behavior is addressed using dynamic version of the power-law wrinkling model. The simulation using non-dynamic version of the power-law overestimates the wrinkling factor and consequently the turbulent flame speed.

Fig.6.17 shows the comparison of the mean temperature and the corresponding fluctuations for the test case 2b using dynamic and non-dynamic version of the wrinkling model. The averaged profiles of temperature for these both test case show fair agreement in plane x=1.0d0 and x=3.0d0 nozzle downstream. The simulation shows aslo deviation in temperatute profiles in shear layer in these planes. In the plane x=5.0d0 nozzle downstream, the deviation shows that the test case using dynamic version of the power-law wrinkling model predicts a longer premixed flame. The later finding is also compatible with the results of the averaged radial velocity in plane x=5.0d0 nozzle downstream.

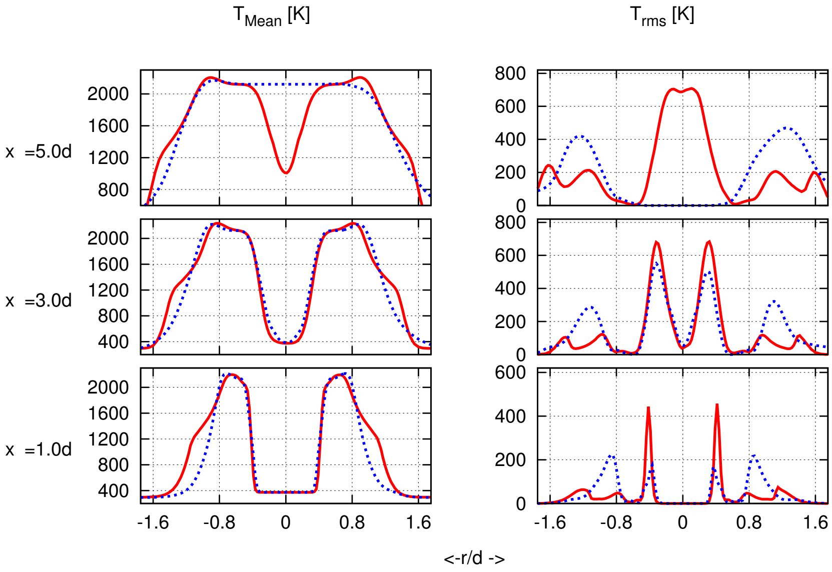

Figure 6.17: Profiles of time averaged temperature and corresponding fluctuations at x=1.0d, 3.0d0 and 5.0d0 nozzle (d=35 (mm)) downstream positions. Solid line: test case 2b (Dyn), dotted line: test case 2b (Non-dyn).

6.2.4.2 Investigation of test case 4b using DATF

The dynamic version of the power-law wrinkling model [19] is applied to the test case 4b. The temporal evolution of β power averaged over whole domain is depicted in Fig.6.18 for the test case 4b. The β has a maximum value of 0.2 and minimum value of 0.14 and average value of 0.18. As mentioned before due to small turbulence intensity the wrinkling factor is also very small.

Fig.6.19 shows the instantaneous contour plots of the dynamic power-law wrinkling model quantities. The resolved progress variable source term from LES $\dot{\omega}_{\tilde{c}}$ $[kg/m^3s]$, the test filtered progress variable source term $\widehat{\dot{\omega}_{\tilde{c}}}$ $[kg/m^3s]$ and the source term from test filtered progress variable and mixture fraction $\dot{\omega}_{\hat{\tilde{c}}}$ $[kg/m^3s]$. The test filtered source term looks like the resolved source term on a coarser mesh grid. In this case the the progress

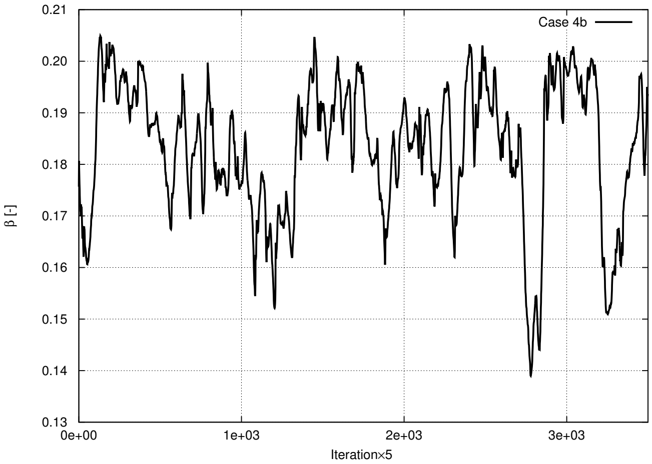

Figure 6.18: The temporal evolution of the β power averaged over whole domain for the test cases 4b.

variable source term from test filtered progress variable and mixture fraction $\dot{\omega}_{\hat{\tilde{c}}}$ $[kg/m^3s]$ is similar to the LES resolved source term and has only a higher maximum magnitude.

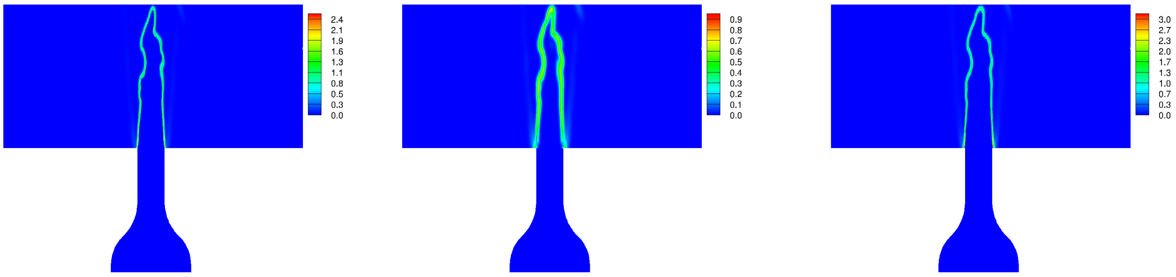

a. b. c.

Figure 6.19: Contour plots of instantaneous dynamic wrinkling model quantities. a: resolved progress variable source term $\dot{\omega}_{\tilde{c}}$ $[kg/m^3s]$; b: test filtered progress variable source term $\widehat{\dot{\omega}_{\tilde{c}}}$ $[kg/m^3s]$; c: source term from test filtered progress variable and mixture fraction $\dot{\omega}_{\hat{\tilde{c}}}$ $[kg/m^3s]$ for the test case 4b.

Fig.6.20 shows the comparison of the mean velocities for the test case 4b using dynamic and non-dynamic version of the wrinkling model. The comparison of the mean axial and radial velocities shows a good agreement with the experimental results at different axial planes for both wrinkling models.

Fig.6.21 shows the comparison of the mean temperature and the corresponding fluctuations for the test case 4b using dynamic and non-dynamic version of the wrinkling model. The comparison shows that also the effect of dynamic formulation of the power-law wrinkling model. The flame is found to be slightly longer than the one predicted using non-dynamic models. Although as described before, this flame is not much wrinkled due to very small turbulence intensity. Therefore the model constant is also found to be very low which confirms the model assumptions.

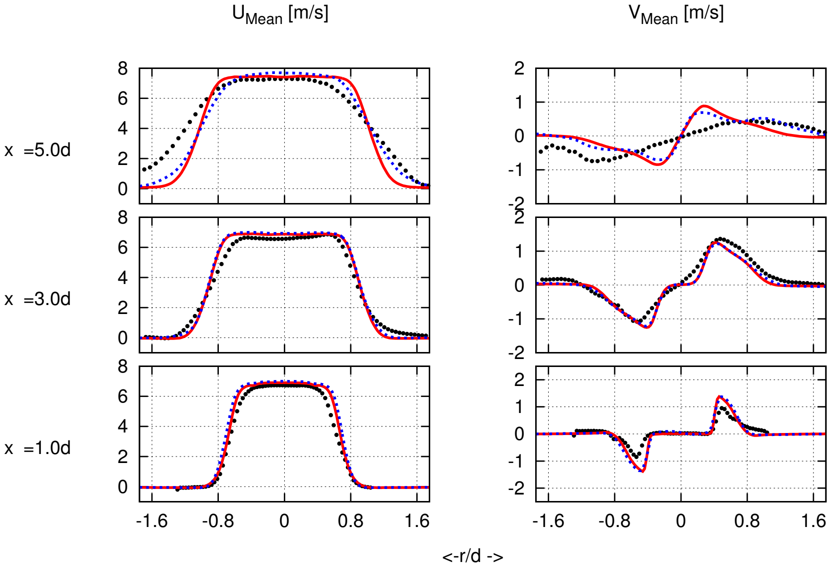

Figure 6.20: Profiles of time averaged axial and radial velocities at x=1.0d, 3.0d0 and 5.0d0 nozzle (d=35 (mm)) downstream positions. Solid line: test case 4b (Dyn), dotted line: test case 4b (Non-dyn), experiment.

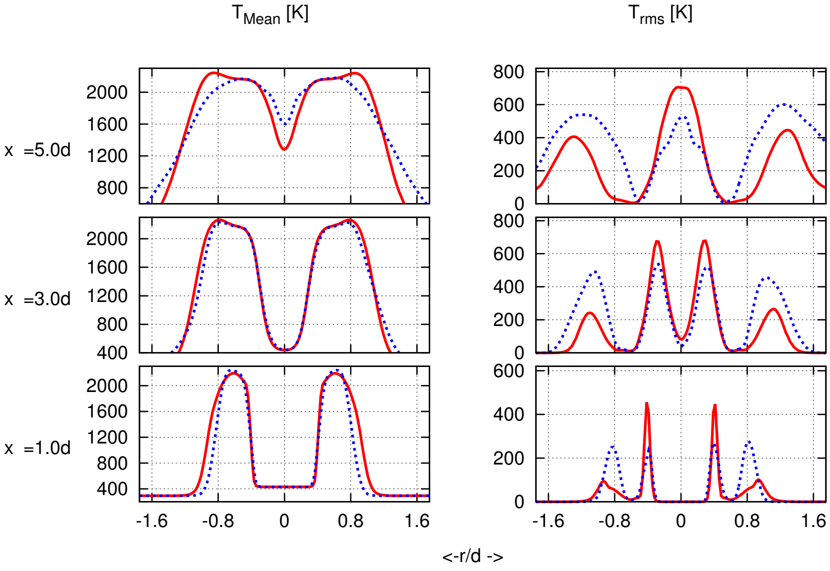

Figure 6.21: Profiles of time averaged temperature and corresponding fluctuations at x=1.0d, 3.0d0 and 5.0d0 nozzle (d=35 (mm)) downstream positions. Solid line: test case 4b (Dyn), dotted line: test case 4b (Non-dyn).

6.3 Conclusions

In this section series of simulations are conducted for a generic burner (Berlin burner) with two combustion models under using dynamic and non-dynamic formulations of power-law wrinkling model. Different test cases are simulated to understand the effect of preheating and momentum alternation on the flow field. This simulation are used as input for the prediction of the combustion noise in premixed combustion using LES/CAA method [118].

The dynamic power-law wrinkling model coupled with artificially thickened flame model and FGM tabulated chemistry is applied to two chosen test cases. The effect of the dynamic model is limited as the flames are positioned in the quasi-laminar regime and flame is not strongly wrinkled. Nevertheless the dynamic wrinkling model shows correct tendency and decreases the power exponent from the standard value $\beta = 0.5$. Hence this decrease leads to a longer flame height. Unfortunately, the experimental results for the temperature field is not available. But the transverse velocity direction as a good indicator for the flame height is in a good agreement with the simulation results of dynamically calculated wrinkling model.

Chapter 7

Summary and outlook

Summary

In the following the developments and results based on the current work are summarized:

- The current work introduces an extension of an artificially thickened flame approach coupled with Flamelet Generated Manifolds (FGM) tabulated chemistry [15] with a dynamic wrinkling model [19].
- The dynamic power-law wrinkling model is coupled with the Flamelet Generated Manifolds (FGM) tabulated chemistry.
- To analysis this model improvement, simulations are conducted for a lean premixed Bunsen type flame (Matrix Burner) with high turbulent intensity, using the ATF (Artificially Thickened Flame) combustion model on two grid levels.
- For validation of results, the same simulations are conducted with other combustion model, F-TACLES (Filtered TAbulated Chemistry for LES), both with dynamic and non-dynamic formulations of power-law wrinkling model. The dynamic formulation of the F-TACLES approach has been implemented in the same code and evaluated for different configurations [23, 24]
- The numerical investigations using non-dynamic version of wrinkling models coupled with both combustion models on all two grid levels fail to predict the flow and temperature characteristics.
- The simulation using developed dynamic power-law wrinkling model shows excellent results comparing to the experiment independent of grid level used.
- Series of simulations are conducted in the frame work of “combustion noise” research project in collaboration with three other research groups. The newly developed dynamic power-law wrinkling model coupled with artificially thickened flame model and FGM chemistry is also applied to two chosen test cases. The effect of the dynamic model is clear to observe but limited as the flames are positioned in the quasi-laminar regime.
- The conclusion is that: for the correct prediction of premixed flames with high turbulent intensity, elaboration of combustion models coupled with dynamic subgrid scale modeling is inevitable.

Outlook

Series of simplifications are assumed both in modeling and numerical sections of the current investigations.

In the modeling side is the definition of modeled turbulence fluctuation (Eq.4.27) at both filter and test filter levels. The suggested simplification of the Eq.4.38 in the limiting case of large turbulence intensities leads to a more simplified model (Eq.4.40) which is then easier for implementation.

Although eventually the full model (Eq.4.20) will be used in the context of transport equation, the effect of this simplification should be investigated. This can be done in comparison of the flow and scalar characteristics with results of appropriate DNS investigations.

The second simplifications and assumptions are carried out in the numerical methods, namely retaining only the second order of the Gaussian filter (Eq.4.47). It is to recommend to investigate this simplification.

The other numerical issue is the conduction of different numerical methods and their influence on the predicted results. As described before, different numerical methods have their ad and disadvantages. Conducting the numerical simulation implicitly using the incomplete LU decomposition delivers first order upwind which is always stable and monotonic but the with limiting first order approximation. The Euler scheme can be increased using Gauss formalism which needs few mandatory additional sub steps to suppress unphysical oscillations. Using implicit approach, the orthogonal part will be solved implicitly while the non-orthogonal contribution is explicitly solved. The current approach leads to numerical oscillations with strongly stretched grids. Therefore it is to recommend to investigate the current issue using more analytical and experimental configurations to find best numerical method.

Bibliography

[1] S. Candel, D. Durox, T. Schuller, N. Darabiha, L. Hakim, and T. Schmitt, "Advances in combustion and propulsion applications," *European Journal of Mechanics - B/Fluids*, vol. 40, no. 0, pp. 87 – 106, 2013.

[2] E. Knudsen and H. Pitsch, "Capabilities and limitations of multi-regime flamelet combustion models," *Combustion and Flame*, vol. 159, no. 1, pp. 242 – 264, 2012.

[3] V. Hiremath, Z. Ren, and S. B. Pope, "Combined dimension reduction and tabulation strategy using ISAT-RCCE-GALI for the efficient implementation of combustion chemistry," *Combustion and Flame*, vol. 158, no. 11, pp. 2113 – 2127, 2011.

[4] D. V. T. Poinsot, *Theoretical and Numerical Combustion.* third edition ed., 2012.

[5] J. Janicka and A. Sadiki, "Large eddy simulation of turbulent combustion systems," *Proceedings of the Combustion Institute*, vol. 30, no. 1, pp. 537 – 547, 2005.

[6] H. Pitsch, "Large-eddy simulation of turbulent combustion," *Annual Review of Fluid Mechanics*, vol. 38, no. 1, pp. 453–482, 2006.

[7] H. Pitsch, "A consistent level set formulation for large-eddy simulation of premixed turbulent combustion," *Combustion and Flame*, vol. 143, no. 4, pp. 587 – 598, 2005.

[8] E. Knudsen and H. Pitsch, "A dynamic model for the turbulent burning velocity for large eddy simulation of premixed combustion," *Combustion and Flame*, vol. 154, no. 4, pp. 740 – 760, 2008.

[9] V. Moureau, B. Fiorina, and H. Pitsch, "A level set formulation for premixed combustion LES considering the turbulent flame structure," *Combustion and Flame*, vol. 156, no. 4, pp. 801 – 812, 2009.

[10] M. Boger, D. Veynante, H. Boughanem, and A. Trouvé, "Direct numerical simulation analysis of flame surface density concept for large eddy simulation of turbulent premixed combustion," *Symposium (International) on Combustion*, vol. 27, no. 1, pp. 917 – 925, 1998.

[11] O. Colin, F. Ducros, D. Veynante, and T. Poinsot, "A thickened flame model for large eddy simulations of turbulent premixed combustion," *Physics of Fluids (1994-present)*, vol. 12, no. 7, pp. 1843–1863, 2000.

[12] F. Charlette, C. Meneveau, and D. Veynante, "A power-law flame wrinkling model for LES of premixed turbulent combustion part one: non-dynamic formulation and initial tests," *Combustion and Flame*, vol. 131, no. 1–2, pp. 159 – 180, 2002.

[13] B. Fiorina, R. Vicquelin, P. Auzillon, N. Darabiha, O. Gicquel, and D. Veynante, "A filtered tabulated chemistry model for LES of premixed combustion," *Combustion and Flame*, vol. 157, no. 3, pp. 465 – 475, 2010.

[14] P. Auzillon, O. Gicquel, N. Darabiha, D. Veynante, and B. Fiorina, "A filtered tabulated chemistry model for LES of stratified flames," *Combustion and Flame*, vol. 159, no. 8, pp. 2704 – 2717, 2012.

[15] G. Kuenne, A. Ketelheun, and J. Janicka, "LES modeling of premixed combustion using a thickened flame approach coupled with FGM tabulated chemistry," *Combustion and Flame*, vol. 158, no. 9, pp. 1750 – 1767, 2011.

[16] S. Richard, O. Colin, O. Vermorel, A. Benkenida, C. Angelberger, and D. Veynante, "Towards large eddy simulation of combustion in spark ignition engines," *Proceedings of the Combustion Institute*, vol. 31, no. 2, pp. 3059 – 3066, 2007.

[17] H. Weller, G. Tabor, A. Gosman, and C. Fureby, “Application of a flame-wrinkling LES combustion model to a turbulent mixing layer,” *Symposium (International) on Combustion*, vol. 27, no. 1, pp. 899 – 907, 1998. Twenty-Seventh Sysposium (International) on Combustion Volume One.

[18] M. Germano, U. Piomelli, P. Moin, and W. H. Cabot, “A dynamic subgridscale eddy viscosity model,” *Physics of Fluids A: Fluid Dynamics (1989-1993)*, vol. 3, no. 7, pp. 1760–1765, 1991.

[19] F. Charlette, C. Meneveau, and D. Veynante, “A power-law flame wrinkling model for LES of premixed turbulent combustion part two: dynamic formulation,” *Combustion and Flame*, vol. 131, no. 1–2, pp. 181 – 197, 2002.

[20] R. Knikker, D. Veynante, and C. Meneveau, “A dynamic flame surface density model for large eddy simulation of turbulent premixed combustion,” *Physics of Fluids (1994-present)*, vol. 16, no. 11, pp. L91–L94, 2004.

[21] G. Wang, M. Boileau, and D. Veynante, “Implementation of a dynamic thickened flame model for large eddy simulations of turbulent premixed combustion,” *Combustion and Flame*, vol. 158, no. 2, pp. 2199 – 2213, 2011.

[22] G. Wang, M. Boileau, D. Veynante, and K. Truffin, “Large eddy simulation of a growing turbulent premixed flame kernel using a dynamic flame surface density model,” *Combustion and Flame*, vol. 159, no. 8, pp. 2742 – 2754, 2012. Special Issue on Turbulent Combustion.

[23] T. Schmitt, A. Sadiki, B. Fiorina, and D. Veynante, “Impact of dynamic wrinkling model on the prediction accuracy using the F-TACLES combustion model in swirling premixed turbulent flamesp,” *Proceedings of the Combustion Institute*, vol. 34, no. 1, pp. 1261 – 1268, 2013.

[24] D. Veynante, T. Schmitt, M. Boileau, and V. Moureau, “Analysis of dynamic models for turbulent premixed combustion,” in *Proceedings of the Summer Program*, p. 387, 2012.

[25] T. Schmitt, M. Boileau, and D. Veynante, “Flame wrinkling factor dynamic modeling for large eddy simulations of turbulent premixed combustion,” *Flow, Turbulence and Combustion*, vol. 94, no. 1, pp. 199–217, 2015.

[26] S. B. Pope, *Turbulent Flows.* Cambridge University press, 2006.

[27] H. Spurk and N. Aksel, *Stroemungslehre.* Springer, 7 ed., 2006.

[28] K. Hanjalic, “Turbulence and transport phenomena modelling and simulation.” Darmstadt, 2005.

[29] P. Moin and K. Mahesh, “Direct numerical simulation: A tool in turbulence research,” *Annual Review of Fluid Mechanics*, vol. 30, no. 1, pp. 539–578, 1998.

[30] O. Reynolds, “On the dynamical theory of incompressible viscous fluids and the determination of the criterion,” *Philosophical Transactions of the Royal Society of London. A*, vol. 186, pp. pp. 123–164, 1895.

[31] L. Prandtl, “Bericht über die Entstehung der Turbulenz,” *Z. Agnew. Math. Mech*, vol. 5, pp. 136–139, 1925.

[32] E. Van Driest, “On turbulent flow near a wall,” *J. Aerospace Sci.*, vol. 23, pp. 1007–1011, 1956.

[33] A. Smith and T.Cebeci, “Numerical solution of the turbulent-boundary-layer equations,” tech. rep., DOUGLAS AIRCRAFT CO INC LONG BEACH CALIF AIRCRAFT DIV, 1967.

[34] K. Hanjalic and B. Launder, “A reynolds stress model of turbulence and its application to thin shear flows,” *Journal of fluid Mechanics*, vol. 52, no. 04, pp. 609–638, 1972.

[35] J. Rotta, “Statistische Theorie nichthomogener Turbulenzwi,” *Zeitschrift fuer Physik A Hadrons and Nuclei*, vol. 129, no. 6, pp. 547–572, 1951.

[36] W. Jones and B. Launder, “The prediction of laminarization with a two-equation model of turbulence,” *International Journal of Heat and Mass Transfer*, vol. 15, no. 2, pp. 301–314, 1972.

[37] D. Wilcox, *Turbulence modeling for CFD.* La Canada, CA: DCW Industries, 1993.

[38] F. Menter, “Two-equation eddy-viscosity turbulence models for engineering applications,” *AIAA journal*, vol. 32, no. 8, pp. 1598–1605, 1994.

[39] D. Naot, A. Shavit, and M. Wolfshtein, “Interactions between components of the turbulent velocity correlation tensor due to pressure fluctuations(interactions between components of turbulent flow velocity correlation tensor due to pressure fluctuations),” *Israel Journal of Technology*, vol. 8, no. 3, pp. 259–269, 1970.

[40] C. Shir, “A preliminary numerical study of atmospheric turbulent flows in the idealized planetary boundary layer,” *Journal of Atmospheric Sciences*, vol. 30, pp. 1327–1339, 1973.

[41] W. Rodi, “A new algebraic relation for calculating the reynolds stresses,” *Gesellschaft Angewandte Mathematik und Mechanik Workshop Paris France*, vol. 56, pp. 219–221, Mar. 1976.

[42] M. Germano, “A proposal for a redefinition of the turbulent stresses in the filtered navier stokes equations,” *Physics of Fluids*, vol. 29, pp. 2323–2324, 1986.

[43] A. Leonard, “Energy cascade in large-eddy simulations of turbulent fluid flows,” in *Turbulent Diffusion in Environmental Pollution, Proceedings of a Symposium held at Charlottesville* (F. Frenkiel and R. Munn, eds.), vol. 18, Part 1 of *Advances in Geophysics*, pp. 237 – 248, Elsevier, 1975.

[44] J. SMAGORINSKY, “General circulation experiments with the primitive equations,” *Monthly Weather Review*, vol. 91, no. 3, pp. 99–164, 1963.

[45] L. Davidson, “Fluid mechanics, turbulent flow and turbulence modeling.” Division of Fluid Dynamics Department of Applied Mechanics Chalmers University of Technology, October 2010.

[46] G. Erlebacher, M. Y. Hussaini, C. G. Speziale, and T. A. Zang, “Toward the large-eddy simulation of compressible turbulent flows.,” *Journal of Fluid Mechanics*, vol. 238, pp. 155–185, 1992.

[47] W. Cabot and P. Moin, *Large Eddy Simulation of Complex Engineering and Geophysical Flows 7. Large eddy simulation of scalar transport with the dynamic subgrid-scale model.* Cambridge University Press, 1993.

[48] F. A. Jaberi and P. J. Colucci, “Large eddy simulation of heat and mass transport in turbulent flows. part 2: Scalar field,” *International Journal of Heat and Mass Transfer*, vol. 46, no. 10, pp. 1827 – 1840, 2003.

[49] J. Bardina, J. H. Ferziger, W. C. Reynolds, and J. Tso, L. S. G. Kovasznay, & A. K. M. F. Hussain, eds., *Improved subgrid-scale models for large-eddy simulation*, July 1980.

[50] U. Schumann, “Subgrid scale model for finite difference simulations of turbulent flows in plane channels and annuli,” *Journal of Computational Physics*, vol. 18, no. 4, pp. 376 – 404, 1975.

[51] S. Menon, P. K. Yeung, and W. W. Kim, “Effect of subgrid models on the computed interscale energy transfer in isotropic turbulence,” *Computers & Fluids*, vol. 25, no. 2, pp. 165 – 180, 1996.

[52] A. Yoshizawa and K. Horiuti, “A statistically-derived subgrid-scale kinetic energy model for the large-eddy simulation of turbulent flows,” *Journal of the Physical Society of Japan*, vol. 54, no. 8, pp. 2834–2839, 1985.

[53] T. Lehnhäuser and M. Schäfer, “Improved linear interpolation practice for finite-volume schemes on complex grids,” *International journal for numerical methods in fluids*, vol. 38, no. 7, pp. 625–645, 2002.

[54] G. Zhou, L. Davidson, and E. Olsson, “Transonic inviscid/turbulent airfoil flow simulations using a pressure based method with high order schemes,” in *Fourteenth International Conference on Numerical Methods in Fluid Dynamics*, pp. 372–378, Springer, 1995.

[55] H. L. Stone, “Iterative solution of implicit approximations of multidimensional partial differential equations,” *SIAM Journal on Numerical Analysis*, vol. 5, no. 3, pp. 530–558, 1968.

[56] H.-J. Leister and M. Peric, “Vectorized strongly implicit solving procedure for a seven-diagonal coefficient matrix,” *International Journal of Numerical Methods for Heat & Fluid Flow*, vol. 4, no. 2, pp. 159–172, 1994.

[57] M. Klein, A. Sadiki, and J. Janicka, “A digital filter based generation of inflow data for spatially developing direct numerical or large eddy simulations,” *Journal of Computational Physics*, vol. 186, no. 2, pp. 652 – 665, 2003.

[58] K. Richter, R. Friedrich, and L. Schmitt, “Large-eddy simulation of turbulent wall boundary layers with pressure gradient,” in *6th Symposium on Turbulent Shear Flows*, vol. 1, pp. 22–3, 1987.

[59] N. Peters, “Numerical and asymptotic analysis of systematically reduced reaction schemes for hydrocarbon flames,” in *Numerical simulation of combustion phenomena*, pp. 90–109, Springer, 1985.

[60] W. Jones and R. Lindstedt, “Global reaction schemes for hydrocarbon combustion,” *Combustion and Flame*, vol. 73, no. 3, pp. 233–249, 1988.

[61] C. K. Westbrook and F. L. Dryer, “Simplified reaction mechanisms for the oxidation of hydrocarbon fuels in flames,” *Combustion science and technology*, vol. 27, no. 1-2, pp. 31–43, 1981.

[62] W. Chen, “a global reaction rate for nitric oxide reburning.,” 1994.

[63] U. Maas and S. B. Pope, “Implementation of simplified chemical kinetics based on intrinsic low-dimensional manifolds,” in *Symposium (International) on Combustion*, vol. 24, pp. 103–112, Elsevier, 1992.

[64] U. Maas and S. B. Pope, “Simplifying chemical kinetics: intrinsic low-dimensional manifolds in composition space,” *Combustion and Flame*, vol. 88, no. 3, pp. 239–264, 1992.

[65] U. Maas and S. Pope, “Laminar flame calculations using simplified chemical kinetics based on intrinsic low-dimensional manifolds,” in *Symposium (International) on Combustion*, vol. 25, pp. 1349–1356, Elsevier, 1994.

[66] O. Gicquel, N. Darabiha, and D. Thévenin, “Liminar premixed hydrogen/air counterflow flame simulations using flame prolongation of ILDM with differential diffusion,” *Proceedings of the Combustion Institute*, vol. 28, no. 2, pp. 1901–1908, 2000.

[67] B. Fiorina, O. Gicquel, L. Vervisch, S. Carpentier, and N. Darabiha, “Premixed turbulent combustion modeling using tabulated detailed chemistry and PDF,” *Proceedings of the Combustion Institute*, vol. 30, no. 1, pp. 867–874, 2005.

[68] J. Van Oijen, F. Lammers, and L. De Goey, “Modeling of complex premixed burner systems by using flamelet-generated manifolds,” *Combustion and Flame*, vol. 127, no. 3, pp. 2124–2134, 2001.

[69] L. de Goey, J. van Oijen, H. Bongers, and G. Groot, “New flamelet based reduction methods: the bridge between chemical reduction techniques and flamelet methods,” in *European Combustion Meeting, Orléans (France)*, 2003.

[70] B. Fiorina, R. Baron, O. Gicquel, D. Thevenin, S. Carpentier, N. Darabiha, *et al.*, “Modelling non-adiabatic partially premixed flames using flame-prolongation of ILDM,” *Combustion Theory and Modelling*, vol. 7, no. 3, pp. 449–470, 2003.

[71] A. Ketelheun, G. Kuenne, and J. Janicka, “Heat transfer modeling in the context of large eddy simulation of premixed combustion with tabulated chemistry,” *Flow, Turbulence and Combustion*, vol. 91, no. 4, pp. 867–893, 2013.

[72] P. Pantangi, A. Sadiki, J. Janicka, M. Mann, and A. Dreizler, “LES of premixed methane flame impinging on the wall using non-adiabatic flamelet generated manifold (FGM) approach,” *Flow, Turbulence and Combustion*, pp. 1–32, 2014.

[73] R. Mercier, P. Auzillon, V. Moureau, N. Darabiha, O. Gicquel, D. Veynante, and B. Fiorina, “LES modeling of the impact of heat losses and differential diffusion on turbulent stratified flame propagation: Application to the TU Darmstadt stratified flame,” *Flow, Turbulence and Combustion*, vol. 93, no. 2, pp. 349–381, 2014.

[74] G. Ribert, O. Gicquel, N. Darabiha, and D. Veynante, “Tabulation of complex chemistry based on self-similar behavior of laminar premixed flames,” *Combustion and flame*, vol. 146, no. 4, pp. 649–664, 2006.

[75] B. Fiorina, O. Gicquel, and D. Veynante, “Turbulent flame simulation taking advantage of tabulated chemistry self-similar properties,” *Proceedings of the Combustion Institute*, vol. 32, no. 2, pp. 1687–1694, 2009.

[76] K. Wang, G. Ribert, P. Domingo, and L. Vervisch, “Self-similar behavior and chemistry tabulation of burnt-gas diluted premixed flamelets including heat-loss,” *Combustion Theory and Modelling*, vol. 14, no. 4, pp. 541–570, 2010.

[77] S. Pope, “Computationally efficient implementation of combustion chemistry using in situ adaptive tabulation,” 1997.

[78] B. Yang and S. Pope, “Treating chemistry in combustion with detailed mechanisms in situ adaptive tabulation in principal directions premixed combustion,” *Combustion and Flame*, vol. 112, no. 1, pp. 85–112, 1998.

[79] L. Lu and S. B. Pope, “An improved algorithm for in situ adaptive tabulation,” *Journal of Computational Physics*, vol. 228, no. 2, pp. 361–386, 2009.

[80] J.-Y. Chen, J. Blasco, N. Fueyo, and C. Dopazo, “An economical strategy for storage of chemical kinetics: Fitting in situ adaptive tabulation with artificial neural networks,” *Proceedings of the Combustion Institute*, vol. 28, no. 1, pp. 115–121, 2000.

[81] J.-Y. Chen, “Analysis of in situ adaptive tabulation performance for combustion chemistry and improvement with a modified search algorithm,” *Combustion science and technology*, vol. 176, no. 7, pp. 1153–1169, 2004.

[82] T. Poinsot and D. Veynante, *Theoretical and Numerical Combustion*, vol. 3rd Edition. 2012.

[83] N. Peters, *Turbulent combustion.* Cambridge university press, 2000.

[84] N. Peters, “Laminar diffusion flamelet models in non-premixed turbulent combustion,” *Progress in energy and combustion science*, vol. 10, no. 3, pp. 319–339, 1984.

[85] R. Bilger, “Turbulent jet diffusion flames,” *Progress in Energy and Combustion Science*, vol. 1, no. 2, pp. 87–109, 1976.

[86] R. Bilger, “Turbulent flows with nonpremixed reactants,” in *Turbulent reacting flows*, pp. 65–113, Springer, 1980.

[87] R. Bilger, “Turbulent diffusion flames,” *Annual Review of Fluid Mechanics*, vol. 21, no. 1, pp. 101–135, 1989.

[88] R. Bilger, “The structure of turbulent nonpremixed flames,” in *Symposium (International) on Combustion*, vol. 22, pp. 475–488, Elsevier, 1989.

[89] “one-dimensional laminar flame code, eindhoven university of technology,” 2014.

[90] C. Bowman, M. Frenklach, W. Gardiner, and G. Smith, “The GRI 3.0 chemical kinetic mechanism,” *University of California: Berkeley, CA*, 1999.

[91] J. O. Hirschfelder, C. F. Curtiss, R. B. Bird, and M. G. Mayer, *Molecular theory of gases and liquids*, vol. 26. Wiley New York, 1954.

[92] F. Williams, *Combustion theory. Second edition.* Addison-Wesley Pub.,Reading, MA, Jan 1985.

[93] M. Germano, A. Maffio, S. Sello, and G. Mariotti, “On the extension of the dynamic modelling procedure to turbulent reacting flows,” in *Direct and Large-Eddy Simulation II*, pp. 291–300, Springer, 1997.

[94] P. E. DesJardin and S. H. Frankel, “Large eddy simulation of a nonpremixed reacting jet: Application and assessment of subgrid-scale combustion models,” *Physics of Fluids (1994-present)*, vol. 10, no. 9, pp. 2298–2314, 1998.

[95] H. G. Im, T. S. Lund, and J. H. Ferziger, “Large eddy simulation of turbulent front propagation with dynamic subgrid models,” *Physics of Fluids (1994-present)*, vol. 9, no. 12, pp. 3826–3833, 1997.

[96] T. Butler and P. O'Rourke, "A numerical method for two dimensional unsteady reacting flows," *Symposium (International) on Combustion*, vol. 16, no. 1, pp. 1503 – 1515, 1977.

[97] S. Pope, "The evolution of surfaces in turbulence," *International journal of engineering science*, vol. 26, no. 5, pp. 445–469, 1988.

[98] E. Hawkes and R. Cant, "A flame surface density approach to large-eddy simulation of premixed turbulent combustion," *Proceedings of the Combustion Institute*, vol. 28, no. 1, pp. 51–58, 2000.

[99] R. Knikker, D. Veynante, and C. Meneveau, "A priori testing of a similarity model for large eddysimulations of turbulent premixed combustion," *Proceedings of the combustion institute*, vol. 29, no. 2, pp. 2105–2111, 2002.

[100] O. Colin and K. Truffin, "A spark ignition model for large eddy simulation based on an FSD transport equation (ISSIM-LES)," *Proceedings of the Combustion Institute*, vol. 33, no. 2, pp. 3097–3104, 2011.

[101] D. Veynante, A. Trouvé, K. Bray, and T. Mantel, "Gradient and counter-gradient scalar transport in turbulent premixed flames," *Journal of Fluid Mechanics*, vol. 332, pp. 263–293, 1997.

[102] S. Tullis and R. Cant, "Scalar transport modeling in large eddy simulation of turbulent premixed flames," *Proceedings of the Combustion Institute*, vol. 29, no. 2, pp. 2097–2104, 2002.

[103] C. Duwig, "Study of a filtered flamelet formulation for large eddy simulation of premixed turbulent flames," *Flow, Turbulence and Combustion*, vol. 79, no. 4, pp. 433–454, 2007.

[104] P. Auzillon, R. Vicquelin, O. Gicquel, N. Darabiha, D. Veynante, B. Fiorina, *et al.*, "A filtered tabulated chemistry model for large eddy simulation of reactive flows," *AIAA Paper*, 2010.

[105] P. Auzillon, B. Fiorina, R. Vicquelin, N. Darabiha, O. Gicquel, and D. Veynante, "Modeling chemical flame structure and combustion dynamics in LES," *Proceedings of the Combustion Institute*, vol. 33, no. 1, pp. 1331–1338, 2011.

[106] A. Coussement, T. Schmitt, and B. Fiorina, "Filtered tabulated chemistry for non-premixed flames," *Proceedings of the Combustion Institute*, 2014.

[107] M. Philip, M. Boileau, R. Vicquelin, T. Schmitt, D. Durox, J.-F. Bourgouin, and S. Candel, "Simulation of the ignition process in an annular multiple-injector combustor and comparison with experiments," in *ASME Turbo Expo 2014: Turbine Technical Conference and Exposition*, pp. V04BT04A053–V04BT04A053, American Society of Mechanical Engineers, 2014.

[108] M. Philip, M. Boileau, R. Vicquelin, E. Riber, T. Schmitt, B. Cuenot, D. Durox, and S. Candel, "Large eddy simulations of the ignition sequence of an annular multiple-injector combustor," *Proceedings of the Combustion Institute*, 2014.

[109] R. Mercier, T. Schmitt, D. Veynante, and B. Fiorina, "The influence of combustion SGS submodels on the resolved flame propagation. application to the LES of the cambridge stratified flames," *Proceedings of the Combustion Institute*, 2014.

[110] V. Moureau, P. Domingo, and L. Vervisch, "From large-eddy simulation to direct numerical simulation of a lean premixed swirl flame: Filtered laminar flame-PDF modeling," *Combustion and Flame*, vol. 158, no. 7, pp. 1340 – 1357, 2011.

[111] T. Schmitt, "Implementation of a filtered tabulated chemistry model in the LES solver FASTEST," tech. rep., Technische Universität Darmstadt - Center of Smart Interfaces, 2011.

[112] M. Zajadatz, M. Hettel, and W. Leuckel, "Burning velocity of high-turbulence natural gas flames for gas turbine application," in *INTERNATIONAL GAS RESEARCH CONFERENCE*, vol. 5, pp. 793–803, GOVERNMENT INSTTUTES INC, 1998.

[113] M. Zajadatz, N. Zarzalis, and W. Leuckel, "Investigation of the turbulent flame speed for natural gas and natural gas/hydrogen mixtures at high turbulence levels and volumetric heat release rates," in *ASME Turbo Expo 2013: Turbine Technical Conference and Exposition*, pp. V01BT04A003–V01BT04A003, American Society of Mechanical Engineers, 2013.

[114] A. Hosseinzadeh, A. Schwarz, A. Sadiki, and J. Janicka, "Numerical investigation of lean-premixed turbulent flame using combustion LES and thickened flame approach," *ICHMT DIGITAL LIBRARY ONLINE*, pp. 781–784, 2012.

[115] A. Hosseinzadeh, T. Schmitt, A. Sadiki, and J. Janicka, "Large eddy simulation of a lean premixed turbulent flame using dynamic F-TACLES combustion model," 10th International ERCOFTAC Symposium on Engineering Turbulence Modelling and Measurements, 2014.

[116] H. Nawroth, A. Saurabh, C. O. Paschereit, F. Zhang, P. Habisreuther, and H. Bockhorn, "Experimental and numerical investigation of a turbulent premixed flame in an anechoic environment," in *AIAA Fluid Dynamics Conference and Exhibit*, pp. 25–28, 2012.

[117] H. Nawroth, C. O. Paschereit, F. Zhang, P. Habisreuther, and H. Bockhorn, "Flow investigation and acoustic measurements of an unconfined turbulent premixed jet flame," in *43rd AIAA Fluid Dynamics Conference and Exhibit*, 2013.

[118] G. Geiser, A. Hosseinzadeh, H. Nawroth, F. Zhang, H. Bockhorn, P. Habisreuther, J. Janicka, C. Paschereit, and W. Schröder, "Thermoacoustics of a turbulent premixed flame," *20th AIAA/CEAS Aeroacoustics Conference*, 2014.

[119] H. Yamashita, M. Shimada, and T. Takeno, "A numerical study on flame stability at the transition point of jet diffusion flames," in *Symposium (International) on Combustion*, vol. 26, pp. 27–34, Elsevier, 1996.

Lebenslauf

Name	Arash Hossein Zadeh	
Geburtsdatum	04. Juni 1978	
Geburtsort	Teheran	
Studium	09/1997-06/2002	**Azad University, south Tehran, Iran** Fachrichtung: Mechanical engineering Vertiefungen: Strömungslehre, Wärme- und Stoffübertragung, Energietechnik Abschluss zum B.Sc.
	10/2004-08/2009	**Technische Universität Darmstadt** Fachrichtung: Maschinenbau-Mechanical and process engineering Abschluss zum B.Sc.
	10/2009-08/2011	**Technische Universität Darmstadt** Fachrichtung: Maschinenbau-Mechanical and process engineering Vertiefungen: Energietechnik, CFD (Computational Fluid Dynamics) Abschluss zum M.Sc.
Wissenschaftlicher Mitarbeiter	seit 06/2011	**Technische Universität Darmstadt** Wissenschaftlicher Mitarbeiter am Fachgebiet für Energie- und Kraftwerkstechnik (EKT)